

FACULTY OF SCIENCE
UNIVERSITY OF COPENHAGEN



Multiphoton generation from a single quantum dot in a photonic nanostructure

Thomas Hummel

Ph.D. Thesis,
June 2019

Multiphoton generation from a single
quantum dot in a photonic nanostructure

This thesis was prepared by

Thomas Hummel

Supervisors

Ravitej Uppu

Peter Lodahl

Release date: June 12, 2019

Comments: A dissertation submitted to the Niels Bohr Institute at the University of Copenhagen in partial fulfillment of the requirements for the degree of philosophiæ doctor (Dr.) in Quantum Optics.

Quantum Photonics Group
Center for Hybrid Quantum Networks (Hy-Q)
Niels Bohr Institute
University of Copenhagen
Blegdamsvej 17
DK-2100 Copenhagen
Denmark

<https://hy-q.nbi.ku.dk/>

<http://quantum-photonics.nbi.ku.dk/>

Preface

This thesis is the result of three years of research in the Quantum Photonics group at the Niels Bohr Institute, University of Copenhagen. My attention got drawn to this group due to a presentation from Prof. Peter Lodahl during my Master project. The group wanted to expand towards multi-photon applications, which is in my field of interest. Since this was a new direction for the group, the infrastructure was not fully ready to go full throttle on this topic at the start of my PhD. Multi-photon experiments require single photon sources, allowing me to learn about both and broaden the range of topics discussed inside this thesis.

First of all I would like to thank Prof. Peter Lodahl for giving me the opportunity to carry out my doctoral dissertation in the Quantum Photonics group. I would like to convey my sincere gratitude to Peter, my main supervisor. It was an interesting 3 year story in which I learnt more than I could imagine in a wide variety of topics.

Secondly I would like to thank the current group members and the previous group members during my project. There are a few people who I would like to highlight. I would like to thank Matthew Broome and Ravitej Uppu for the daily supervision and all the discussions during my Ph.D.. The mark of these discussions can be seen through all the projects that I worked on. When joining the group, I helped Raphaël Daveau, who together with Henri Thyrrstrup introduced me to the daily life of this group. During my time I have worked together with Claudéric Ouellet-Plamondon, who I want to thank for all his help. Further I had the pleasure of two Master students helping me during my time, Ela Uğur and Hans Eriksen. I enjoyed supervising as well as working together with them.

All of you helped me on different topics, which I would like to expand on **Ravi** helped me on the topics described in chapter 2 to 5. The support ranged from helping with the experiments to understanding the background. **Matt** supported on the work in chapter 2, 3, 5 and 6. A lot of the work was in understanding all the different topics and how to deal with it in the lab. **Clauderic** supported me

with the research discussed in chapters 2 to 4. We had a lot of discussions about the measurements and the results which helped me improve my understanding of semiconductor physics and quantum dots. **Ela** was the first Master student helping me out in the lab. She helped in the setting up of the demultiplexer (chapter 3) and the heralded entanglement gate (chapter 5). **Hans** is continuing the fantastic work on the heralded entanglement gate through his ongoing Master project. He helped out with the finalisation of the entanglement gate setup and in the validation of the calculation related to the gate. During the time of writing this thesis he is interfacing the heralded entanglement gate to the demultiplexer. With respect to this I would like to thank Martin, Hanna, Claudéric, Xiaoyan, Ravi, Hans and Camille for proof reading different section of this thesis.

Besides the aforementioned people I had discussions with many more people. First I want to start thank Henri Thyrrstrup, Hanna Le Jeannic and Gabija Kiršanskė for teaching me a lot about quantum dots, semiconductors and cryogenics. Next I want to thank the people that I shared an office with for all the discussions and jokes, Tommaso Pregiolato, Chirag Patil, Kasper Lund and Freja Pedersen. I am especially grateful for the technical support of the NBI, for which I want to specifically thank Axel Boisen, Jimmy Hansen and Thomas Hedegaard. I want to acknowledge Jürgen Appel, Martin Appel, Maxime Bergamin, Xiao-liu Chu, Raphaël Daveau, Dapeng Ding, Sofie Hansen, Alisa Javadi, Zhe Liu, Sahand Mahmoodian, Leonardo Midolo, Jörg Müller, Camille Papon, Nir Rotenberg, Tim Schröder, Signe Simonsen, Christian Starup, Søren Stobbe, Petru Tighineanu, Asli Ugurlu, Ying Wang, Xiaoyan Zhou, and everybody else whom I met in the Quantum Photonics group, at QUANTOP or at Hy-Q for the discussions and the good times. Not all interactions occur based on science, but some on a social level for which I want to thank everybody I encountered during my Ph.D.. I would like to highlight Alisa Javadi and Petru Tighineanu for all the amazing games of chess we played.

During my Ph.D. I had the pleasure to perform an external project at the University of Oxford in the research group of Prof. Ian Walmsley (currently at Imperial College), where I met many wonderful people. Foremost, I want to thank Prof. Walmsley for this opportunity to learn more about SPDC sources. Further I would like to thank Helen Chrzanowski, Andreas Eckstein, Jelmer Renema and Joelle Boutari for that the project I worked on. I would like to thank my other fellow countryman that I met in Oxford, Tom Wolterink and Sjoerd Loenen for all the nice discussions and jokes. I did not only interact with these people but with everybody in the group. I would like to thank everybody I met during my time in Oxford for the welcome stay.

Last but not least I want to thank my family and friends for all the endless support, advice, cheering or whatever was needed at the time.

Thomas Hummel
Copenhagen, June 2019

Abstract

Single photons are very actively pursued for quantum optical applications due to their robust nature against environmental influences. These applications benefit from deterministic generation of indistinguishable single photons.

Quantum dot sources fabricated in a heterostructure with electrical contacts allows the control of coupling between a photonic crystal waveguide and the quantum dot. This control over the Purcell enhancement allows a tuneable efficiency of the source. The electrodes also allow the study of the Stark tuning of quantum dots and to analyse the effect of charge noise.

The control over quantum dot sources allows the deterministic generation of indistinguishable single photons. Generating multi-photon states using multiple quantum dot single photon sources induces problems since the generated photons are distinguishable from each other. This occurs due to the random growth nature of the quantum dots. Generating a multi photon state from a single quantum dot source requires a temporal-to-spatial mode converter (i.e. demultiplexer). An efficient 4 mode demultiplexer is demonstrated in this thesis with an output four fold coincidence rate of 1.05 ± 0.05 Hz. Thorough analysis of all efficiencies from the source till detection shows that this is the most efficient demultiplexer yet. The generated four photon state can be used as a resource to generate heralded polarisation entanglement between two photons. With an indistinguishability between the photons of 95%, a maximum heralding efficiency of 81% can be achieved. The entanglement gate is built with a port-to-port efficiency of 88%, averaged over all combinations. Incorporating end-to-end losses by coupling the entanglement gate to the demultiplexer results in a maximum achievable heralding efficiency of 31%.

The demultiplexer is built such that it can be upgraded to 8 spatial modes. Adding a second heralded entanglement gate allows proof of principle experiments of device independent quantum key distribution.

Resumé

Enkelte fotoner bliver meget aktivt efterforsket til kvanteoptiske anvendelser, da de er robuste overfor miljømæssige påvirkninger. Disse anvendelser kan drage fordel af deterministisk dannelse af identiske fotoner.

Et kvantepunkt, som er fabrikeret i en heterostruktur med elektriske forbindelser, giver mulighed for at styre koblingen mellem kvantepunktet og en bølgeleder i en fotonisk krystal. Kontrollen over Purcell-forstærkningen tillader styring af effektiviteten af enkeltfotonkilden. Elektroderne tillader også at studere Stark-tuningen af kvantepunktet og at analysere effekten af ladningsstøj.

Kontrollen over kvantepunkts-enkeltfotonkilden tillader deterministisk generering af identiske enkelte fotoner. Brugen af flere kvantepunkts-enkeltfotonkilder til generering af multi-foton-kvantetilstande er problematisk, da fotoner fra forskellige kvantepunkter ikke er identiske grundet den tilfældige dannelse af kvantepunkterne. Laves multi-foton-kvantetilstanden i stedet med ét kvantepunkt, skal der bruges en tidslig til rumlig signalomformer kaldet en demultiplekser. I denne afhandling bliver der demonstreret en effektiv demultiplekser med fire kanaler, som har en firefoldig sammenfaldsfrekvens på 1.05 ± 0.05 Hz. Grundig analyse af alle optiske tab fra fotonkilden til måleinstrumentet viser, at dette er den mest effektive demultiplekser til dato. Den genererede fire-foton-kvantetilstand kan blive brugt som en ressource til at danne annonceret polarisationssammenfiltrering mellem to fotoner. Med 95% identiske fotoner kan der maksimalt opnås en annonceringseffektivitet på 81%. Sammenfiltringsporten er bygget med en indgang-til-udgangseffektivitet på gennemsnitligt 88% beregnet over alle kombinationer mellem indgang og udgang. Kombineres de optiske tab fra demultiplekseren med sammenfiltringsporten vil den maksimalt opnåelige annonceringseffektivitet være 31%.

Demultiplekseren er bygget, så den kan udvides til otte rumlige kanaler. At tilføje en ekstra sammenfiltringsport gør det muligt at udføre eksperimenter, der kan bevise princippet omkring apparatuafhængig kvantemekanisk nøglefordeling.

Samenvatting

Er vindt veel onderzoek plaats naar enkelvoudige fotonen voor kwantumtoepassingen vanwege hun van nature hoge weerstand tegen omgevingsinvloeden. Deze toepassingen kunnen grote voordelen halen uit het gecontroleerd genereren van ononderscheidbare enkelvoudige fotonen.

Kwantumdot bronnen, vervaardigt in een gedoteerde, samengestelde halfgeleider met elektroden, maken een gecontroleerde koppeling mogelijk tussen een fotonisch kristal met golfgeleider en de kwantumdot. De controle over deze Purcell-versterking zorgt voor een regelbaar rendement van de enkelvoudige fotonenbron. De elektroden geven ook de mogelijkheid de Stark-modulatie van een kwantumdot en het effect van ruis door elektrische ladingen te onderzoeken.

Controle over kwantumdot bronnen staat beheerst genereren van ononderscheidbare fotonen toe. Het produceren van een meervoudige fotonentoestand door meerdere enkelvoudige fotonenbronnen, gebaseerd op kwantum dots, te gebruiken, wordt bemoeilijkt doordat de fotonen van verschillende kwantum dotbronnen onderscheidbaar zijn. De onderscheidbaarheid ontstaat door willekeur in de groei van kwantumdots. Voor het produceren van een meervoudige fotonentoestand met één enkel kwantumdot is een tijd-naar-ruimte transformator nodig, een zogeheten demultiplexer. Dit proefschrift beschrijft een hoog-rendement vier-foton demultiplexer met een meervoudige detectiesnelheid van 1.05 ± 0.05 Hz. Grondig onderzoek naar alle fotonische verliezen laat zien dat de voor dit onderzoek gebruikte demultiplexer het hoogste rendement tot nu toe biedt. De gegenereerde vier-foton toestanden kunnen worden gebruikt voor de melding van polarisatie-verstrengelde fotonen. Met een ononderscheidbaarheid van 95% tussen de fotonen kan een aankondigingsrendament van 81% worden bereikt met deze verstrengelingspoort. De verstrengelingspoort is gebouwd met een poort-naar-poort rendement van 88%, gemeten gemiddelde over alle combinaties. Als de demultiplexer en de verstrengelingspoort worden gecombineerd kan, met inachtneming van de verliezen, een aankondigingsrendament van maximaal 31% worden bereikt.

De opstelling van de demultiplexer is ontworpen om eenvoudig te worden uitgebreid naar een acht-poorts demultiplexer. Als hier een tweede verstrengelingspoort aan wordt toegevoegd, kan de werking van apparaat-onafhankelijke kwantumsleuteldistributie worden aangetoond.

List of publications

The work performed during this Ph.D.-project has resulted in the following publications:

- **Thomas Hummel**, Claudéric Ouellet-Plamondon, Ela Uğur, Irina Kulkova, Toke Lund-Hansen, Matthew A. Broome, Ravitej Uppu, and Peter Lodahl, "Efficient demultiplexed single-photon source with a quantum dot coupled to a nanophotonic waveguide", *Applied Physics Letters* accepted (2019)
- C. Ouellet-Plamondon, R. Uppu, **T. Hummel**, T. Pregolato, C. Papon, L. Midolo, A. D. Wieck, A. Ludwig, R. J. Warburton, P. Lodahl, "Extracting the quantum efficiency of a quantum-dot nanophotonic single-photon source under resonant excitation", *in preperation*

Contents

Preface	v
Abstract	vii
Resumé	ix
Samenvatting	xi
List of publications	xiii
1 Introduction	1
2 Theoretical background	5
2.1 Properties of semiconductors	6
2.1.1 Electrical tuning of energy bands	8
2.1.2 Effect of confinement	9
2.1.3 Quantum dots	11
2.1.4 Excitation of energy states	13
2.2 Quantum dot single-photon source	14
2.2.1 Spontaneous emission	15
2.2.2 Nano-photonic structures for efficient collection	17
2.2.3 Spectral characterisation	20
2.3 Single photon characterisation	25
2.3.1 Source efficiency	25
2.3.2 Single photon purity	26
2.3.3 Indistinguishability	29
2.3.4 Rate equation modelling	31
2.4 Parametric down conversion sources	34
3 Temporal-to-spatial mode conversion of single photons	39
3.1 Temporal-to-spatial demultiplexer setup	40
3.1.1 Source characterisation	41
3.1.2 Operation of the demultiplexer	46
3.2 Expectation of four fold detection rates	47

CONTENTS

3.2.1	General expectation for M-fold demultiplexer	47
3.2.2	Results from demultiplexing experiment	50
3.2.3	Expansion of demultiplexer setup	51
3.3	Conclusion and outlook	53
4	Characterisation of Single Photon Sources	55
4.1	Characterisation of quantum dots	56
4.1.1	Characterisation of quantum dots in waveguides	56
4.1.2	Effect of WG width variation on QD resonance	61
4.1.3	Purcell enhancement in photonic crystal waveguides	65
4.2	Building a SPDC source	69
4.2.1	Optimising spectral properties	70
4.2.2	Optimising built SPDC source	72
4.3	Comparison SPDC and Quantum Dots	76
4.4	Conclusion	79
5	Heralded Entanglement Generation	81
5.1	Operation of the heralded entanglement gate	82
5.2	Effects of experimental limitations	87
5.3	Entanglement confirmation	91
5.4	Conclusion	91
6	Time-bin BosonSampler	93
6.1	Time-bin BosonSampling setup	95
6.2	Calculating the unitary operation	96
6.3	Conclusion	102
7	Conclusion and outlook	103
	Bibliography	105
A	Rate equation modelling for demultiplexed source	121
B	Setup design of the demultiplexer	125
C	States in entanglement gate	127
D	Polarising beamsplitter with limited indistinguishability	133

CH. 1

Introduction

Quantum mechanics started to emerge at the beginning of the 20th century inducing a drastic change in the view of the physical world. This change started with Max Planck's quantised radiation in 1901 [1] leading to the wave-particle duality of light. The wave-particle duality was followed up by Albert Einstein with the photoelectric effect in 1905 [2, 3]. The experiment confirmed discretisation of the system, assumed to be from the photons. Careful analysis later on showed that the photoelectric effect can be explained with the discretisation of the atom [4]. The atomic model with discretized energy states was introduced in 1913 [5] by Niels Bohr. This quantisation formed the basis for quantum mechanics, formalised by Werner Heisenberg in 1925 [6] and Erwin Schrödinger in 1926 [7] (See [8] or any other quantum mechanics textbook for more). Max Born introduced the probability amplitude in 1926 [9] to link the wave function with observables of quantum mechanics.

The intrinsic random nature in quantum mechanics radically changed the view of the world since all earlier theories assumed nature to be deterministic. Due to the intrinsic randomness Albert Einstein assumed quantum mechanics to be an incomplete theory and proposed the existence of local hidden variables together with Boris Podolski and Nathan Rosen [10]. This led to the *EPR-Paradox*. Thorough analysis of John Bell resulted in a proposal on which local hidden variables could be rejected [11], and therefore can establish quantum mechanical

principles. The rejection of local hidden variables can be done with a Bell-test where the violation of an inequality meant that the system can not be described with local hidden variables. The first violation of the Bell-inequality was measured in the eighties by Aspect, Grangier and Roger [12–14].

The progress in the understanding of quantum mechanics has lead to different potential technologies. Two fields where the quantum advantage is significant and feasible are computation and cryptography. The advantage can be understood from the units in which computer calculate. A classical computer calculates in discrete bits (a '0' or a '1'), where a quantum computer calculates with qubits. These qubits are a superposition of the two classical bits $\alpha |0\rangle + \beta |1\rangle$ where α and β are normalisation constants with $|\alpha|^2 + |\beta|^2 = 1$. More information can be encoded on the qubit due to this superposition of two classical bits. Different protocols that utilising this fundamental advantage of quantum mechanics have been proposed over the last decades. Examples of protocols benefiting from the advantage of quantum mechanics are the Deutsch-Jozsa protocol [15], Shor's algorithm [16], Grover's algorithm [17, 18] and the HHL-algorithm [19]. All classical and quantum algorithms have a mathematical limit in the minimum number of operations required to execute the algorithm. The advantage in the quantum algorithms over the classical ones is the slower scaling in the number of operations with increasing input size. This results in less required operations for a quantum algorithm.

The first scheme for a universal quantum computer based on linear optics was proposed in 2001 by Knill, Laflamme and Milburn [20]. The qubits in this scheme are single photons that interfere with each other via a linear optical network of phase shifters and beamsplitters. While this scheme implements a universal quantum computer in a straightforward manner, the number of photons required for operating a quantum algorithm that would outperform a classical computer is technologically out of reach [21]. A more realistic scheme to prove quantum advantage is a quantum simulator. Such simulator can only perform a single task, in which it obtains a speedup due to the quantum effects in play. Possible applications for a simulator is for example the interaction of molecules [22–25]. This is a hard task to calculate with a classical computer, when the number of atoms and interactions increase. A controlled quantum system that emulates the interactions and the complex quantum dynamics in the molecular system would naturally be more advantageous. One of the pursued quantum simulators is the BosonSampler [26, 27], which can be constructed from a network of linear optical components [28–31]. The optical BosonSampler requires multiple indistinguishable single photons at the input which are interfered through an optical network and then detected. A BosonSampler simulates the output state of any unitary evolution that can be mapped onto it. Calculating the output state of a BosonSampler requires the calculation of matrix permanents, which is hard for a classical computer. A BosonSampler does however not calculate the permanents of

a matrix and cannot be used as a calculator.

Computation and cryptography go hand in hand since most of the current used cryptographic schemes rely on computational complexity. Classical encryption methods are mostly based on either a priori sharing an encryption key and authentication key or on mathematical assumptions on the hardness of certain calculations. One of these schemes that rely on computational complexity is RSA, which relies on the factorisation of large integers and is assumed to be hard for a classical computer. Shor's algorithm on the other hand is expected to factorise large number in a faster timescale than a classical computer is capable of, imposing a risk on the RSA encryption method. The risk that a quantum computer poses on current cryptography schemes can be overcome with quantum cryptography. Various quantum cryptography schemes have been proposed that enable secure communication which include Quantum Key Distribution [32–36], Quantum Secure Direct Communication [37, 38], Quantum Key Recycling [39] and Quantum Secret Sharing [40].

The route towards establishing the quantum advantage requires multiple experimental resources. One of the pursued directions to show quantum advantage is based on photonics due to the robust nature of single photons [31, 41, 42]. This allows the scaling of the circuits performing quantum protocols. To harness the benefits from quantum optics, efficient deterministic generation of multiple indistinguishable single photons is required [43–45]. Traditional approaches consist of non-linear photon source [46–48] which are limited by the generation efficiency. The advances of quantum dot single photon source as near-ideal sources [49–51] brings an alternative in the single photon generation. The fabrication of photonic nanostructures around the quantum dots resulted in deterministic single photon sources [52–56]. This gives an alternative for bright multi photon sources by active temporal-to-spatial demultiplexing [57–59]. Recent measurements of high indistinguishability over long time scales allows for this demultiplexing route [60].

This thesis focuses on the route towards quantum advantage using photonic architectures. the thesis starts with the required background in Ch. 2, which covers topics such as semiconductor physics, quantum confinement, and single photon properties.

Chapter 3 introduces an efficient method to generate multiple photons using a single quantum dot. This is performed by a temporal-to-spatial mode converter consisting of a series of optical switches acting on the emission from a quantum dot. This chapter demonstrates the generation of four spatially separated photons employing the temporal-to-spatial mode converter.

Chapter 4 focuses on the effect of the nanostructures on the quantum dot emission. The chapter deals with quantum dot embedded in a semiconductor heterostructure with electrical contacts for control over the quantum dots. The

Chapter 1. Introduction

gates enable charge control and tuning of the quantum dot emission. This chapter also discusses the characterisation of an SPDC source, allowing the comparison of properties between an SPDC source and a quantum dot source.

Chapter 5 discusses an application of the four-channel demultiplexer from Ch. 3. This gate generates polarisation entangled photon pairs from the four photon input states. Entangled photons are a crucial resource for quantum cryptography and allows fundamental tests of quantum mechanics.

Chapter 6 introduces an optical circuit operating in the temporal domain, a time-bin BosonSampler. The advantage of using a time-bin based BosonSampler over a spatial BosonSampler is that the number of required optical elements does not depend on the number of modes in the system. The calculation of the time evolution of the state through the BosonSampler is shown with realistic optical elements.

CH. 2

Theoretical background

There are many proposals on using photons for applications as quantum information processing [20, 26, 61] or quantum communication [32, 33, 35] going as far as a quantum internet [45, 62]. Background knowledge on single photon sources [50] and photon characteristics are required for these protocols, since photons are the information carriers. This chapter discusses the required background for single photon sources and photon properties. Section 2.1 describes the fabrication of a single photon source in a semiconductor. Fabricating such a source requires the knowledge of what a semiconductor is and which properties it has. This allows the introduction of a quantum dot embedded in a semiconductor and how to use it as a single photon source. Section 2.2 follows up on this by describing the excitation and relaxation properties of such a quantum dot and how it can be altered with the fabrication of nanostructures. Section 2.3 discusses the properties of single photons and how to measure them, followed by discussing the efficiency of quantum dot single photon sources. The last part touches on parametric down conversion sources (Sec. 2.4), since this is another commonly used single photon source.

2.1 Properties of semiconductors

Semiconductor materials are commonly used in electronics because the electrical properties can be determined from fabrication. This allows the construction of small electrical devices in a single chip, such as electrical transistors. These transistors can be used for complex circuits, on which the Nobel prize was awarded in 2000 [63]. There are many different type of semiconductors based on different groups in the *periodic table*, such as the group-IV and group-III-V semiconductors [64]. The advantage of semiconductors over conducting materials is that semiconductors can be tuned to be conductive or resistive during fabrication, and afterwards by applied external influences [64–66]. This tuning on conductivity during fabrication can be done on the microscopic scale allowing the fabrication of small electrical circuits.

To identify the differences between conductors, semiconductors and insulators, we need to take a step back and look at the Bohr model of a single atom. In this model, an atom has discrete electron orbitals that can be occupied by electrons. Certain parameters and the orbital an electron is in determines the state of an electron with a limited number of electron states per orbital. An electron state is only occupied by a single electron since *Pauli's exclusion principle* prohibit the occupation of a state by multiple electrons [8] (p. 204) [4] (p. 38) [67] (p. 474). Every state can be described by a different quantum numbers: n (principal quantum number: $n= 1, 2, 3, \dots$), l (angular quantum number: $l= 0, 1, 2, \dots, n - 1$), m_l (magnetic quantum number: $m_l = -l, -l + 1, \dots, l - 1, l$) and m_s (spin quantum number: $m_s = -s, \dots, s$) where s is the spin. When the system is in the lowest energy state at 0 K all the electron states are filled up starting from the lowest energetic state. The electrons in the highest energetic orbital that is partially filled are the valence electrons of the atom.

When an atom is brought into proximity of another atom, the orbitals hybridise [64] (p. 83). This results in energy splittings around the original orbital energies resulting in non-degenerate energy states. When multiple atoms are brought into proximity, the orbitals of these atoms hybridises, resulting in many hybridised energy states around the original orbital energy levels. All these discrete hybridised energy states can be treated as a continuum of states with sufficient atoms. All the energy states created around an orbital can then be seen as an energy band, creating a band-structure with all the orbitals. When this collection of atoms is reduced to the lowest energetic state (cooled to 0 K), the electrons are in the lowest states possible. The energy level of states up to where the electron fills up is related to the Fermi level. This Fermi level is the electrochemical potential for electrons and can be seen as a free electron kinetic energy, meaning that any electron with an energy larger than the Fermi level behaves as a free electron and lead to electrical conduction. This causes different scenarios of how the orbitals hybridise and to which energy level the electrons fill up. The first scenario is where

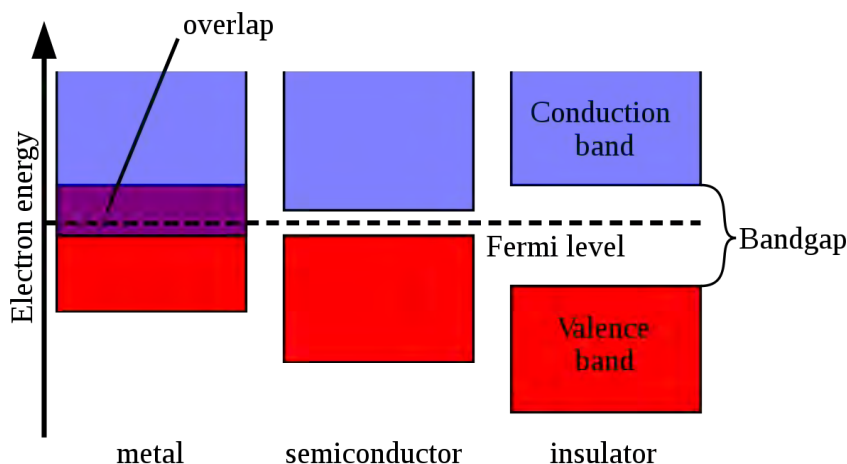


Figure 2.1: Reprint from [68]. Schematic illustration of the differences between a metal, semiconductor and insulator. Vertical axis represents the electron energy of a state and the horizontal axis represent the three types of material. **Left** metal, **centre** semiconductor, **right** insulator.

the hybridisation makes energy levels from different orbitals overlap around the Fermi level. This ensures that at any non zero temperature an electron can occupy a state above the Fermi level and conduct electricity. This is also the case when the hybridised energy level do not overlap, but the Fermi level lies within an energy band. Both these cases ensures that the material behaves as a conductor and are called metals. When the hybridised energy levels do not overlap and the Fermi level lies between two bands, the material is called an insulator or semiconductor [66] (p. 33). This scenario allows the definition of a valance band and conduction band where the valence is the energy band with the highest energetic electron and the conduction band the lowest energetic band without an electron. The energy difference between the highest energy in the valence band and the lowest energy state in the conduction band is the bandgap energy ϵ_g . The band structures and Fermi levels for a metal, semiconductor an insulator are schematically shown in Fig. 2.1.

The distribution of electrons over the energy states is depending on temperature and can be calculated via the Fermi-Dirac distribution [8] (p. 241) [4] (p. 347)

$$f(\epsilon) = \frac{1}{e^{\frac{\epsilon - \epsilon_f}{k_b T}} + 1}, \quad (2.1)$$

with ϵ as the energy of the state, ϵ_f the Fermi level, k_b the Boltzmann constant and T the temperature. This only describes the distribution over existing states and does not take the density of states into account. If we take $N(\epsilon)$ as the num-

ber of states at energy ϵ , the electron occupation density turn into

$$n(\epsilon) = N(\epsilon) \cdot f(\epsilon). \quad (2.2)$$

The textbook difference between an insulator and semiconductor is the bandgap energy, but this is a weak constraint since there are semiconductors with a larger bandgap than certain insulators. A more practical difference is therefore the applicability of induced defects to tune the electrical properties of the material where semiconductors can be doped with impurities. The introduction of doping adds electrons (n-type) or removes electrons (p-type) from the material defining non doped materials as intrinsic (i-type). Doping a semiconductor with an electron or hole (removed electron), energy states are created inside the bandgap compensating for the addition or removal of the electron [66] (p. 23). Adding the extra energy states with dopants changes the band edges of the semiconductor depending on the concentration of doping. Since the Fermi level and bandgap energy remains constant, it creates a tool to alter the Fermi level relative to the band edges. In case of a group-IV semiconductor, electrons (holes) can be added by replacing some group-IV material by group-V (Group-III) material. in the case of Silicon, the n-doping can consist of Phosphor, Arsenic or Antimony (Boron, Aluminium, Gallium or Indium for p-doping). For a type-III-V semiconductor, the doping can consist of a type-IV material replacing either the type-III (n-doping) or type-V (p-doping) material. In case of GaAs (type-III-V semiconductor) this can be done with Silicon (n-doping, replacing Gallium [69]) and Carbon (p-doping, replacing Arsenic [69]).

2.1.1 Electrical tuning of energy bands

Adding doping tunes the band edges relative to the Fermi level, allowing the construction of semiconductors with spatially varying energy bands. The most simple

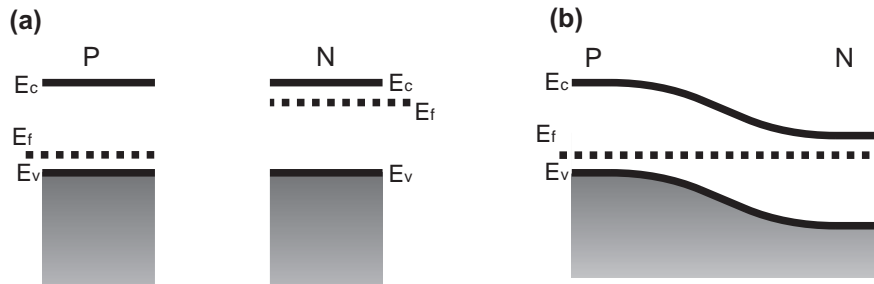


Figure 2.2: **(a)** Doped semiconductor materials before merging with the Fermi levels shifted towards a band edge. **(b)** The two doped materials merged together forming a PN-junction around the intersection. The Fermi level is constant across the material causing a depletion region around the connection surface modifying the band edges. The grey shade illustrate states filled with electrons.

device consist of a semiconductor where one side is p-doped and the other side n-doped. The result is a PN-junction where the two different sides join as shown in Fig. 2.2. The semiconductor with p-doping (left) and n-doping (right) are shown in Fig. 2.2 (a). The Fermi level is shifted in the bandgap towards a band edge, where the direction of the shift depends on the type of doping. The shaded area indicate the valence band filled with electrons while the conduction band is empty. Merging the two doped semiconductors together results in the band diagram of Fig. 2.2 (b). Since the Fermi level is constant in thermal equilibrium, the band edges obtain a spatial distribution in the depletion region. Since p-doped material has excess holes and n-doped material excess electrons, there is a region where the excess electrons and holes migrate to and recombine. This creates a region with a build-in electric field which causes the energy-bands to shift. The shift can be determined from the relative difference between the band edge and the Fermi level of the different doped materials. The width of the depletion region can be determined from the concentration of dopants, since the number of electrons that migrated is known from the electric potential.

The calculation of the build-in electric field hold in thermal equilibrium, which can be broken by applying an external electric potential. This results in a non-constant quasi Fermi level, since the Fermi level is not defined if the material is not in thermal equilibrium. This quasi Fermi level is altered by the applied electric potential, where a larger potential reduces the Fermi level. This occurs because the potential adds energy, with the result that less energy is required to add an extra electron (as defined for the Fermi level). The energy bands shift along with the quasi Fermi level, resulting in a tool to tune the electrical properties.

2.1.2 Effect of confinement

Another method to tune the band diagram of a semiconductor is to use materials with different band gaps [70] (p. 145), as visualised in Fig. 2.3. This shows two materials where a slab of material 2 is placed between two slabs of material 1. Material 2 has a narrower bandgap creating a localised area with different energy states. This area is confined by the narrow width of material 2, altering the hybridisation of orbitals resulting in a change of the *Density of Electron States* (DES). Spatial confinement results in discretized energy states along the confinement direction as shown in the bottom of Fig. 2.3. The non confined direction still has a continuous density of electron states.

Confinement of material 2 results in a change of DES, where the behaviour of the DES changes with the number of dimensions along which the material is confined [70] (p. 143). Figure 2.4 shows the confinement direction (top) and DES (bottom) for (a) no confinement, (b) 1-dimensional, (c) 2-dimensional and (d) 3-dimensional confinement. The density of states can be calculated via the dispersion relation of the electron in the first Brillouin zone [71] of the semiconductor

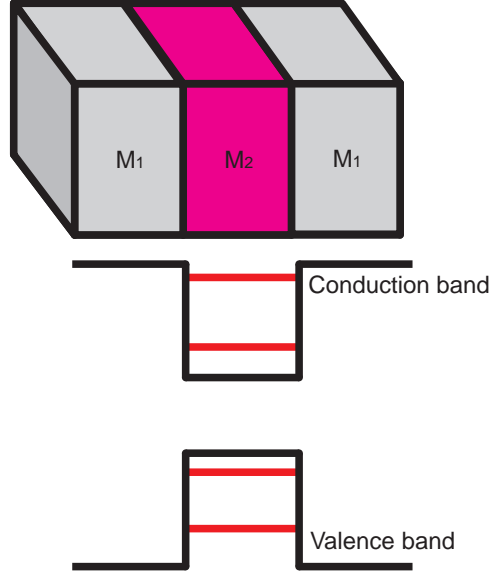


Figure 2.3: Confining a semiconductor slab within a semiconductor with a different bandgap energy (top). This creates discretized energy states along the direction of confinement (bottom).

between all the symmetry points. The bottom of Fig. 2.4 shows the increased discretization of the DES, where the quantum dot shows a completely discretized DES. Assuming a cube quantum dot, the energy of the electron in the lowest energy state can be calculated with [70] (p. 156)

$$E_e(\mathbf{k}) = E_g + \frac{\hbar^2 \pi^2}{2m_e^* L_x^2} + \frac{\hbar^2 \pi^2}{2m_e^* L_y^2} + \frac{\hbar^2 \pi^2}{2m_e^* L_z^2}, \quad (2.3)$$

where L_x (L_y, L_z) is the size of confinement along the x-direction (y-direction, z-direction), m_e^* the effective electron mass and E_g the bandgap energy of the confined material if it was in bulk. The energy of a hole can be calculated in the same fashion as the energy of the electron via

$$E_h(\mathbf{k}) = \frac{\hbar^2 \pi^2}{2m_h^* L_x^2} + \frac{\hbar^2 \pi^2}{2m_h^* L_y^2} + \frac{\hbar^2 \pi^2}{2m_h^* L_z^2}, \quad (2.4)$$

If the system is in the ground state meaning that all the valence band states are occupied and all the conduction band states are empty, the required energy to excite an electron in the QD from the ground state to the first excited state can be calculated. This excitation requires the generation of an electron-hole pair (exciton) in the QD and requires the energy it takes to bring the electron from the highest valence band state to the lowest conduction band state, which is

$$E_{exciton} = E_e + E_h = E_g + \frac{\hbar^2 \pi^2}{2} \left(\frac{m_h^* + m_e^*}{m_e^* m_h^*} \right) \left(\frac{1}{L_x^2} + \frac{1}{L_y^2} + \frac{1}{L_z^2} \right) \quad (2.5)$$

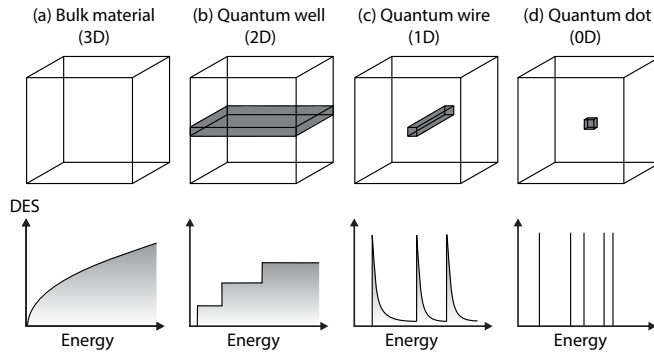


Figure 2.4: Reprint from [72] Density of electron states (DES, bottom) for the possible dimensionality of confinement (top). **(a)** No confinement (Bulk). The DES is in all three direction continuous, resulting in a continuous increase with energy. **(b)** 1 Dimensional confinement (quantum well). The energy states are discrete in one dimension, resulting in a stepwise increase of the DES. **(c)** 2 Dimensional confinement (quantum wire). The single direction in which the electrons can move freely result in a decay DES after every energy step from the confinement. **(d)** 3 Dimensional confinement (quantum dot). The discretization of the energy states in all three dimensions results in a completely discretized DES.

2.1.3 Quantum dots

From the basic principle of the quantum dot a more realistic view can be established. The quantum dot structures in this thesis are made from InAs located in a GaAs structure. The quantum dots are fabricated via the Stranski-Krastanov method [75] (p. 146) in which a layer of InAs is grown on GaAs. The lattice mis-

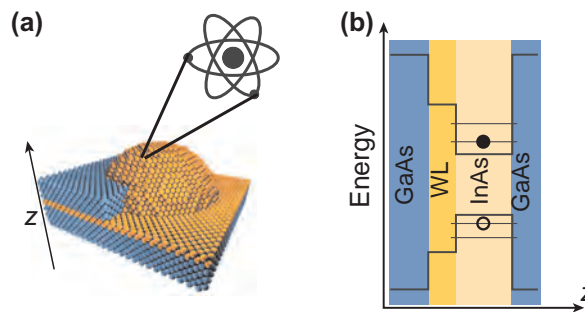


Figure 2.5: (Adapted from [73, 74]) **(a)** Schematic of the grown quantum dots. The blue dots represents the atomic layers of GaAs, on which a layer of InAs (orange dots) is grown. Lattice mismatch between GaAs and InAs induces defects forming quantum dots. **(b)** Band diagram representation of the QD embedded in a GaAs substrate. The InAs quantum dot is connected to a wetting layer induced by the monolayer of InAs forming a quantum well.

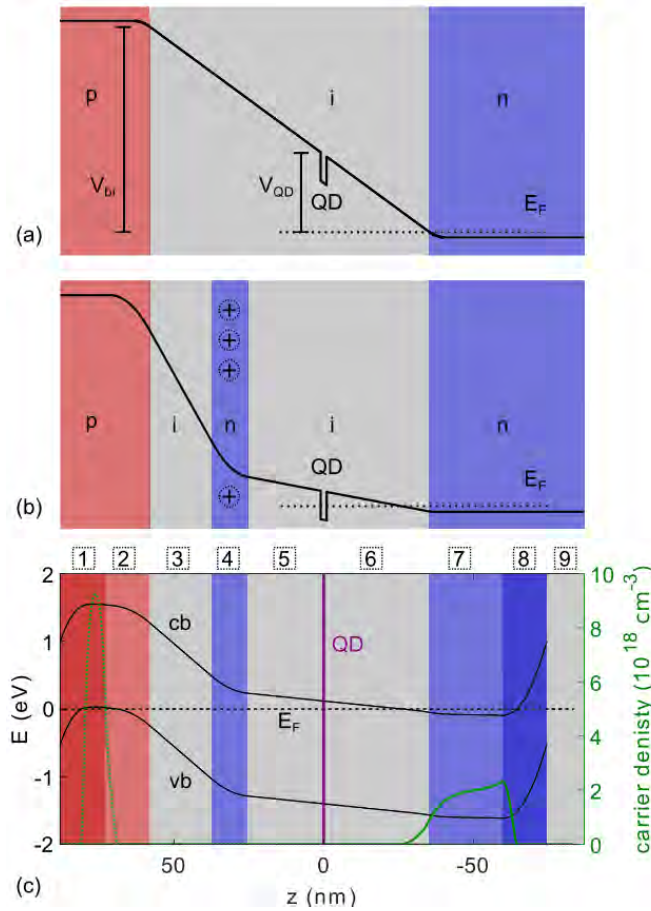


Figure 2.6: reprint from [69] **(a,b)** Schematic of a $p-i-n(-i-n)$ junction showing the location of the quantum dots. The colours represent the doped areas (red: p-doping; blue: n-doping; grey: intrinsic). Solid line indicates the conduction band edge. The $p-i-n-i-n$ structure has an extra n-layer to sandwich the intrinsic QD-layer between two n-layers reducing the built in potential over the QD. **(c)** Simulation of the $p-i-n-i-n$ structure showing the conduction band, valence and the Fermi level. The quantum dot layer is not taken into account for the band edges due to the narrow width, but it is marked with a purple line. The doped areas are colour marked where the intensity indicate the doping concentration. The outer doped areas have a higher concentration (approximately factor 4 to 5 higher) to allow the fabrication of an Ohmic contact to a metal.

match between InAs and GaAs induce defects after the growth of approximately 1 or 2 monolayers of InAs [76]. These defects arise randomly over the sample and grow a few nanometer high and encapsulated in another layer of GaAs. This quantum dot formation is schematically shown in Fig. 2.5 (a) where the blue dots represent the GaAs and the orange dots the InAs. The band structure is shown in

Fig. 2.5 (b) with from left to right (bottom to top in the sample) the bottom GaAs, the InAs monolayer creating a quantum well (Also called the wetting layer), the InAs quantum dot, and on top the encapsulating GaAs.

The quantum dot structure is located between doped GaAs layers with two common type of structures, $p-i-n$ and $p-i-n-i-n$. The letters p , n and i indicate the order of doping types. The quantum dots are located in the intrinsic layer of the structure, where in the $p-i-n-i-n$ case it is the intrinsic layer between the two n -layers. The structures are shown in Fig. 2.6, with a schematic of the conduction band edge for (a) the $p-i-n$ structure and (b) the $p-i-n-i-n$ structure. A simulation of the $p-i-n-i-n$ band structure is shown in Fig. 2.6 (c), where the quantum dot layer is not taken into account in the simulation. The colours represent the different dopants (red: p-doping; blue: n-doping; grey: intrinsic), where the colour intensity indicates the doping concentration. The numbers indicate the different layers of the material and [69] gives more specific information on the layers (Doping concentration and thickness). The growth of the sample starts from the bottom (the first n -layer) with $\text{Al}_{0.75}\text{Ga}_{0.25}\text{As}$ which is used as a sacrificial layer to make suspended structures. The $p-i-n(-i-n)$ structures are grown on top of that starting from the n -layers (Silicon doped [69]) and ending with the p -layers (Carbon doped [69]). Despite the fact that the QD is in the intrinsic layer, the concentration of dopants and small size of the structure ensures that the QD is in a depletion region and obtained a slope of the band edges. The induced electric field tunes the quantum dot energy levels, and can be further tuned with an external applied electric field. The shifts of the confined energy states occur due to the Stark-effect [77–79], where the linear term arise from the bulk stark effect and the parabolic term from the quantum confined stark effect [80].

2.1.4 Excitation of energy states

An excitation of a quantum dot moves an electron from the valence band into the conduction band generating an electron-hole pair. If the electron and hole are bound to each other it is called an exciton [70] (p. 95), else they are a free electron and/or a free hole. The exciton decays when the electron hole pair recombines. This releases the energy which can be in the form of a photon (radiative) or phonon (non-radiative). The photons of interest for the experiments in this thesis are generated when an exciton in the lowest excited state decays radiatively. An exciton in a higher excited state typically relaxes back into the lowest excited state before it decays to the ground state. This occurs because intraband relaxation is in the time scale of 0.3 – 3 ps [81–84] while interband relaxation is in the order of 1 ns. The excitation of the quantum dot can be performed via different methods. The four most common optical excitations are shown in Fig. 2.7 with (a) aboveband excitation, (b) wetting layer excitation, (c) p-shell excitation and (d) resonant excitation. Methods (a) to (c) excite the quantum dot to a higher excited state and requires the quantum dot to relax back into the first excited

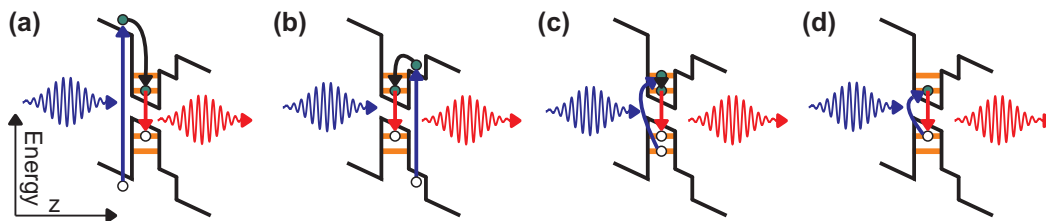


Figure 2.7: Different excitation schemes for a quantum dot. Every scheme requires the absorption of a photon (blue), relaxation to the first excited state (except for **(d)**) and a decay back into the ground state. The decay from the first excited state to the ground state results in the emission of a single photon (red). The shown schemes are **(a)** aboveband excitation, **(b)** wetting layer excitation, **(c)** p-shell excitation and **(d)** resonant excitation. The differences in excitation occur from the excitation laser wavelength.

state. The difference between the three is the location in the band structure where the excitation occurs and with which energy. The advantage of these methods is that the excitation wavelength is different from the emission wavelength and can be spectrally filtered. The disadvantage is that it requires the intraband relaxation and that other charged states can be excited ((a) and (b)). The other charge states occur if an exciton is generated of which the electron or hole gets trapped by the quantum dot while the other becomes a free electron or hole. This alters the energy levels inside the quantum dot and changes the required energy to create an exciton. This automatically arises the advantages and disadvantages of (d) (resonant excitation), which ensures that only the first excited state is excited. This ensures that a previous excitation could not have charged the quantum dot. Resonant excitation can also reach near perfect excitation of the first excited state via π -pulse excitation [85, 86]. The disadvantage is that the wavelength of the excitation laser and the emitted photons is identical which means that other means of filtering than spectral filtering have to be used to remove the laser light in the emission path.

2.2 Quantum dot single-photon source

A quantum dot in a semiconductor can act as a single-photon source which emission wavelength can be tuned by applying a voltage. A quantum dot in bulk material can be treated as a dipole and therefore emits light in a dipole pattern. This pattern is symmetric along the dipole axis, resulting in a low fraction of the emission into a specific direction. To create an efficient source from a quantum dot, controlled and efficient collection of the photons is required by directing all the emission into a desired direction. The directionality of emission can be controlled by fabricating nanostructures around the quantum dot [50, 87, 88] allowing efficient collection of the generated photons.

2.2.1 Spontaneous emission

To quantify the control of emission from a quantum dot, the emission properties have to be evaluated. Due to the tight three-dimensional confinement of a quantum dot, it can be described as an artificial atom (See Fig. 2.11 in Sec. 2.2.3 for the level structure). The general properties of a two level system can be described with the Einstein Coefficients [4] (p. 48 – 51) A_{21} (Spontaneous emission), B_{12} (absorption) and B_{21} (stimulated emission). These coefficients are related to each other thus if one is known, the rest can be calculated. The coefficient for spontaneous emission is related to the lifetime of a state via [4] (p. 49)

$$\tau = \frac{1}{A_{21}}, \quad (2.6)$$

where the coefficients are related via [4] (p. 51)

$$g_1 B_{12} = g_2 B_{21} \quad (2.7)$$

and

$$A_{21} = \frac{\hbar\omega^3}{\pi^2 c^3} B_{21}, \quad (2.8)$$

where g_1 (g_2) is the degeneracy of state 1 (state 2), \hbar is the reduced Planck constant, ω is the radiation wavelength and c is the speed of light. To obtain the transition rate between two states we use Fermi's golden rule [4] (p. 51)

$$W_{i \rightarrow f} = \frac{2\pi}{\hbar} |M_{if}|^2 g(\hbar\omega), \quad (2.9)$$

where M_{if} is transition matrix element from the initial state (i) to the final state (f) and $g(\hbar\omega)$ is the density of final states. The transition matrix element is calculated via perturbation theory with an interaction Hamiltonian via $|M_{if}|^2 = \left| \langle f | \hat{H}_{int} | i \rangle \right|^2$. When we sum over all possible final states f , the density of states can be represented as Dirac-delta function $g(\hbar\omega) = \delta(\omega_i - \omega_f)/\hbar$. The total radiative decay rate is obtained by summing over all individual channels contributing to the radiation, resulting in [64] (p. 260) [89] (p. 271)

$$\gamma_{rad} = \frac{2\pi}{\hbar^2} \sum_f \left| \langle f | \hat{H}_{int} | i \rangle \right|^2 \delta(\omega_i - \omega_f). \quad (2.10)$$

Since the quantum dot is smaller than the wavelength of the radiation, it can be approximated as a point dipole. This allows us to write the interaction Hamiltonian as $\hat{H}_{int} = -\hat{\mathbf{d}} \cdot \hat{\mathbf{E}}$ where $\hat{\mathbf{d}}$ is the dipole interaction operator and $\hat{\mathbf{E}}$ is the electric field operator [89] (p. 271). The radiative decay rate can now be written as [89] (p. 276) [89] (p. 512)

$$\gamma_{rad}(\mathbf{r}_0, \omega_0) = \frac{\pi\omega_0}{3\hbar\epsilon_0} \left| \langle g | \hat{\mathbf{d}} | e \rangle \right|^2 \rho(\mathbf{r}_0, \omega_0), \quad (2.11)$$

Chapter 2. Theoretical background

where \mathbf{r}_0 is the emitter location and ω_0 is the frequency of the emitted light from the excited state $|e\rangle$ to the ground state $|g\rangle$ with a local density of states (LDOS) $\rho(\mathbf{r}_0, \omega_0)$. The decay rate allows us to calculating the lifetime since they are each other inverse

$$\tau = \frac{1}{\gamma_{rad}}. \quad (2.12)$$

The emission from the quantum dot is not monochromatic, due to the finite lifetime of the states. The frequency of the emitted light is proportional to the energy, and the uncertainty on the energy is linked to the uncertainty on the time by Heisenberg's uncertainty principle ($\Delta E \Delta t \approx \hbar$ [4] (p. 56 – 57), [89] (p. 280)). If $\Delta t = \tau$ then $1/\tau \approx \Delta E/\hbar = \Delta\omega$, meaning that the linewidth is the inverse of the lifetime. The line shape of the frequency distribution is calculated via the Fourier transform of the far field radiation of a single decay process [89] (p. 279),

$$\frac{\delta W}{\delta\Omega\delta\omega} = \frac{1}{4\pi\epsilon_0} \frac{|\mathbf{d}|^2 \sin^2 \theta \omega_0^2}{4\pi^2 c^3 \gamma_{rad}^2} \left[\frac{\frac{\gamma_{rad}^2}{4}}{(\omega - \omega_0)^2 + \frac{\gamma_0^2}{4}} \right]. \quad (2.13)$$

This is the power radiated in a unit solid angle ($\delta W/\delta\Omega$) per unit frequency interval ($\delta\omega$) where θ is the radiation angle towards the z-axis of the dipole and ω is the radiation frequency. This shows that the line shape of the emission is a prefactor

$$\frac{1}{4\pi\epsilon_0} \frac{|\mathbf{d}|^2 \sin^2 \theta \omega_0^2}{4\pi^2 c^3 \gamma_{rad}^2}$$

multiplied with a Lorentzian line shape [4] (p. 57) [67] (p. 540 – 541)

$$\frac{\frac{\gamma_{rad}^2}{4}}{(\omega - \omega_0)^2 + \frac{\gamma_{rad}^2}{4}}.$$

The full width half maximum of this Lorentzian line shape is γ_{rad} , as predicted via Heisenberg's uncertainty principle. It is also shown that the linewidth of the resonance is limited by the lifetime of the state. It can however be broadened by other effects such as noise and dephasing.

The lifetime of the quantum dot can be altered via two parameters as indicated by Eq. 2.11. The first method is to alter the transition matrix element which describes the coupling between the excited and the ground state. This depends on the material properties and the size of the quantum dot and is therefore determined during the growth of the quantum dot. The second point is the density of states which depends on the environment around the quantum dot. We can make nano-photonic structures around the quantum dot which allows us to alter the lifetime of the quantum dot after the growth of it. The enhancement in the decay rate by photonic structures is the Purcell factor which is the ratio between the

decay rate in the cavity over the decay rate in bulk [4] (p. 203)

$$F_p = \frac{3Q \left(\frac{\lambda}{n}\right)^3}{4\pi^2 V_0}, \quad (2.14)$$

where Q is the cavity quality factor of the nanostructure, λ is the wavelength of light in free space, n is the refractive index of the material and V_0 is the mode volume of the cavity.

2.2.2 Nano-photonic structures for efficient collection

The emission of light from a quantum dot can be altered by embedding it in nano-photonic structures [50, 87, 88], as discussed with the Purcell enhancement. These structures alter the LDOS at the quantum dot and can be designed to enhance emission into a desired optical mode. The two common structures either enhance emission out of plane or enhance emission in plane which is routed to an efficient collection coupler. Common methods to enhance emission out of plane are micropillar cavities [54, 90], photonic nanowires [91] and microlenses [92–94]. Enhancing the emission in plane is commonly done with nano-beam waveguides [95] and photonic crystal waveguides [88, 96–101]. In order to confine the emission in-plane, the nano-structures have to be suspended to confine the light via total internal reflection. This requires a material with a large refractive index for the best confinement. The suspension confines the photons in-plane and the nanostructures determine the direction in the plane.

This thesis is focused on in-plane nano-photonic structures and we describe the two in-plane structure in this section. There is also a description on the micropillar cavities since this is a successful nanostructure for out of plane coupling.

Nanobeam

A schematic of the nanobeam waveguide is shown in Fig. 2.8 where the red bar indicate the nanobeam waveguide and the grey material the bulk sample. The

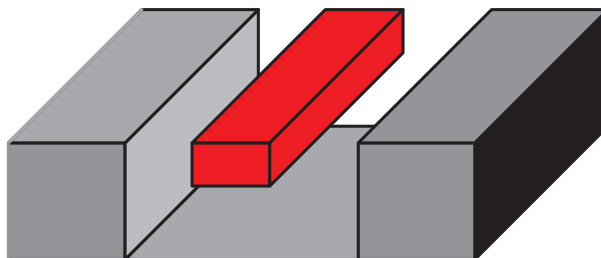


Figure 2.8: Schematic of a suspended nanobeam waveguide (red bar). The grey material represents bulk material of the sample.

nanobeam waveguide is a high refractive index material surrounded by low refractive index material with a predefined cross-section. The confinement of the light in the waveguide occurs due to total internal reflection at the semiconductor-air interface. The larger the contrast in refractive index, the larger the out of plane wave vector for the light has to be to escape the waveguide. The waveguides are typically terminated with a grating coupler or a photonic crystal mirror. This termination is connected to the bulk material to support the waveguide. Longer waveguides are supported by tethers that are designed to minimise scattering of light. Measured Purcell enhancement in a nanobeam waveguides is $F_p \approx 1.6$ [102].

A common material in which these waveguides are fabricated is GaAs, which is deposited on a $\text{Al}_{0.75}\text{Ga}_{0.25}\text{As}$ substrate. The first fabrication step is to pattern the planer structure, which is then etched through the GaAs. The second step is to suspend the GaAs nano-photonic structure which is done by removing the $\text{Al}_{0.75}\text{Ga}_{0.25}\text{As}$ layer below the waveguide.

Photonic crystal waveguide

Another method to engineer the density of states around a quantum dot is by making a photonic crystal around it. A photonic crystal is a regular pattern of two material with a different refractive index. This regular pattern changes the dispersion of light along the direction of the photonic crystal and blocks the prop-

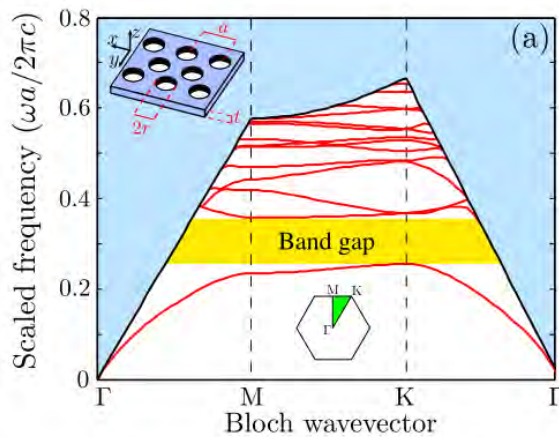


Figure 2.9: Reprinted from [50]. Band diagram of a $2D$ -photonic crystal with a triangular lattice. The frequency is scaled to the lattice parameter a with a hole radius of $a = 3r$ and a membrane height of $t = 2a/3$. The first Brillouin zone is marked in the inset with the symmetry points Γ , M and X and the reduced Brillouin zone in green. The propagation modes are shown as red lines, and the bandgap is marked yellow. The blue area marks the light that is not confined in the slab with the light line as the edge of this area.

agation of certain frequencies into certain directions. There is a frequency range that cannot propagate into any direction through the photonic crystal, which is called the band gap (see Fig. 2.9). The photonic crystal can be in only a limited number of direction, but also in all directions. These can therefore be either $1D$, $2D$ or $3D$, where $1D$ -photonic crystals are typically used as mirrors (So called Bragg-reflectors) and $2D$ and $3D$ photonic crystals are typically used to fabricate waveguides. Figure 2.9 shows the band diagram for a $2D$ photonic crystal in a membrane. The patterning is done by fabricating holes with a low refractive index into a membrane of high refractive index where the holes are placed in a regular triangular lattice. The distance between the holes is the lattice parameter a , the radius of the holes is r and the thickness of the membrane is t . The shown band diagram is for $a = 3r$, $t = 2a/3$ and $n = 3.5$. The bands show the relation between the scaled frequency and the allowed k -vectors where the k -vectors are shown over the first reduced Brillouin zone. The blue area is the light that is not confined by the slab and can escape in vertical direction. The red lines are all the different modes that can propagate through the photonic crystal, and shows that there is an optical frequency range that can not propagate through the photonic crystal.

A waveguide can be fabricated by removing a single line of holes from the photonic crystal. Such a defect allows a mode in the bandgap that can travel through this defect, causing it to be a waveguide. These waveguides can be fabricated around quantum dots. If the quantum dot has an emission frequency in the guided mode, the emission into the waveguide is enhanced. Measured Purcell factors for these structures consists of $F_p = 2$ [103] and $F_p = 5$ [52].

Micropillar cavity

Another structure commonly used to enhance the emission from a quantum dot is a micropillar cavity. This consists of a $1D$ -photonic crystal in the vertical direction, or commonly called a *Distributed Bragg Reflector* (DBR). The quantum dot is located in a defect layer of the DBR, which makes a cavity around the quantum dot. The DBR layers are made with epitaxial growth and the pillar structure is made by etching around the pillar with a typical diameter of 2 to 3 μm . The number of layers above and below the quantum dot is different since a high collection efficiency on a single side is desired. Therefore there are more layers below the quantum dot than above to ensure a higher reflectivity on the bottom to orient the photon to the top. Figure 2.10 shows a schematic of a micropillar structure with 3 DBR layers on the top and 6 DBR layers on the bottom.

The quantum dot in a micropillar cavity can be excited from the top [54] and from the side [105–107]. Excitation from the side allows for an enhancement of the extinction ratio since the laser light propagation is orthogonal to the emission direction from the micropillar. Measured Purcell enhancements in micropillar cavities are $F_p = 5.7$ [108], $F_p = 6.3$ [54] and $F_p = 7.6$ [109].

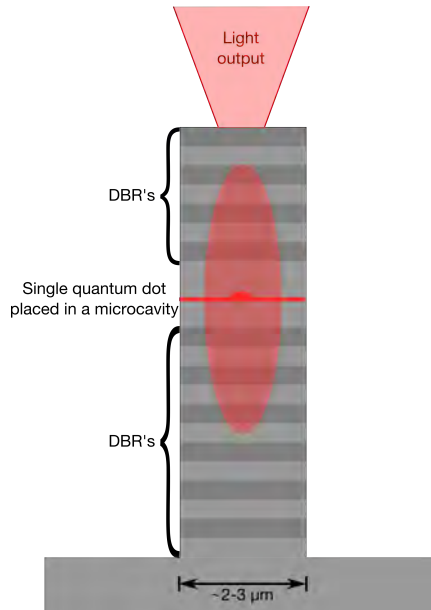


Figure 2.10: Reprint from [104]. Schematic of a micropillar cavity. The quantum dot is located between two Bragg reflectors to create a cavity in the vertical direction. The number of layers on the bottom is bigger than on the top (3 v.s. 6 in the schematic; 15 v.s. 25.5 in [54]). There are less layers on top to orient the emission for collection. The radial emission is confined by the limited diameter of the pillar ($2.5 \mu\text{m}$ in [54]).

2.2.3 Spectral characterisation

The spectral properties from a quantum dot (Sec. 2.2.1) are altered by embedding them in nanostructures. The properties are not only tuned by the nanostructures, but also by the type of exciton and the applied bias voltage across the quantum dot. The applied voltage induces a Stark tuning and can add or remove a charge (electron or hole) from the quantum dot. The stark tuning alters the resonance frequency and the lifetime while the addition or removal of a charges changes the type of exciton. The electron-hole configuration for different excitons are schematically drawn in Fig. 2.11. The green circles (top half) indicate electrons and the white circles (bottom half) indicate holes. The arrows through the electrons and holes indicate the spin state. The recombination between an electron and a hole can only happen if they are in the same energy level and have opposite spin. The numbering of the energy levels is done from the bandgap, thus the first electron state is the lowest energy level in the conduction band while the first hole state is the highest energy level in the valance band. If a electron-hole pair can recombine generating a photon is depending on the spin states of the electron and the hole since their combined spin state result in the angular momentum state of the photon. Generated photon have either an angular momentum of 0 (linear polarised)

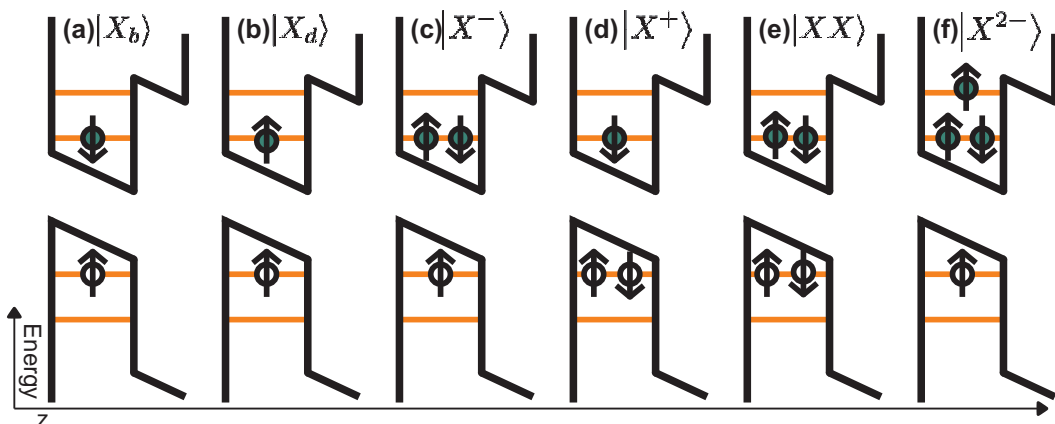


Figure 2.11: Schematic of the electron-hole configuration for different excitons in a quantum dot. **(a)** $|X_b\rangle$ (bright exciton), bright excited state; **(b)** $|X_d\rangle$ (dark exciton), dark excited state; **(c)** $|X^- \rangle$ (negative trion), single negative charged excited state; **(d)** $|X^+ \rangle$ (positive trion), single positive charged excited state; **(e)** $|XX\rangle$ (bi-exciton), double excited state; **(f)** $|X^{2-}\rangle$, double negative charged state. The arrows indicate the spin state and the recombination of an electron and hole require opposite spin states to conserve spin (photons have no spin).

or ± 1 (circular polarised). Electrons have a spin of $\pm 1/2$ and the holes of $\pm 3/2$ (heavy holes) resulting that the electron and hole should have opposite spins. The simplest of excitons are drawn in Fig. 2.11 (a) and (b) since both contain only 1 electron and 1 hole. Figure 2.11 (a) is the bright neutral exciton $|X_b\rangle$ since the electron and hole can recombine while Fig. 2.11 (b) is a dark neutral exciton $|X_d\rangle$ since the spins states prohibit recombination. The bright neutral exciton is also written as X_0 since it has zero net charge. Figure 2.11 (c) and (d) show the single charges excitons (trions). These are a single exciton with an extra charge in the quantum dot where Fig. 2.11 (c) has an extra electron resulting in a negative charged exciton $|X^- \rangle$ and Fig 2.11 (d) has an extra hole resulting in a positive charged exciton $|X^+ \rangle$. It is also possible to have two excitons in the quantum dot simultaneously, which is called a bi-exciton $|XX\rangle$ (Fig. 2.11 (e)). The decay from a bi-exciton always result in a $|X_0\rangle$. The last shown exciton is the double negative charged exciton $|X^{2-}\rangle$ in Fig. 2.11 (f).

The different charged excitons are obtained by tuning valance and conduction band slope with the applied bias voltage resulting in different capture rates for electrons and holes in the quantum dot. Every exciton has different behaviour in the lifetime and resonance frequency since the Coulomb interaction shifts the energy state of the electrons and holes. The variation in emission wavelength can result in differences of a few nanometer. The dark exciton state is influenced in the lifetime, which has to be long since the spin prohibits them from recombining.

The rest of this work focuses on the bright exciton $|X_b\rangle$ and the negatively charged exciton $|X^- \rangle$. The bright exciton is a transition that can be split up again in two different excitons, determined by the dipole moment [50]. Equation 2.11 shows that the decay rate of a transition depends on the dipole moment, allowing the differentiation between the x-dipole and y-dipole of the $|X_b\rangle$. The dipole coupling and energy level is different for both dipoles due to material properties which results in fine structure splitting [110–113]. This effect lifts the degeneracy between the the x and y-dipole, resulting in two different energy levels for the two transitions. Trions are not affected by this splitting of the degeneracy and have only a single energy level [50], assuming that no magnetic field is applied. The two different dipoles are also affected differently by nanostructures resulting in different Purcell enhancements to the two dipoles.

The method to measure the lifetime and linewidths are equal for the different excitons where the type of exciton is selected with this bias voltage. The linewidth of an exciton is measured resonantly, and can be done via different methods. The methods used in this thesis are *Resonant Transmission* (RT) and *Resonant Fluorescence* (RF). Both measurements require a narrow linewidth laser (CW) where the frequency is scanned across the quantum dot resonance. For RT the quantum dot has to be embedded in a waveguide with a coupler on both sides since the laser is attenuated to a single photon level and coupled into the waveguide. The laser photons interact with the quantum dot while travelling through the waveguide and the other coupler then sends the transmitted photons to a single photon detector. This difference between RT and RF is schematically shown in Fig. 2.12, where RF excited the quantum dot from the top while RT travels through the waveguide and interacts with the quantum dot.

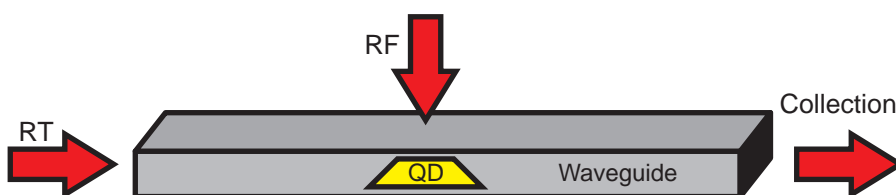


Figure 2.12: Difference between *Resonant Transmission* (RT) and *Resonant Fluorescence* (RF) linewidth measurements on a quantum dot. Both cases have the quantum dot embedded in a waveguide where RT requires a coupler on both sides while RF only needs a coupler on one side. In RT an attenuated laser is coupled into the waveguide, interacts with the quantum dot while traversing through the waveguide and coupled to a single photon detector by the other coupler. In RF is the quantum dot excited from the top. The emitted photon due to the decay is then sent to a single photon detector via a coupler at the end of the waveguide. To obtain the line shape, the used laser is swept in frequency.

In both cases we measure the count rate depending on the laser frequency. The profile of this count rate is the convolution of the exciton resonance with the laser linewidth if we assume no noise. This occurs since the count rate at a certain laser frequency is the interaction of the laser light with the exciton. In Sec. 2.2.1 we derived that the frequency profile is a Lorentzian and this profile determines the interaction strength between the laser light and the exciton. Since the linewidth of the laser is narrow, we probe the Lorentzian linewidth which then appears in the measured count rate when the laser frequency is swept. The construction of the line shape and how the interaction works is described below.

Resonance fluorescence

In resonance fluorescence (RF) [114, 115] the quantum dot is excited by a laser with the same energy as the transition energy. The quantum dot decays back to the ground state with the emission of a photon into the waveguide. This photon is collected via a coupler and sent to a single photon detector. Due to the vast number of laser photons, some of these are collected too. This requires filtering between the emitted photons from the quantum dot and the laser photons, which can be done by polarisation. Increasing the laser power increases the emitted photons as long as the laser is in the weak-field approximation. When the laser power is increased into the strong-field limit, we can observe coherence effect between the laser and the exciton. These coherence effects induce Rabi Oscillations [4] (p.177), which are oscillations in the emitted photons depending on the laser power. There is a power with maximum efficiency which is called π -pulse excitation.

Spectral characterisation is performed in the weak coupling regime. Measuring these properties in RF introduces challenges since the detector can not discriminate between emission photons and laser photons. This can be solved by filtering the light on a property where the laser and photons are different, such as polarisation. The photons emitted from the waveguide obtain a well-defined polarisation, while the laser is scattered light from the surface and laser coupled to the waveguide. The laser coupling to the waveguide can be minimised by optimising the input laser polarisation to couple minimally to the waveguide. The scattered laser light is filtered out in the collection path since most scattered light is still polarised. The ratio between the emission photons and the laser photons is the extinction ratio and can be measured by setting the laser at the frequency desired to measure on and change the applied bias voltage over the quantum dot between on-resonance and off-resonance. Emission count from the quantum dot are only expected when the laser and quantum dot are on-resonance with each other. The difference in count rate between the on-resonance and off-resonance is therefore the emission rate from the quantum dot. The extinction ratio can then be calculated by dividing the emission rate by the background counts which is the count

rate when the quantum dot is off-resonance. This results in an extinction ratio of

$$Ext = \frac{I_{on} - I_{off}}{I_{off}}, \quad (2.15)$$

where I_{on} is the photon count rate when the quantum dot and laser are on-resonance and I_{off} is the photon count intensity when the quantum dot and laser are off-resonance.

Resonance transmission

Another method to measure the linewidth of a quantum dot is by performing resonance transmission. This requires a waveguide with a coupler on both sides, since the laser has to be transmitted through the waveguide containing the quantum dot. The coherent laser field interacts with the quantum dot, reflecting the single photon components and transmitting the multi photon components [102, 116–119]. This yields a method to find the exciton linewidth by scanning the resonance with a laser. The larger the interaction between the laser and the quantum dot, the more likely the single photon components are reflected and thus the lower the detection rate. The resonance profile of the quantum dot is a measure of the interaction with light of that frequency and therefore the reduction in count rate depending on the laser frequency yields the line shape. The count rate has to be corrected for frequency dependencies of the couplers and waveguide. The linewidth is therefore determined from the normalised transmission which is obtained from the ratio of when the quantum dot and laser are on-resonance versus off-resonance. The tuning in and out of resonance is done by changing the bias voltage between values where the quantum dot is on-resonance versus off-resonance. This results in a normalised transmission of

$$T_{norm} = \frac{I_{on}}{I_{off}}, \quad (2.16)$$

where I_{on} and I_{off} are the same as in equation 2.15. This allows us to define a transmission dip visibility, which is the maximum value of $1 - T_{norm}$.

This method of measuring linewidths is less sensitive to laser scattering since the couplers are optimised to couple light in and out of the waveguide. The power used for RT is also orders of magnitude lower than for RF since we require single photon components from the coherent state. The problem is that RT yields lower count rates and the edges of the waveguide can form a cavity. If the quantum dot resonance is not aligned with the cavity resonance, the line shape becomes a Fano line shape [102, 116, 119]. The linewidth however remains equal.

Measuring quantum dot lifetime

The lifetime is measured by exciting the quantum dot with a narrow pulsed laser, and measure the time it takes for the quantum dot to decay and emit a photon. This time is measured by recording the time a laser pulse was generated and the

time when a emission photon was detected. The time difference between these two events is stored. This can be done many times to construct a histogram of all the time differences to show the decay dynamics. Every excited state has an exponential decay with a life time given in Eq. 2.12 and an amplitude decay given by $C(t) = e^{\frac{-t}{2\tau}}$ [67] (p. 539) where $C(t)$ is the amplitude probability of the excited state and t is the elapsed time since the excitation. What we measure in the lab is the probability $P(t) = |C(t)|^2 = e^{\frac{-t}{\tau}}$. If the decay consists of multiple decay paths (e.g. x and y-dipole for the neutral exciton), the exponential decays are added

$$P(t) = \sum_n p_n \cdot e^{\frac{-t}{\tau_n}}, \quad (2.17)$$

where P_n is the relative probability of that decay and τ_n the lifetime of the individual decay. This shows that the neutral exciton has a bi-exponential decay due to the x and y-dipole and that the trion is a single exponential decay. Lifetime can be measured with different excitation methods (Fig. 2.7), where the different lies in the preparation of the state.

2.3 Single photon characterisation

Single photons are not only characterised by their spectrum, but also by their purity and indistinguishability. The source generating these photons is further characterised by the generation efficiency of these photons. This section discusses the different properties starting with the generation efficiency from a source (Sec. 2.3.1). Section 2.3.2 discusses the single photon purity and Sec. 2.3.3 the indistinguishability. Section 2.3.4 shows a method to calculate the source efficiency and purity from a quantum dot via rate equation modelling.

2.3.1 Source efficiency

Generating single photons is ideally a deterministic process, but in reality losses play a role. The quantum dot source is excited with a narrow pulse laser (< 10 ps) with a fixed repetition rate (F_{rep}). Due to the deterministic nature, every pulse should yield a single photon from the decay of the excited state (Sec. 2.2.1). The source efficiency describes the probability to obtain a photon from a single excitation. The single photon rate collected from the source is given by I_{cts} , resulting in a source efficiency

$$\eta_{source} = \frac{I_{cts}}{F_{rep}}. \quad (2.18)$$

This is the ratio between obtained photons and excitation pulses, and includes all losses. These losses can be divided in three major categories, the preparation efficiency of the quantum dot p_e , the waveguide collection efficiency β -factor and the optical transmission T (including coupling efficiencies).

The preparation efficiency (p_e) of the quantum dot is the probability that the quantum dot is excited to the target state and that radiative decay results in a photon from the desired exciton. If the quantum dot is excited non resonantly, the quantum dot can relax into a different exciton states. The decay can be measured with a spectrometer from which the intensity in the desired wavelength range can be compared to the total measured intensity. The ratio of these yield the preparation efficiency p_e .

The next step in the source efficiency is the collection of the emitted photons into the waveguide, which is given by the β -factor [52]

$$\beta = \frac{\Gamma_{wg}}{\Gamma_{wg} + \Gamma_{rad} + \Gamma_{non-rad}}, \quad (2.19)$$

where Γ_{wg} is the decay rate into the waveguide, Γ_{rad} is the radiative decay rate not collected by the waveguide and $\Gamma_{non-rad}$ is the non radiative decay rate. The β -factor is the decay into the waveguide divided by the total decay from the desired exciton.

After the photon is coupled to the waveguide, it travels through the waveguide and is collected by optical components. Propagation losses of the waveguide are influenced by the intrinsic losses of the waveguide and by the quality of fabrication. Measured losses are in the range of $6.6 \pm 0.5 \text{ dB/mm}$ [120] to 0.16 dB/mm [121]. The photons are coupled out of the waveguide and different techniques are investigated to maximise the coupling efficiency (η_{oc}). Possible (but not all) strategies are evanescent coupling [122–127], end-fire inverted tapers [52, 128] and grating scattering [52, 129–132]. After the photons are coupled out of the waveguide, they travel through optical components to be prepared for the setup after the gate. This efficiency can be measured classically by sending in a laser and measure the input power (P_{in}), followed by measuring the output power (P_{out}) and take the ratio of these two.

2.3.2 Single photon purity

The single photon purity is the probability to obtain a single photon in a predefined time interval. In case of a pulsed single photon source this is the probability to have a single photon in the interval of the excitation. The purity can be conditioned by selecting only the time intervals in which a photon was detected, removing all time intervals without a photon from the statistics. If we take $P(n)$ as the probability of having n photons, the unconditioned single photon purity is $P(1)$ and the conditioned single photon purity is $P(1)/(1 - P(0))^\dagger$.

This shows that the single photon purity is depending on the distribution of photon number states. A common distribution of photon states is the coherent state

[†] $\sum_n P(n) = 1$

which describes the photon statistic of a laser. This is a Poissonian photon distribution of [4] (p. 159) [133]

$$P(n) = \frac{\bar{n}^n}{n!} e^{-\bar{n}}, \quad (2.20)$$

where \bar{n} is the mean photon number. Another common distribution is the Boltzmann distribution, describing photons from a thermal source. This is given by [4] (p. 85)

$$P(n) = \frac{1}{\bar{n} + 1} \left(\frac{\bar{n}}{\bar{n} + 1} \right)^n. \quad (2.21)$$

Pure photon states are given by Fock states, where the exact number of photons is known. This is described by

$$P(n) = \delta(n - \bar{n}). \quad (2.22)$$

A Poissonian state with a large mean photon number can be approximated as a Gaussian distribution, which is the typical photon number distribution of random light. Measuring photon number states of more than 1 photon in a deterministic fashion is non trivial, despite the existence of photon resolving detectors [134–136]. Measuring the full probability distribution of all the different photon number states is therefore a hard task to perform to obtain the single photon purity. There is however a different techniques to determine the single photon purity, the second order correlation function ($g^{(2)}$) which correlates different times of a signals with each other via [4] (p. 111)

$$g^{(2)}(t, \tau) = \frac{\langle I(t)I(t + \tau) \rangle}{\langle I(t) \rangle \langle I(t + \tau) \rangle} \quad (2.23)$$

where $I(t)$ is the intensity on time t and τ is the time delay in the signal. The expectation value does not depend on the time delay resulting in $\langle I(t) \rangle = \langle I(t + \tau) \rangle$ yielding [89] (p. 320) [133]

$$g^{(2)}(t, \tau) = \frac{\langle I(t)I(t + \tau) \rangle}{\langle I(t) \rangle^2} \quad (2.24)$$

Equation 2.24 assumes the correlation of a signal at two different times. To achieve this we must split our signal and add a delay to one of the two detection paths. The setup that can measure the second order correlation function is the *Hanbury-Brown-Twiss* (HBT) setup, which is schematically represented in figure 2.13. The stream of photons enters a 50 : 50 beamsplitter and both paths are sent to a single photon detector. These detectors sent a signal when a photon impinged on it and the signal from the detectors are correlated with each other. The signal from one of the two detectors has a tuneable time delay τ and the signals are correlated to each other according to Eq. 2.23. Transforming this equations to the single photon regime requires the intensities to be replaced by number operators, resulting in [137]

$$g^{(2)}(t, \tau) = \frac{\langle \hat{a}^\dagger(t)\hat{a}^\dagger(t + \tau)\hat{a}(t)\hat{a}(t + \tau) \rangle}{\langle \hat{a}^\dagger(t)\hat{a}(t) \rangle \langle \hat{a}^\dagger(t + \tau)\hat{a}(t + \tau) \rangle}. \quad (2.25)$$

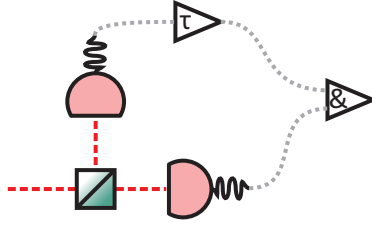


Figure 2.13: HBT setup with light being split by a 50:50 beamsplitter and sent to a detector on both arms. One of the detectors can apply a time delay τ to the signal to correlated it over different time delays.

Time t is an exact time but the second order correlation function correlates a signal with a different time of itself. The exact time can therefore be set to $t = 0$ since only the time difference is relevant. two signals with each other using only a relative time between the two signals. We can therefore take an arbitrary value for t , including $t = 0$. This results in an equation giving the correlation between the two detectors with a time delay τ .

The correlation measurements can be mode in either a pulsed excitation or a continuous excitations. The difference in the second order correlation function is that pulsed excitation results in pulses in the second order correlation function. Th reason for that is that if we excite with a time difference between the pulses of $\Delta\tau$, the coincidences occurs when τ is a integer multiplication of $\Delta\tau$.

The second order correlation function is by definition normalized to the total power. Light with a random photon distribution and no power fluctuations result in no correlations between the detectors and obtain a $g^{(2)}(\tau \rightarrow \infty) = 1$ [4] (p. 111). Pulses of photons have by definition power fluctuations since we can only obtain photons during the pulses. Random light with fixed pulsing result then that the height of the peaks at $g^{(2)}(\tau \gg) = 1$, due to the normalisation. This normalisation to uncorrelated light renders the $g^{(2)}(0)$ as a parameter to distinguish different sources where it is either equal, bigger or smaller than one. This categorisation occurs because the $g^{(2)}(0)$ represent the correlation of a signal with itself, which in a quantum regime results in the likelihood to have multiple photons at the same time. Since $g^{(2)}(0) = 1$ means a random distribution, there is a random probability to have more than one photon while if $g^{(2)}(0) > 1$, it is more likely to measure a photon on the second detector if the first detector measured a photon (bunching of photons). If the photon number follows the Boltzmann distribution the measured $g^{(2)}(0) > 1$. If $g^{(2)}(0) < 1$, the second detector is less likely to have a detection event if the first detector measured a photon (antibunching of photons). When $g^{(2)}(0) = 0$ there were no coincidence between detector one and two, meaning only pure single photons could be inserted in the HBT-setup. The terms (anti)bunching comes from the principle that there is either a higher or a lower probability to detect a second photon when the first photon was detected and they

are therefore bunched or antibunched. Since the $g^{(2)}(0)$ is a measure of the probability to have multiple photons at the same time, it can be used to characterise the number of photons emitted by a quantum dot source [138] (p. 174)

$$g^{(2)}(0) = \frac{n-1}{n}. \quad (2.26)$$

2.3.3 Indistinguishability

Single photons have to be indistinguishable from each other to be useful in most applications. This indistinguishability between photons can be measured with a *Hong-Ou-Mandel* (HOM) setup, which is schematically shown in Fig. 2.14. A HOM setup consists of a 50 : 50 beamsplitter with a detector in the two output modes. Both input modes contain a single photon which are interfered with each other on the beamsplitter. Labelling the input paths as path a and b and the outputs paths as c and d , the beamsplitter operation can be written as

$$\begin{pmatrix} \hat{c}^\dagger \\ \hat{d}^\dagger \end{pmatrix} = \frac{1}{\sqrt{2}} \begin{bmatrix} 1 & i \\ i & 1 \end{bmatrix} \begin{pmatrix} \hat{a}^\dagger \\ \hat{b}^\dagger \end{pmatrix}. \quad (2.27)$$

where \hat{a}^\dagger , \hat{b}^\dagger , \hat{c}^\dagger and \hat{d}^\dagger are the photon creation operators in the four different paths.

When two identical photons enter the beamsplitter via path a and b , the input state can be written as $\hat{a}^\dagger \hat{b}^\dagger |0, 0\rangle$. Enacting the beamsplitter operation on this input state results in an output state of $\frac{i}{2} (\hat{c}^\dagger \hat{c}^\dagger + \hat{d}^\dagger \hat{d}^\dagger) |0, 0\rangle$, showing that the output state is bunched with either both photons in path c or both photons in path d . This shows that the two detectors will never detect a photon at the same time, thus there is never a coincidence count between the detectors. The two photons can be made (partly) distinguishable by adding a time delay to one of the two photons, as shown in Fig. 2.14 which has a time delay in path b . Increasing this time delay sufficient results in completely distinguishable photons. The output photons are labelled by their input port yielding the state

$$\frac{i}{2} (\hat{c}_a^\dagger \hat{c}_b^\dagger - i \hat{c}_a^\dagger \hat{d}_b^\dagger + i \hat{d}_a^\dagger \hat{c}_b^\dagger + \hat{d}_a^\dagger \hat{d}_b^\dagger) |0, 0\rangle.$$

If the time window to measure coincidences is longer than the time difference between the photons, we measure a coincidence between the detectors in 50% of the cases.

The time delay added in path b can make the photons partial indistinguishable and we define the time window for the coincidence to be larger than the time difference between the photons. The partial indistinguishability is denoted by Q , and results in the transformations

$$\begin{aligned} \hat{a}^\dagger &\mapsto \left[\sqrt{Q} (\hat{c}_I^\dagger + i \hat{d}_I^\dagger) + \sqrt{1-Q} (\hat{c}_a^\dagger + i \hat{d}_a^\dagger) \right] \frac{1}{\sqrt{2}} \\ \hat{b}^\dagger &\mapsto \left[\sqrt{Q} (i \hat{c}_I^\dagger + \hat{d}_I^\dagger) + \sqrt{1-Q} (i \hat{c}_b^\dagger + \hat{d}_b^\dagger) \right] \frac{1}{\sqrt{2}} \end{aligned} \quad (2.28)$$

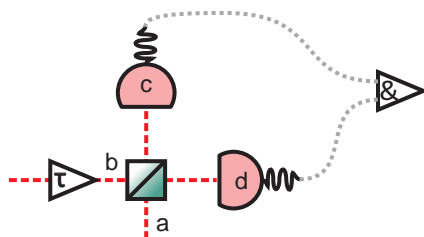


Figure 2.14: HOM-setup to measure the indistinguishability of two photon. Port a and b are the inputs where port b has an option to delay the photon. Port c and d are the output ports of the beamsplitter and contain a detector. If the photons are perfectly indistinguishable, there will be no coincidence counts between the detector, while perfectly distinguishable photon have a coincidence count in 50% of the measurements.

where the distinguishable output modes are marked by the subscript a and b , which denotes the input port it originates from. The subscript I denotes the indistinguishable part of the photons. This is also the part that interferes in the beamsplitter. If $Q = 1$ the state is identical to the perfectly indistinguishable case, and setting $Q = 0$ results in the perfectly distinguishable situation. Taking the input case of $\hat{a}^\dagger \hat{b}^\dagger$, the transformation results into

$$\begin{aligned}
 \hat{a}^\dagger \hat{b}^\dagger \mapsto & \frac{i}{2} Q \left(\hat{c}_I^\dagger \hat{c}_I^\dagger + \hat{d}_I^\dagger \hat{d}_I^\dagger \right) + \\
 & \frac{i}{2} (1 - Q) \left(\hat{c}_a^\dagger \hat{c}_b^\dagger - i \hat{c}_a^\dagger \hat{d}_b^\dagger + i \hat{d}_a^\dagger \hat{c}_b^\dagger + \hat{d}_a^\dagger \hat{d}_b^\dagger \right) + \\
 & \frac{1}{2} \sqrt{Q(1-Q)} \left(i \hat{c}_I^\dagger \hat{c}_b^\dagger - \hat{d}_I^\dagger \hat{c}_b^\dagger + \hat{c}_I^\dagger \hat{d}_b^\dagger + i \hat{d}_I^\dagger \hat{d}_b^\dagger \right) + \\
 & \frac{1}{2} \sqrt{Q(1-Q)} \left(i \hat{c}_I^\dagger \hat{c}_a^\dagger + \hat{d}_I^\dagger \hat{c}_a^\dagger - \hat{c}_I^\dagger \hat{d}_a^\dagger + i \hat{d}_I^\dagger \hat{d}_a^\dagger \right).
 \end{aligned} \tag{2.29}$$

This shows again that $Q = 1$ yields the perfectly indistinguishable outcome while $Q = 0$ results in the perfectly distinguishable outcome. There is however a part which only occur in partly distinguishable photons. The indistinguishability can be measured by applying a delay to path b resulting in the indistinguishability parameter Q to be dependent of τ . If the detectors at path c and d are perfect number resolving detectors, the detection probability of the three different states ($|2_c, 0_d\rangle$, $|0_c, 2_d\rangle$, $|1_c, 1_d\rangle$) can be calculated. We are interested in either a $|1_c, 1_d\rangle$ or the sum of the $|2_c, 0_d\rangle$ and $|0_c, 2_d\rangle$ state, which probabilities depending Q are plotted in Fig. 2.15 (a). Most detectors are non number resolving detectors and we can only measure the $|1_c, 1_d\rangle$ by having a coincidence count. The $|2_c, 0_d\rangle$ and $|0_c, 2_d\rangle$ can not be measured.

We now have a tool to link the indistinguishability to the probability to measure a coincidence. This can be used in a experimental scenario where we have losses in the system and a unknown indistinguishability between two photons. We use

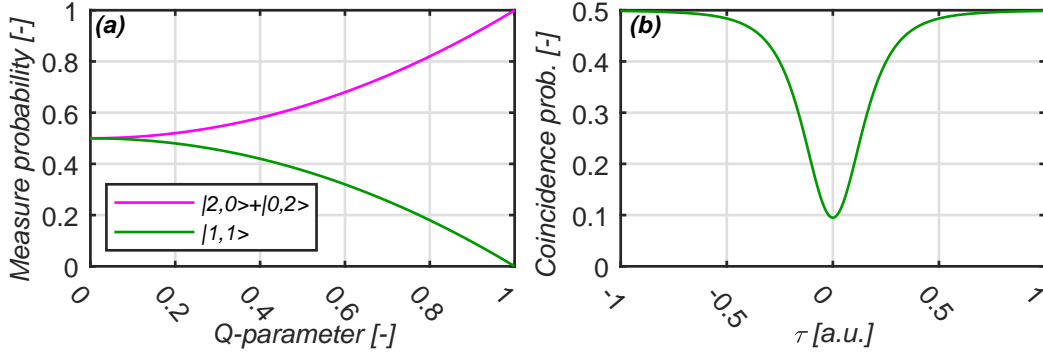


Figure 2.15: **(a)** Relation between the Q-parameter for indistinguishability and the probability to measure a coincidence between output c and d (green) and to measure a twofold on c or d (magenta). The more indistinguishable the photons are, the less coincidence will be measured. **(b)** The coincidence probability for photons with an arbitrary linewidths and a maximum Q-parameter of 0.9. The Q-parameter is approximated by a Lorentzian with a FWHM of 0.5 a.u. .

the principle of changing the time delay between the two photons to make them fully distinguishable and then change it to the best indistinguishability as possible. The probability to measure a coincidence can not be directly deduced due to the losses in the setup, but we can measure the coincidence count rate depending on the time delay. When the time delay is set to have fully distinguishable photons, the measured coincidence count rate can be used to normalise to the 50% probability of measuring a coincidence. After that the time delay is varied resulting in a point where the coincidence rate is minimised. Applying the normalisation results in the probability of a coincidence at that time delay, which can be translated to the Q-parameter.

The indistinguishability dependency on the delay is Lorentzian in this type of setup since we make a convolution of two exponential decays. Taking an example of $Q = 0.9$ and a Lorentzian *Full width Half Maximum* (FWHM) of 0.5τ , the expected outcome of such an experiment is shown in Fig. 2.15 (b).

Experiments normally show the HOM-visibility (V_{HOM}), which is $V_{HOM} = 1 - C_{min}/C_{max}$ where C_{min} and C_{max} are the lowest and highest measured coincidence rates. The HOM visibility is related to the Q parameter via $V_{HOM} = Q^2$ since $V_{HOM} = 1 - 2P_{\text{coin},\text{min}}$ and $P_{\text{coin},\text{min}} = 1 - Q^2/2$ where $P_{\text{coin},\text{min}}$ is the lowest probability to measure a coincidence.

2.3.4 Rate equation modelling

The last section is related to the source efficiency (Sec. 2.3.1) and the second order correlation function (Sec. 2.3.2). This is about rate equations, which is a

tool to calculate the source efficiency and the $g^{(2)}(\tau)$ based on an N -level system with known pumping and decay rates. This requires some assumptions which are typically fulfilled in general situations. The first assumption is that there are no Markovian processes, thus we can map every effect onto a state in the quantum dot. Secondly we assume that the probability to emit a photon is directly related to the population of the excited state.

The modelling is set up via coupled differential equation, where every state is a node in the differential equation and the rates are coupling parameters. We follow the case of a three level system, where we assume a ground state (n_g), an exciton state (n_e) and an aboveband state (n_a). This quantum dot is excited from the ground state to the aboveband state, relaxes into the exciton state and then radiatively decays into the ground state. Figure 2.16 shows a schematic of this model representing the 3 states and 3 rates. The differential equation is set as

$$\begin{aligned}\dot{n}_a &= -\gamma_{ae}n_a + \gamma_{ga}n_g \\ \dot{n}_e &= -\gamma_{eg}n_e + \gamma_{ae}n_a \\ \dot{n}_g &= -\gamma_{ga}n_g + \gamma_{eg}n_e\end{aligned}\tag{2.30}$$

where \dot{n} is the population change of this state, n is the population of this state and γ is the rate between two the states denoted in the subscript. Solving this system can be done via matrix calculation in the form of

$$\begin{pmatrix} \dot{n}_g \\ \dot{n}_e \\ \dot{n}_a \end{pmatrix} = \begin{bmatrix} -\gamma_{ga} & \gamma_{eg} & 0 \\ 0 & -\gamma_{eg} & \gamma_{ae} \\ \gamma_{ga} & 0 & -\gamma_{ae} \end{bmatrix} \begin{pmatrix} n_g \\ n_e \\ n_a \end{pmatrix}.\tag{2.31}$$

The eigenvalues of the matrix are the time constants in the differential solution, and the eigenvectors are the vectorial values. The outcome of a differential equation has a constant for every term, which can be determined from the initial condition. This is commonly,

$$\begin{pmatrix} n_g \\ n_e \\ n_a \end{pmatrix} (t = 0) = \begin{pmatrix} 1 \\ 0 \\ 0 \end{pmatrix}.$$

This assumes that all the population is initially in the ground state. The initial condition has no effect on the calculation of the source efficiency but will have an effect on the $g^{(2)}(\tau)$. We look at the steady state condition ($t = \infty$) to find the source efficiency depending on the excitation power. This efficiency is the population in the excited state (n_e). Doing this result in

$$\begin{aligned}n_e(t \mapsto \infty) &= \frac{\gamma_{ga}\gamma_{ae}}{\gamma_{ga}\gamma_{eg} + \gamma_{ga}\gamma_{ae} + \gamma_{eg}\gamma_{ae}} \\ &= \frac{\gamma_{ae}}{\gamma_{eg} + \gamma_{ae}} \frac{\gamma_{ga}}{\gamma_{ga} + \frac{\gamma_{ae}\gamma_{eg}}{\gamma_{ae} + \gamma_{eg}}}.\end{aligned}\tag{2.32}$$

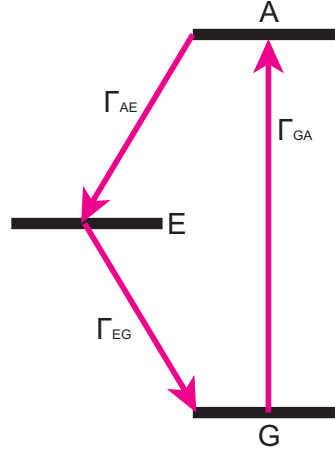


Figure 2.16: Three level system used in the example for the rate equation modelling. The 3 states and 3 rates are shown in the model.

γ_{ae} and γ_{eg} are constant since they are the relaxation time from the aboveband state to the exciton state and the decay from the exciton to the ground state. The pumping is given by γ_{ga} , which depends on the laser power (P). The steady state solution of the probability to be in the excited state can be written as a dependency of the pumping power via

$$n_e(P) = \eta_0 \left(\frac{P}{P + P_{sat}} \right), \quad (2.33)$$

where η_0 is the steady state efficiency and P_{sat} is the saturation power. This equation shows that the saturation behaviour follows a logistic function. In an experimental setup is the count rate measured which allows to determine the saturation power by measuring the count rate depending on excitation power. The efficiency η_0 is now exchanged for the measured count rate since these two are directly related to each other. The measured count rate then follows

$$I_{QD}(P) = I_0 \left(\frac{P}{P + P_{sat}} \right), \quad (2.34)$$

where I_0 is the maximum measured count rate.

A quantum dot has many states that do not all decay radiatively, which are called dark states. When an excited quantum dot is in such a dark state, it can not decay resulting in no photons generated. If the lifetime of such a dark state is longer than the repetition of the excitation, the dark state shows periods of time where a photon can not be emitted. This results in photon bunching on the timescales of the lifetime of a dark state. This bunching results in an enhanced $g^{(2)}(\tau)$ where it is possible to obtain $g^{(2)}(\tau \neq 0) > 0$. This can be calculated with rate equation modelling, since it is effectively an extra state in the model with a population and lifetime.

The $g^{(2)}(\tau)$ can be extracted from the rate equation model by evaluating the population of the excited state over time. The population shows the probability to emit a photon after a time t , where $t = 0$ is the moment when the laser is turned onto the quantum dot. When $t \rightarrow \infty$ the emission from the quantum dot is assumed uncorrelated to the starting time and should have a $g^{(2)} = 1$. If $n_e(t) \neq n_e(\infty)$, that the probability to obtain a photon at time t is either higher or lower than when it is random. This is equal to how the $g^{(2)}(\tau)$ operates, resulting in [139] (p. 334)

$$g^{(2)}(\tau) = \frac{n_e(t = \tau)}{n_e(t \mapsto \infty)}. \quad (2.35)$$

This procedure only extracts the second order correlation function from a simple model and does not actually calculate the auto-correlation. Calculation the auto-correlation would require the full master equation.

Current calculations assumed a weak electric field (low laser power), but can be extended to a strong electric field. A strong electric field induces coherence between the ground state and the excited state. To describe this with the same type of modelling, coherence states have to be introduced to describe the coherence. The states used in the calculation are now the equations of motion for the density matrix, which results in the optical Bloch equations for a two level emitter [140] (p.178). These are still a set of linear differential equations as earlier in this section, but the difference is that they have complex numbers. This is however not a limitation to the solving process of the system of equations, since the only requirement is that the system of equations is linear. This makes the rate equation modelling a strong tool to calculate source efficiencies since it can be expanded to coherent system, as long as the equation of motion are a set of linear differential equations.

2.4 Parametric down conversion sources

Most of this chapter focuses on single photon generation from quantum dot sources. Another commonly used process is *Spontaneous Parametric Down Conversion* (SPDC), which is based on a non-linear susceptibility. The susceptibility (χ) is the relation between the polarisation of a material and the electric field. Most materials are considered to be linear yielding a relation between the polarisation and electric field of $\tilde{P}(t) = \epsilon_0 \chi^{(1)} \tilde{E}(t)$, where $\tilde{P}(t)$ is the polarisation, ϵ_0 is the permittivity, $\tilde{E}(t)$ is the time dependent electric field and $\chi^{(1)}$ is the linear susceptibility [141] (p. 2). A non linear material has a susceptibility acting to the electric field to a power bigger than one, which adds terms to the polarisation via [141] (p.2) [142] (p.876)

$$\begin{aligned} \tilde{P}(t) &= \epsilon_0 \left[\chi^{(1)} \tilde{E}(t) + \chi^{(2)} \tilde{E}^2(t) + \chi^{(3)} \tilde{E}^3(t) \right] \\ &\equiv \tilde{P}^{(1)}(t) + \tilde{P}^{(2)}(t) + \tilde{P}^{(3)}(t), \end{aligned} \quad (2.36)$$

where $\chi^{(2)}$ and $\chi^{(3)}$ are the second and third order susceptibility. Linear materials are considered to have a non-linear susceptibility significantly small so that it can be negligible.

For non-linear materials the polarisation can be written in a linear and a non-linear term $\tilde{\mathbf{P}} = \tilde{\mathbf{P}}^{(1)} + \tilde{\mathbf{P}}^{NL}$ [141] (p.72) The wave equation has to be fulfilled for every ω_n , resulting in [141] (p.73)

$$-\nabla^2 \tilde{\mathbf{E}}_n + \frac{\epsilon^{(1)}(\omega_n)}{c^2} \frac{\partial^2 \tilde{\mathbf{E}}_n}{\partial t^2} = -\frac{1}{\epsilon_0 c^2} \frac{\partial^2 \tilde{\mathbf{P}}_n^{NL}}{\partial t^2} \quad (2.37)$$

where c is the speed of light and $\epsilon^{(1)}$ the linear relative permittivity.

The non-linear element in equation 2.37 allows the mixing of different frequencies to generate light with new frequencies. The number of waves allowed to be mixed depend on the order of non-linearities that is sustained by the material where a material with significant $\chi^{(2)}$ (so called $\chi^{(2)}$ -medium) allows for mixing of three waves and a material with significant $\chi^{(3)}$ (so called $\chi^{(3)}$ -medium) allows the mixing of four waves.

The conversion of light has to fulfil the law of energy conservation ($\Delta\omega = 0$) and the law of momentum conservation ($\Delta k = 0$). Different cases of *Spontaneous Parametric Conversion* are shown in Fig. 2.17 with (a) SPDC, (b) *Sum Frequency Generation* (SFG) and (c) *Four wave Mixing* (FWM). The relations for energy conservation and momentum conservation are given below and show that Δk ($\Delta\omega$) is the difference between the light pumped in and the light generated.

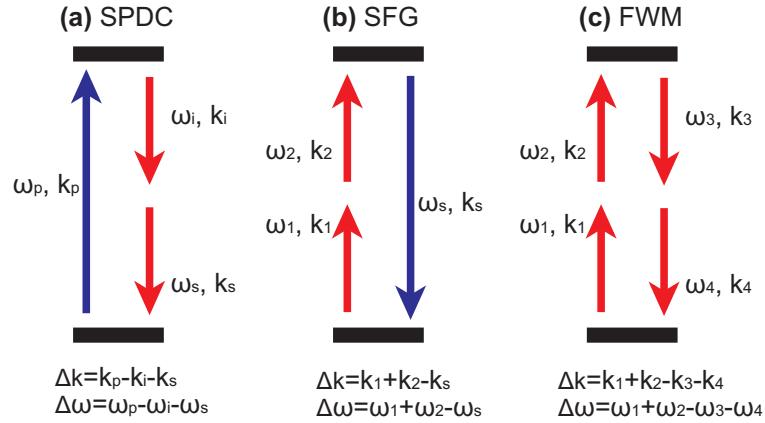


Figure 2.17: Schematics for different *Spontaneous Parametric Sources* with (a) *Spontaneous Parametric Down Conversion* (SPDC), (b) *Sum Frequency Generation* (SFG) and (c) *Four wave Mixing* (FWM). SPDC and SFG mixes three waves and require a $\chi^{(2)}$ while FWM mixes four waves and requires a $\chi^{(3)}$. The energy and momentum conservation relations are given for all three cases.

The conservation of momentum is also called the phase relation and holds for an infinite long interaction length with the non-linear material. For a material with a finite size, the phase relation has a conversion efficiency depending on Δk that is given by [141] (p.79)

$$\eta_{conv} = \text{sinc}^2 \left(\frac{\Delta k L}{2} \right) \quad (2.38)$$

where L is the interaction length of the light with the non-linear medium. This shows that the conversion efficiency is depending on the phase mismatch following a sinc-function. There are therefore local maxima for the efficiencies in the phase relation, so called side lobes. By polling the non-linear material, an extra phase term can be added to the phase relation. This allows the modification of wave vectors with the maximum conversion efficiency to match the energy of the light.

A common single photon source is the SPDC source which has the phase relation and energy conservation given in Fig. 2.17 (a). The non-linear crystal is pumped with a single laser, from which a photon is converted into two other photons called the signal and idler. The photon properties of the signal and idler are identical in terms of purity and indistinguishability and can be analysed separately. The indistinguishability between different signal (or idler) photons is intrinsically high due to the phase matching relation and energy conservation. Even the indistinguishability across different sources is high due to the engineer-ability of the phase matching, as long as the same laser is used. The single photon purity is an aspect that has a larger interest for the SPDC source since the generation of a single and idler photon has a certain probability per pump pulse. This probability is independent from the number of photons that is already generated, allowing the generation of multiple signal and idler pairs. The output photon state is therefore not a single photon Fock-state but a thermal-state following the Boltzmann distribution as [4] (p. 85))

$$|\psi\rangle = \sum_{n=0}^{\infty} \frac{1}{\bar{n} + 1} \left(\frac{\bar{n}}{\bar{n} + 1} \right)^n |n\rangle_s |n\rangle_i. \quad (2.39)$$

where n is the photon number per pulse and \bar{n} the average photon number per pulse. The single photon purity is analysed using the second order correlation function on either the signal or idler emission. If the source is operated in a pulsed mode with narrow temporal pulses and if the pumping power is in a low squeezing limit (Small generation probability), the second order correlation function on the signal (or idler) photon $g^{(2)}(0)$ can be estimated from the ratio of probabilities [137]

$$g^{(2)}(0) = \frac{\rho_c}{\rho_{s1}\rho_{s2}} = \frac{\frac{C}{F_T}}{\frac{s_1}{F_T} \cdot \frac{s_2}{F_T}} = \frac{F_T \cdot C}{s_1 \cdot s_2}, \quad (2.40)$$

where ρ_c , ρ_{s1} and ρ_{s2} are the probability to measure a single or coincidence with a HBT setup (figure 2.13). These probabilities can be transformed via $\rho_c = C/F_T$,

$\rho_{s1} = s_1/F_T$ and $\rho_{s2} = s_2/F_T$ where C , s_1 and s_2 are the measured coincidence and single rates and F_T the excitation rate (triggers).

Since the approximation only works with small generation probabilities ($\eta_g \ll 1$), we can calculate what $g^{(2)}(0)$ is. First we have to calculate the detection rates on a single detector of the HBT-setup which is

$$\begin{aligned} s_D &= F_{rep} \sum_{n=1}^{\infty} \eta_g^n [1 - (1 - \eta_D)^n] \left(1 - \left(\frac{1}{2}\right)^n\right) \\ &\approx \frac{F_{rep} \eta_g \eta_D}{2} \end{aligned} \quad (2.41)$$

where D is the output arm number, F_{rep} is the repetition rate of the excitation laser and η_D is the optical efficiency of the path. The approximation of ($\eta_g \ll 1$) allows us to only take the term of $n = 1$ in the summation which results in the given approximation. The coincidences can be calculated via

$$\begin{aligned} C &= F_{rep} \sum_{n=1}^{\infty} \sum_{p=0}^n \eta_g^n [1 - (1 - \eta_1)^p] [1 - (1 - \eta_2)^{n-p}] \binom{n}{p} \left(\frac{1}{2}\right)^n \\ &\approx \frac{F_{rep} (\eta_g)^2 \eta_1 \eta_2}{2} \end{aligned} \quad (2.42)$$

with the same parameters as in the singles. When $n = 1$ in the summation, the measured coincidences is zero. The lowest term in the summation that yield a non-zero output is when $n = 2$ and the approximation is therefore the $n = 2$ term in the summation. All higher order term can be neglected because $\eta_g \ll 1$.

The $g^{(2)}(0)$ can now be calculated by using Eq. 2.42 and Eq. 2.41 in Eq. 2.40 knowing that $F_T = F_{rep}$. This yields that the $g^{(2)}(0) = 2$ for an SPDC source, meaning that the photons are bunched.

This appears to be different than a quantum dot source as discussed in Sec. 2.3.2, where the $g^{(2)}(0)$ goes to 0. This difference occurs because the $g^{(2)}(0)$ for a quantum dot is already conditioned on measuring a photon, removing effect from all the zero-photon states induced by losses. The calculated $g^{(2)}(0) = 2$ for an SPDC source is unconditioned and therefore takes all zero-photon states into account. To calculate the single photon purity of an SPDC source allowing it to be compared to a quantum dot source, we have to condition the $g^{(2)}(0) = 2$ on having at least one photon. This can be done by splitting the signal and idler photon and use one of them to measure the $g^{(2)}(0)$ while the other is a herald that a photon pair was generated. This would make the trigger rate F_T equal to the photon detection rate in the herald. The herald rate for the conditional second order correlation function can be calculated from the single and coincidence rates via $F_T = s_1 + s_2 - C_{s_1 s_2}$. Inserting this in Eq. 2.40 results in a conditional

$$g^{(2,1)}(0) = 2\eta_g - \eta_g^2 \quad (2.43)$$

Chapter 2. Theoretical background

implying that the conditional single photon purity can be tuned with the generation rate which is directly linked to the pump power.

To compare the SPDC source to a quantum dot source requires a $g^{(2)}(0)$ that is conditioned on having a signal and idler photon pair. The conditioned single photon purity can be tuned with the generation rate inducing a trade-off between the two. To measure the intrinsic operation of a SPDC source, the unconditioned $g^{(2)}(0)$ should be measured which goes to $g^{(2)}(0) = 2$.

Temporal-to-spatial mode conversion of single photons

Single photon sources are most suitable for creating a quantum network due to the robustness of a photon in carrying information. Applications for single photons are quantum-information processing [61, 143–146], quantum-cryptography [147–149] and quantum-simulation [31, 41, 42]. These applications require a single photon source that deterministically generates indistinguishable photons [43–45]. Single photons have many degrees of freedom allowing encoding in as many different schemes. Two commonly used degrees of freedom are temporal and spatial modes since this is a natural operation of single photon sources. These sources emit in a fixed spatial mode in different temporal modes. Since we are interested in gates operating on different spatial modes, a temporal to spatial mode converter is required. Another solution to obtain identical photons in different spatial modes is to use multiple identical quantum dot sources. However, this is a hard task for quantum dot sources due to inhomogeneous broadening.

This chapter discusses the temporal-to-spatial mode converter (i.e. demultiplexer) for multi-photon generation, based on [59]. Section 3.1 describes the experimental setup including the used source (Sec. 3.1.1) and demultiplexer (Sec. 3.1.2). A theoretical framework to estimate the N-fold coincidence is developed in Sec. 3.2 which takes the setup and source parameters as inputs. The result of this calculation is compared to the measured coincidence rates in Sec. 3.2.2. This chapter concludes with an outlook for potential applications in Sec. 3.3.

3.1 Temporal-to-spatial demultiplexer setup

The principle of a demultiplexer setup is to switch a temporal string of M photons into M distinct spatial modes. This is illustrated in Fig 3.1 (a) with the spatial mode on the x-axis and the temporal mode on the y-axis. Four photons enter the demultiplexing setup and are switched according to their temporal mode. The string of photons entering the demultiplexer are separated by a time $\Delta t = 1/F_{rep}$ with F_{rep} being the repetition rate of the laser exciting the quantum dot. Switching 1 photon in every mode requires switches operating at $F_{sw} = F_{rep}/M$. If the switches in the demultiplexer are limited by a maximum repetition rate of $F_{max} < F_{sw}$, the demultiplexer has to switch more than 1 photon per mode to optimise the efficiency. Maximising this efficiency results in a total of $N \doteq F_{rep}/(F_{max} \cdot M)$ number of photons per mode where \doteq indicates the increase to the nearest integer. This is illustrated in 3.1 (b) where the first N photons are switched to mode 1, the $(N + 1)^{th}$ til the $2N^{th}$ photon are switched to the second mode, and so on. This principle results in a total switching rate of $F_{sw} = F_{rep}/(N \cdot M) \leq F_{max}$ with a total number of photons per burst of $N \cdot M$.

We build a demultiplexer setup for $M = 4$ modes with a source operated at $F_{rep} = 76.152$ MHz. The switches have a maximum operating frequency of $F_{max} = 1.0$ MHz, resulting in an optimum of $N = 20$ photons per mode and an effective switching rate of $F_{sw} = 952$ kHz.

The switches used in the demultiplexer operate based on polarisation by actively switching the polarisation between horizontal and vertical. This rotation can be made using an *Electro Optical Modulator* (EOM). The switches then consist of

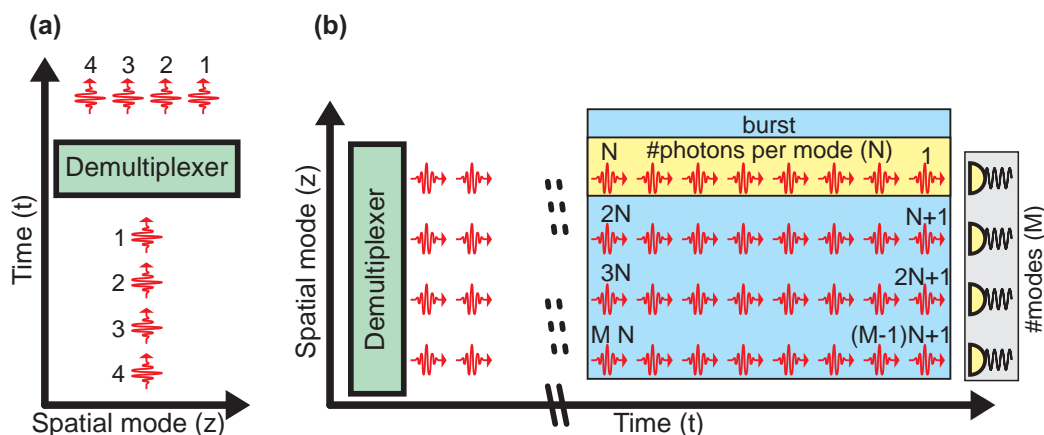


Figure 3.1: Schematic of the temporal to spatial demultiplexer operation with (a) the ideal scenario where every individual photon (Red wiggle) is switched to a different spatial mode and (b) the realistic case where the switching rate is limited multiple photons per mode are switched.

an EOM and a *Polarising Beam Splitter* (PBS), which reflects or transmits light based on the polarisation. Every set of EOM with PBS added to the demultiplexer creates an extra spatial mode, requiring 3 sets to create 4 spatial modes. The temporal matching of photons is done by adding delay fibres after the separation into distinct spatial modes.

The complete scheme for the demultiplexing experiment is shown in Fig. 3.2, and the optical setup for the four demultiplexer is drawn in Fig. B.1 (Appendix B). The three core sections of the demultiplexer setup are highlighted in Fig. 3.2, which are: Source, Demultiplexing & Detection and the Electronics. All three sections will be discussed in detail in the following sections.

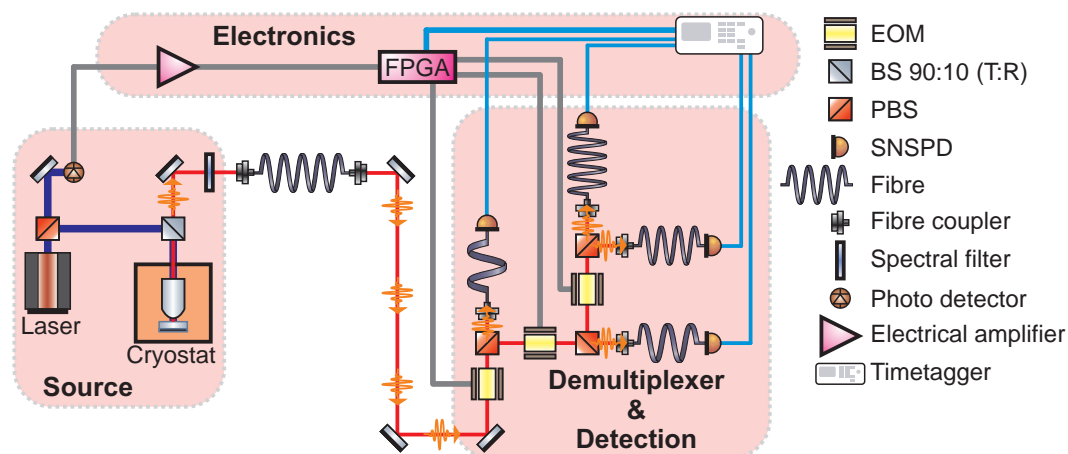


Figure 3.2: Schematic of the demultiplexing experiment with the three core elements: Source, Demultiplexer & Detection and Electronics. The source is a quantum dot excited with a pulsed laser. Photons are collected and transmitted to the demultiplexing setup. The switched photons are detected with *Superconducting Nanowire Single Photon Detectors* (SNSPDs). Detection events are time-tagged together with a trigger signal from the FPGA, synchronised to the laser and EOMs.

3.1.1 Source characterisation

The source used for the demultiplexer experiment is an InAs quantum dot in a GaAs suspended nanobeam waveguide (Fig. 3.3). The waveguide is 320 nm wide, 160 nm thick, 14.7 μm long and terminated on one side with a photonic crystal mirror and on the other side with a shallow-etch grating [132]. The waveguide is designed to confine the emission into a single mode. The photonic crystal mirror ensures that all emission is directed into a single collection grating. The grating coupler is optimised to collect the emitted photons into a single mode optical fi-

bre with a high efficiency. The source has no electrical contacts, resulting that the quantum dot resonance and the quantum dot charge state cannot be tuned. The sample containing the source is mounted in a liquid-helium-bath cryostat and cooled down to 4.2 K.

Characterisation of the source is performed to understand the efficiency and photon characteristics. The total photon rate is important to understand the 4-fold coincidence rate after the demultiplexing setup, which affect the operation time of potential gates after the demultiplexer. The single photon purity is analysed since it affect the fidelity of potential gates afterwards. The indistinguishability is not measured since the source has no electrical gates to control charge noise.

Excitation of the quantum dot is performed with a pulsed aboveband laser with $\lambda = 853$ nm and $F_{rep} = 76.152$ MHz with a pulse width of ≈ 3 ps. The excitation power is actively stabilised using a PID-controller on a predefined selected polarisation. The polarisation can be changed afterwards with waveplates. The PID-controller is connected to a power meter and computer allowing to set the power at a known point in the excitation path. The laser is coupled into the cryostat with a 90 : 10 (transmission:reflection) beamsplitter via the reflection side and focused on the sample with a high-NA objective. The quantum dot is excited from the top and the emitted photons are collected through the waveguide via the grating coupler. The collection fibre is coupled via the transmissive path of the 90 : 10 beamsplitter to minimise photon loss from the splitting of excitation and collection. The collected light is spectrally filtered afterwards with a tuneable bandpass filter ($\Delta\lambda = 0.3$ nm).

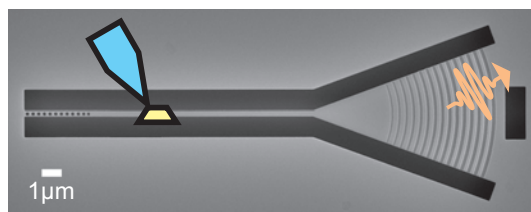


Figure 3.3: Quantum dot single photon source embedded in a suspended nanobeam waveguide. A quantum dot (yellow trapezoid), excitation (blue arrow) and emitted photon (orange wiggly) are schematically indicated.

The first analysis of the source is done on the efficiency and the spectrum, which is shown in Fig. 3.4. The collected spectrum is shown in (a) with both the filtered (green) and the unfiltered (purple) spectrum, measured with an excitation power of 470 nW on the quantum dot. We filter around the emission line with the highest measured count rate, which is at $\lambda = 927.3$ nm. The emission efficiency of the source in the desired wavelength range can be determined from the spectrum by dividing the integrated counts over the total count rate out of the source. This

yield a preparation efficiency of $p_e = (37 \pm 1.5)\%$. Analysis of the collected photons in the desired wavelength range allows the deduction of the bandpass filter efficiency and the saturation behaviour of the quantum dot. This saturation behaviour is plotted in Fig. 3.4 (b) where the collected count rates in the desired wavelength range is plotted as a function of the excitation power. The saturation behaviour of both measurements (with and without filter) are fitted with the logistic function (Eq. 2.34) deduced from the expected saturation behaviour (red dot-dashed line) and with Eq. 3.1 (solid black line)

$$I_{QD}(P) = I_0 \left(1 - e^{-\frac{P}{P_{\text{sat}}}} \right), \quad (3.1)$$

where I_0 is the maximum collected light and P_{sat} is the saturation power.

The data with and without filter are fitted with the same parameters, where the fit adds filter efficiency (η_F) for the filtered data. Both equations (logistic Eq. 2.34 and exponential Eq. 3.1) result in the same filter efficiency $\eta_F = (58 \pm 2)\%$, but the saturation count rate and intermediate behaviour of the two is different. Figure 3.4 (b) indicates that the logistic function (Eq. 2.34) does not follow the saturation behaviour of the quantum dot, while it was expected from calculation. Equation 3.1 was determined empirical for the saturation curve as this was the equation with the least number of free parameters that followed the behaviour of the saturation. An explanation of why Eq. 2.34 does not fit comes from the type of excitation. The quantum dot is excited via aboveband excitation which

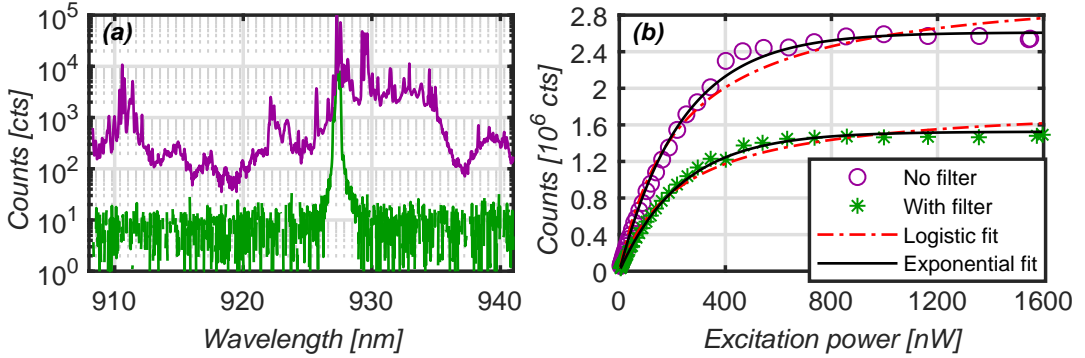


Figure 3.4: Results from the spectral (a) and the saturation (b) measurement. (a) shows the spectrum before filtering (purple) and after filtering (green) indicating a strong suppression of other excitation lines. The count rate in the desired wavelength is reduced by the efficiency of the filter. (b) shows the saturation measurement for the case with (green) and without (purple) filter. There are two different fits with each three parameters (I_0 , η_F and P_{sat}), where one curve follows an exponential curve (black solid) and the other line the logistic function from Eq. 2.34 (red dot-dashed line).

has multiple decay paths as can be seen by the number of emission lines in Fig. 3.4 (a). The decay rates of all the other states are unknown thus we cannot setup a rate equation model to analyse the expected saturation behaviour. Since the complexity from all other states can alter the saturation behaviour, we have to use a simplified empirical model. This resulted in an exponential saturation behaviour as described in Eq. 3.1. Along with the filter efficiency, the fit yields the saturation power of the quantum dot, $P_{sat} = 236$ nW and the saturation counts $I_0 = 2.6 \cdot 10^6$ photons per seconds.

We analyse the single photon purity via the second order correlation function (Sec. 2.3.2). The generated photons are inserted in a HBT-setup (Fig. 2.13) and the photons are time-tagged with a resolution of 4 ps. The quantum dot is excited at approximately the saturation power ($P = 231$ nW) yielding the second order correlation shown in Fig. 3.5. The photons are time binned together at time intervals larger than 4-ps the analysis to obtain coincidences between the two paths at different time intervals. The time binning has to be chosen carefully to avoid aliasing between the time binning and the repetition rate. The binning is therefore done at the repetition rate divided by an integer number, Fig. 3.5 (a) $t_{bin} = 1/F_{rep} \approx 13.1$ ns and Fig. 3.5 (b) $t_{bin} = 1/(10 F_{rep}) \approx 1.31$ ns. Since Fig. 3.5 (a) is binned at the repetition rate of the laser, the individual excitation pulses are not visible. Investigating the $g^{(2)}(0)$, it is visible that the correlation function is reduced meaning that there are less correlations between the two arms. This shows that the source emits a single photon per excitation pulse. Since the second

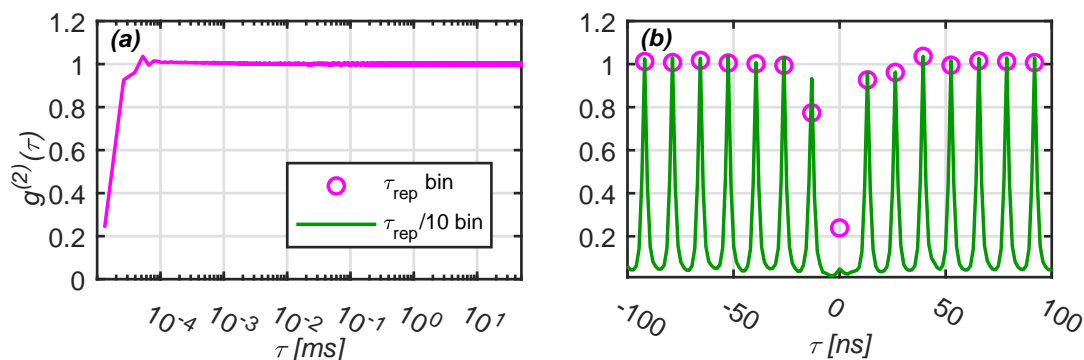


Figure 3.5: Measured second order correlation function with (a) the long time scale and (b) the short time scale. The magenta data are processed with a binning equal to the repetition time of the laser, where the green data are binned at 10% of the repetition time of the laser. These integer divisions reduces aliasing between the binning and the laser repetition. (a) Indicates that there is no slow blinking of the quantum dot at a time scale of $\tau < 50$ ms. (b) Shows $g^{(2)}(0) = 0.05 \pm 0.01$ on the data with $t_{bin} \approx 1.31$ ns. The asymmetry in the data is expected to come from correlation noise between the detectors.

order correlation function in Fig. 3.5 (a) is 1 at the visible timescale range, it can be concluded that there is no blinking up to a timescale of $\tau_{\text{blinking}} > 50$ ms [150]. If there was blinking in this time range, it would result in a $g^{(2)}(\tau) > 1$ when $\tau < \tau_{\text{blinking}}$. A better analysis of the $g^{(2)}(0)$ comes from the analysis at $t_{\text{bin}} \approx 1.31$ ns, which is shown in Fig. 3.5 (b) (green line). This resolves the individual excitation pulses and is normalised to the average peak height at a long time distance (10 to 50 ms). The central peak is nearly diminished and yields a $g^{(2)}(0) = 0.05 \pm 0.01$. The circles in this plot are the datapoints for the analysis of $t_{\text{bin}} \approx 13.1$ ns, showing that the peak heights match when $\tau \neq 0$ and that the peak height is reduced at $\tau = 0$. The reduction in $g^{(2)}(0)$ due to the decreased bin width is induced by an offset of $\tau = 0$ in the binning process. The time-bin of $\tau = 0$ is therefore not centralised around zero, but at a small time offset. When the timestamps are binned at the repetition rate ($t_{\text{bin}} \approx 13.1$ ns) and the central bin is not perfectly centred around $\tau = 0$, the analysed $g^{(2)}(0)$ will be artificially increased. The asymmetry in both datasets in Fig. 3.5 (b) is assumed to occur from correlation noise of the detectors, but is expected to have no significant effect on $g^{(2)}(0)$.

To know the photon emission rate of the quantum dot, we have to analyse the bright state efficiency (η_b) of the quantum dot. Assuming that the decay from the aboveband to an exciton line and the decay to the bright/dark X_0 dipole is uncorrelated, the effective dark state can be individually modelled accordingly to [151]. The strong excitation power creates many electron-hole pairs, which increases the probability that out X_0 is reached via a bi-exciton decay. The decay rate from a bi-exciton to a bright/dark exciton is twice the decay rate from a bright/dark exciton to the ground state. This results in a bright state efficiency of $\eta_b = (40 \pm 4)\%$ (See App. A for calculation). The quantum dot emission rate is then $F_{\text{rep}} p_e \eta_b = 11.4$ MHz when excited with a laser at $F_{\text{rep}} = 76.152$ MHz. Knowing the emission rate, the collection efficiency of the waveguide (β -factor [52]) has to be analysed to know the photon rate into the waveguide. This is the ratio of the photon emission rate into the collection mode divided by the total photon emission rate from the quantum dot. This could not be measured for this specific quantum dot, but it could be estimated from simulation and other measurements [102, 152] yielding

Exciton line p_e	$37 \pm 1.5\%$
Bright state efficiency η_b	$40 \pm 4\%$
Waveguide β	$80 \pm 10\%$
Outcoupler efficiency η_{OC}	$60 \pm 5\%$
Collection optics T	$69 \pm 2\%$
Spectral filter η_F	$58 \pm 2\%$

Table 3.1: Summary of efficiencies required to calculate the total source efficiency.

$\beta = (80 \pm 10)\%$. The last items to analyse for the total source efficiency are the outcoupling from the waveguide through the collection optics. This can be divided in the mode matching between the outcoupler and collection fibre and the transmission efficiency of the optical components. The mode matching is measured in [132] as $\eta_{oc} = (60 \pm 5)\%$. Their sample was fabricated from the same wafer as our sample, allowing us to assume the same efficiency. The transmission efficiency of the collection optics is measured as $T = (69 \pm 2)\%$. All the efficiencies required to calculate the source efficiency are summarised in Tab. 3.1, and yield a source efficiency of $\eta_S = p_e \eta_b \beta \eta_{oc} T \eta_F = (2.84 \pm 0.54)\%$.

The source efficiency can be compared to the results of the power series, where we had an efficiency of $\eta = \eta_F I_0 / F_{rep} = 1.98\%$. This is lower than the source efficiency since η includes the transport and detection efficiency. The coupling to the detector was done via the demultiplexer setup due to spatial limitations. All switches were turned off resulting in all the photons travelling through the same path. to obtain the total detection rate, the source efficiency has to be multiplied with the fibre efficiency ($\eta_{\text{fibre}} = (92 \pm 2)\%$), demultiplexer transmittance ($\eta_{m,sw} = (84 \pm 2)\%$), and detector efficiency ($\eta_{\text{det}} = (88 \pm 1)\%$). Multiplying these three efficiencies with the source efficiency yield $\eta = (1.9 \pm 0.4)\%$ meaning that the calculated and measured count rates are within each-other error margin. The efficiency of these three elements are discussed later on, but shows that we understand the losses in the setup.

3.1.2 Operation of the demultiplexer

The demultiplexer transmission used in Sec. 3.1.1 is when we turn off all switches. Due to the different paths, every mode has a different transmission, which are $\eta_1 = 84\%$, $\eta_2 = 84\%$, $\eta_3 = 86\%$ and $\eta_4 = 88\%$. Beside the spatial losses, there is a loss incorporated from the switching, which is given by the extinction ratio of the switching (1 : 100) and the losses of the EOM and PBS (98.4%), resulting in an effective switching efficiency of $\eta_{sw} = (97 \pm 1)\%$. The fibre efficiency from Sec. 3.1.1 is the fibre transporting the photons from the source to the demultiplexer. This fibre is 30 meter long due to the physical distance and has a measured efficiency of $\eta_{\text{fibre}} = (92 \pm 2)\%$. The detector efficiency consists of the transmission from the fibre between the demultiplexer and detector, and the detection efficiency of the detector. This fibre has a transport efficiency of $\approx 94\%$ and the detectors are specified to have an efficiency of $> 95\%$. The connection between the fibre and the detector is made with a splice with an estimated efficiency of $\approx 98\%$ resulting in a total detection efficiency $\eta_{\text{det}} = (88 \pm 1)\%$.

The last aspect of the demultiplexer to discuss is the control of the EOMs and the time-tagging. The EOMs used are *Eksma Optics Ultrafast Pulse Pickers* made from 5 mm wide KTP-crystal. They are operated as half wave plates by applying a voltage of 2.0 \sim 2.5 kV across the crystals. The voltage is applied in pulses at a

maximum repetition rate of 1 MHz (952 kHz in the experiment) with a duty cycle of 27.5%. The duty cycle is slightly more than 25% since this also accommodates the rise and fall time of 6.6 ns.

The triggering of the EOMs is controlled using a *Field Programmable Gate Array* (FPGA). An FPGA consists of many logic gates where interconnections can be programmed, allowing fast operation of reconfigurable functions. One of the logic blocks on the FPGA is a *Phase Locked Loop* (PLL), which is referenced to the trigger signal from the pulsed excitation laser. The trigger signal from the laser is connected via a 30 meter long BNC cable to the FPGA. The FPGA has four outputs with a frequency divided by the PLL of $F_{\text{out}} = F_{\text{in}} / (M \cdot N)$. This frequency matches the operation frequency of the demultiplexer. All four outputs consist of a TTL pulse where every consecutive channel is 90 degree out of phase with the previous one ($\phi_m = 90^\circ \cdot (m - 1)$). The first pulse is sent to the time tagger to record the timestamp of when the switching sequence starts, and the other three are sent to the three different EOMs to trigger their switching.

3.2 Expectation of four fold detection rates

Having information of all the efficiencies, a prediction of the coincidence rates can be made. Measuring a coincidence means that all modes should contain a photon that is detected. ρ_m^n is the detection probability of a photon in temporal mode n and spatial mode m . The probability to measure a four fold coincidence at temporal mode n is $\eta_{4F}^{(n)} = \rho_1^{(n)} \rho_2^{(n)} \rho_3^{(n)} \rho_4^{(n)}$. This is simplified to $\eta_{4F}^{(n)} = (\rho^{(n)})^4$ if all spatial modes have the same detection probability and $\eta_{4F} = (\rho)^4$ if there is no temporal structure in detection probability.

3.2.1 General expectation for M-fold demultiplexer

The demultiplexer used in this setup has both temporal and spatial structure in the detection probability. The spatial dependency results from losses in the different modes, and the temporal structure results from the deadtime of the detectors. The deadtime is longer than the time between two consecutive photons but shorter than the time between consecutive bursts of photons, resulting in a full reset of detection probabilities between these bursts. This simplifies the calculation as we can treat a single burst independently.

The probability to detect a photon can be split up in the different dependencies by $\rho_m^n = \eta_m \eta_n \eta_i$ with η_m and η_n as the spatial and temporal dependencies, and η_i is the intrinsic efficiency. Every photon has a lifetime (τ_t), but this is significantly smaller than the interval between photons (Δt) and the detector deadtime (τ_{dead}). Every photon is therefore considered as a δ -function in time giving a discrete string for $\eta_n(n)$ and ρ_m^n . The time response in the detection probability is

assumed to be purely affected by the deadtime of the single photon detector with a certain recovery profile for the efficiency. Two common detectors are *Avalanche Photodiode* (APD) and a *Superconducting Nanowire Single Photon Detector* (SNSPD) which have typical recovery profiles of a heavy-side function and exponential function, respectively. The maximum efficiency of η_n is assumed to be 100% since static losses are written in the intrinsic efficiency (η_i). Therefore we can see η_n as the time response function of the detector with the current photon number (n) and the photon number of the last detection event (Q) as input variables. This allows η_n to be written as a time response function of $\eta_n = T_m^{P,Q}$ with P as the current photon number ($P = n$). The time response function T is dependent on the spatial mode number m since different detectors can have different deadtimes. If $Q = 0$, there has not yet been a detection event in the photon burst so $T_m^{P,Q=0} = 1$.

Having all the required element to calculate ρ_m^n we can calculate this for different values of n . The first scenario is when $n = 1$ where the detection probability is

$$\rho_m^{n=1} = \eta_{i,m} T_m^{1,0}, \quad (3.2)$$

with $\eta_{i,m} = \eta_i \eta_m$.

When $n = 1$, the last time-bin where a detection event could have happened is $Q = 0$, meaning it is far before the photon arrives. The detection efficiency is then the intrinsic efficiency multiplied with the spatial mode efficiency. Extending this to $n > 1$ requires summing over all probability to obtain a detection event multiplied with the probabilities of when the last detection event happened. The probability of a specific last detection event is the probability of detecting a photon at that specific time while not detecting a photon at any earlier time, and can be written as

$$\prod_{\epsilon=Q}^{n-1} (1 - \rho_m^\epsilon) \rho_m^{Q-1}$$

with Q as the last occurred detection event. This allows us to write out the detection probability for $n = 2$ and $n = 3$ resulting in

$$\begin{aligned} \rho_m^{n=2} &= (1 - \rho_m^1) \eta_{i,m} T_m^{2,0} + \rho_m^1 \eta_{i,m} T_m^{2,1}; \\ \rho_m^{n=3} &= (1 - \rho_m^1) (1 - \rho_m^2) \eta_{i,m} T_m^{3,0} + \rho_m^1 (1 - \rho_m^2) \eta_{i,m} T_m^{3,1} + \rho_m^2 \eta_{i,m} T_m^{3,2}. \end{aligned}$$

This shows that the probability for a detection event for a specific Q can be written as

$$\eta_{i,m} \prod_{\epsilon=Q+1}^{n-1} (1 - \rho_m^\epsilon) \rho_m^Q T_m^{n,Q}$$

since we look for a detection at time n with a last occurred detection at time Q . To obtain the total probability for a detection event, we have to sum over all prob-

abilities of the last detection event, resulting in [†]

$$\rho_m^n = \eta_{i,m} \sum_{k=0}^{n-1} \left(\prod_{\epsilon=k+1}^{n-1} (1 - \rho_m^\epsilon) \rho_m^k T_m^{n,k} \right). \quad (3.3)$$

Writing out for $n = 1$ to $n = 4$ yields

$$\begin{aligned} \rho_m^{n=1} &= \eta_{i,m} \rho_m^0 T_m^{1,0} \\ \rho_m^{n=2} &= \eta_{i,m} [(1 - \rho_m^1) \rho_m^0 T_m^{2,0} + \rho_m^1 T_m^{2,1}] \\ \rho_m^{n=3} &= \eta_{i,m} [(1 - \rho_m^1) (1 - \rho_m^2) \rho_m^0 T_m^{3,0} + (1 - \rho_m^2) \rho_m^1 T_m^{3,1} + \rho_m^2 T_m^{3,2}] \\ \rho_m^{n=4} &= \eta_{i,m} [(1 - \rho_m^1) (1 - \rho_m^2) (1 - \rho_m^3) \rho_m^0 T_m^{4,0} + \\ &\quad (1 - \rho_m^2) (1 - \rho_m^3) \rho_m^1 T_m^{4,1} + (1 - \rho_m^3) \rho_m^2 T_m^{4,2} + \rho_m^3 T_m^{4,3}], \end{aligned} \quad (3.4)$$

and shows that there is a ρ_m^0 which can be interpreted as the time response value at the beginning of a burst. Typically this is considered to be $\rho_m^0 = 1$ since the time between two bursts is larger than the deadtime, but this can be put lower if there would be a physical reason that the detector is not at the maximum efficiency at the beginning of a burst.

The next step to calculate the expected count rate is to define a function for the time response function. The detectors used in the experiment have an exponential recovery where the dead time is determined by the time the detector needs to reach back 95% of the original efficiency. The time response function can then be written as

$$\begin{aligned} T_m^{P,Q} &= 1 && \longrightarrow Q = 0 \\ T_m^{P,Q} &= 1 - e^{-\frac{P-Q}{\tau_{\text{norm}}}} && \longrightarrow Q \neq 0 \end{aligned} \quad (3.5)$$

where τ_{norm} is the normalised dead time and can be written as

$$\tau_{\text{norm}} = \frac{\tau_{\text{dead}} F_{\text{rep}}}{-\ln(0.05)}. \quad (3.6)$$

The expected number of M-fold coincidences can be calculated by multiplying the detection probabilities of all spatial modes at a fixed time with each other, and sum this over all time-bins. The expected number of coincidences within a single burst is then

$$C_{MF} = \sum_{n=1}^N \prod_{m=1}^M \rho_m^n. \quad (3.7)$$

Since the rate of bursts can be written by $F_b = \frac{F_{\text{rep}}}{M \cdot N}$, the total M-fold coincidence rate is given by

$$F_{MF} = \frac{F_{\text{rep}}}{M \cdot N} \sum_{n=1}^N \prod_{m=1}^M \rho_m^n. \quad (3.8)$$

[†] $\prod_{\epsilon}^{<\epsilon} = 1$

The given equations allows us to predict the measured four-fold coincidence rate out of the demultiplexer setup. The efficiencies used for the calculation are given in Sec. 3.1.1 and Sec. 3.1.2 and implemented as $\eta_{i,m} = \eta_S \eta_{\text{fibre}} \eta_m \eta_{\text{sw}} \eta_{\text{det}}$. The deadtime is assumed to be equal for every detector and $\tau_{\text{dead}} = 70$ ns. This results in a 4-fold coincidence rate of $F_{4F} = 2.5 \pm 1.9$ Hz.

3.2.2 Results from demultiplexing experiment

An input source rate $F_{\text{in}} = F_{\text{rep}} \eta_S \eta_{\text{fibre}}$ is defined to analyse the performance of the demultiplexer independent from the source. The input source rate can be modified by changing the efficiency of the source or by changing the excitation power as can be seen from the saturation behaviour (Fig. 3.4 (b)).

The four fold coincidence rate is measured for different input source rates ranging from 400 kHz to 1.7 MHz. The measurements with an input source rate below 800 kHz are performed with a non-optimised collection efficiency (T in Tab. 3.1) where the variation occurs due to different steps in optimising the source rate. The measurements with a source rate of more than 800 kHz are performed with the optimised efficiencies as in Tab. 3.1 but with different excitation powers. The results are shown in figure 3.6 where the four-fold coincidences depending on the input source rate is shown. The circles indicate the measured coincidence rate and the solid line indicates the expected coincidence rate from the calculation without any fitting parameter. The measured coincidence rate ranges from 4.3 ± 0.2 mHz

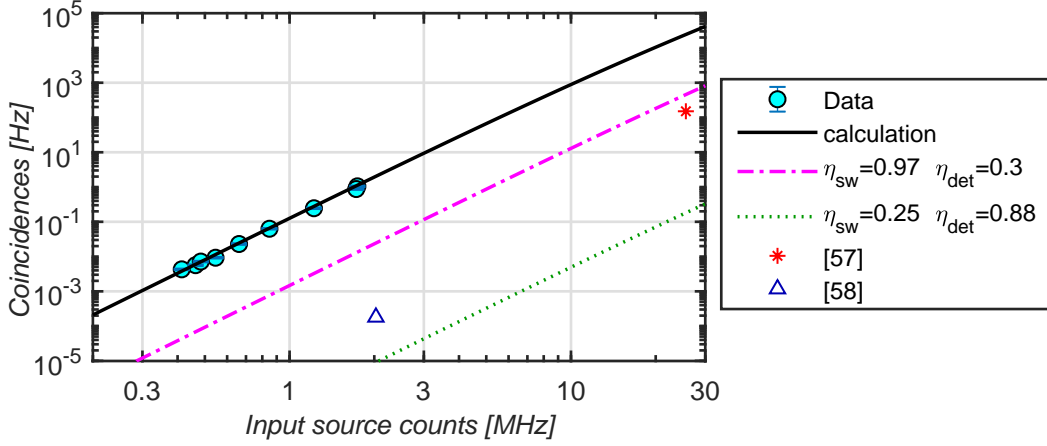


Figure 3.6: Calculated (Black solid line) and measured (Blue dots) four fold coincidence rates depending on the input source rate. Calculations are compared to a passive demultiplexer ($\eta_{\text{sw}} = 1/M = 0.25$, green dotted line) or when we measured with APDs ($\eta_{\text{det}} = 30\%$, magenta dash-dotted line). Results from [57] and [58] are compared to the calculation with APDs since their results are measured with APDs.

(15 per hour) with 0.41 MHz input source rate to 1.05 ± 0.05 Hz with 1.7 MHz input source rate. The calculated four fold coincidence rates for these input source rates are respectively 3.8 mHz and 1.12 Hz. This shows that the expected and measured coincidence rates matches closely, taking into account that the calculation does not contain any fitting parameter.

To compare our results to the results from other configurations and research groups, we also calculated the expected four fold coincidence rates with different parameters. The first comparison is made to a fully passive demultiplexer, assuming the same source and detectors as in our measurement. This would result in a switching efficiency of $\eta_{sw} = 1/M = 0.25$ and is plotted in Fig. 3.6 as the dotted line. This indicate that our active demultiplexing setup has an improvement of 5 orders of magnitude in four fold coincidence rate. The second comparison is if we had measured with APDs instead of SNSPDs as done in [57, 58]. This allows us to compare our coincidence rates to theirs and can be calculated by using $\eta_{det} = 0.3$. This calculation is shown in Fig. 3.6 as the dash-dotted line. Reference [57] and [58] are shown in Fig. 3.6 as a red star and blue triangle, respectively. Reference [57] has an input source rate of 25.6 MHz with a detected four fold coincidence rate of 151 Hz. This includes a high efficient circuit ($\eta_c > 95\%$), and correcting for this results in a four fold rate of $F_{4F} < 200$ Hz. Our demultiplexer would yield a four fold coincidence rate of $F_{4f} \approx 460$ Hz using the same type of detectors as [57], indicating that our demultiplexer is more efficient. Using SNSPDs with a input source rate of 25.6 MHz would yield a four fold coincidence rate of $F_{4f} \approx 38$ kHz. Reference [58] uses a different technique of switching by fabricating the demultiplexer on-chip. They predict a four fold coincidence rate of $F_{4f} = 0.18$ mHz with a source rate of 2 MHz. Their coincidence rate is low since the on-chip $\eta_m < 0.1$, which severely limits the demultiplexer.

3.2.3 Expansion of demultiplexer setup

The current demultiplexing setup convert the temporal modes to four spatial modes. The design of the demultiplexer allows for a trivial expansion to more spatial modes. This can be done by placing an electrical resonant EOM before the first electrical broadband EOM and drive it with an oscillate at $F_{Rep}/2$. This switches consecutive photons between horizontal and vertical polarisation. Delaying every first photon with one time bin and route it back parallel to the original spatial mode creates a second spatial mode temporal multiplexed with the second photon. Both photons are then switched into the chain of broadband EOMs. A drawing of the expansion to an 8-fold demultiplexer is drawn in Fig. B.2 (Appendix B). This second spatial mode travels parallel to the first spatial mode through the broadband EOMs, resulting that every broadband EOM creates two extra modes.

Another method to expand the number of spatial modes is be chaining more broadband EOMs, creating an extra mode per EOM. This can still be coupled with the

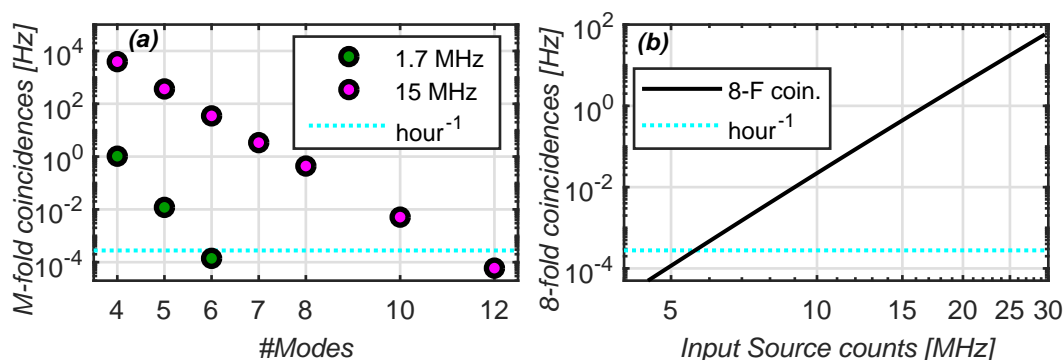


Figure 3.7: Predictions of coincidence rates for different expansions of the demultiplexer. **(a)** Expected M -fold coincidence rate with an increase of the number of spatial modes. The green dots shows the expectations for the source used in this experiment and the magenta dots shows the expectations if we obtain an input source count rate of 15 MHz. **(b)** Expected 8-fold coincidence rate depending in the input source count rate, assuming the expansion a resonant EOM.

resonant EOM, creating two extra modes per broadband EOM. With the given calculations and measured efficiencies, we can predict the M -fold coincidence rate for different expansions. We assume to have no resonant EOM if $M \leq 7$, and we have a resonant EOM if $M \geq 8$ where M can only take even integer values. We assume that the efficiency of a spatial mode reduces with 2% for every EOM in the path. The expected M -fold coincidences are shown in Fig. 3.7 (a) where the green dots are the expectation with our current source and the magenta dots the expectation if we increase the input source count to 15 MHz. The blue dotted line indicate a coincidence rate of 1 per hour. This shows that the current source can scale up to a 6-photon demultiplexer with a coincidence rate of a few per day. When the source is improved to yield 15 MHz of input counts we can scale realistically to a 10 photon demultiplexer.

The original design of the demultiplexer was to obtain 8 spatial modes, so we analyse the required input source counts to yield reasonable coincidence rates. Figure 3.7 (b) shows the expected coincidence rate for an 8-fold demultiplexer depending on the input source counts, where the blue line indicate a count rate of 1 per hour. This shows that an input source count of 5 MHz is required to obtain a few 8-fold coincidences per day. To increase this coincidence rate to at least 1 Hz would require an input source count rate of almost 17 MHz.

3.3 Conclusion and outlook

This chapter demonstrates a highly efficient demultiplexer setup for multi-photon generation which can exploit the quantum advantage for quantum information processing and simulation [146, 153, 154]. The used source consists of a quantum dot in a planar structure with a grating coupler for top-collection of light. We measured a $g^{(2)}(0) = 0.05 \pm 0.01$ at $P = P_{sat}$ and a maximum count rate out of the source of $I_0 = 2.6$ MHz.

We built demultiplexer that switches the photons over 4 spatial modes. We made a fit parameter free model to predict the measured M -fold coincidence rate, which can be used for a demultiplexer switching into M number of spatial modes. We measured the efficiencies of our demultiplexer and used the model to predict the measured 4-fold coincidences depending on the input count rate from the source. We performed the measurement and varied the input count rate by adding/removing loss elements in the single photon source and obtained an input count rate ranging from 400 kHz up to 1.7 MHz. The largest measured coincidence rate is $F_{4F}1.05 \pm 0.05$ Hz, and all measured coincidence rates fits with the model. Comparing our demultiplexer with other built demultiplexers shows that we have a higher efficiency, since we can obtain more than twice the coincidence rate of others.

Future work exist of expanding the demultiplexer to a higher number of spatial modes. The design of the current setup was based on a trivial expansion to a larger number of modes. We focused on doubling the number of modes with one extra EOM, resulting in an 8-fold demultiplexed source. We showed that we need an input source count of at least 5 MHz to have a few 8-fold coincidences per day, and need an input source count of 17 MHz to obtain at least 1 Hz of 8-fold coincidences. A direction to increase the source efficiency is to use electrical gated samples and perform resonant excitation [55, 57].

A general future direction for demultiplexed single photon sources would require demultiplexing on chip [58]. Recent work demonstrated on chip switches [155], which can route towards fully integrated devices for multi photon experiments.

Characterisation of Single Photon Sources

Single photon sources can be constructed in different manners with most commonly the quantum dot (QD) and spontaneous parametric down conversion (SPDC) sources. Both sources generate photons with distinct characteristics depending on the configuration of the source. This chapter focuses on characterising specific aspects of these sources. First we discuss a quantum dot single photon sources (Sec. 4.1) embedded in two different nanostructures fabricated in a sample with a diode structure. The first structure consists of a nanobeam waveguide and the second of a photonic crystal waveguide. In the nanobeam waveguide we investigate the effect of the waveguide width on the spectral and electrical properties of the quantum dot. As seen in Sec. 2.2.1 are the lifetime and spectral width related to each other. We measure the spectral properties and the electrical properties and link that to possible noise sources. The second part of the quantum dots investigates a quantum dot embedded in a photonic crystal waveguide. Section 2.2.1 shows that the decay rate of a quantum dot can be altered by changing the density of states. This can be done with a photonic crystal waveguide, where the quantum dot resonance is close to the photonic bandedge. When the quantum dot is tuned onto the bandedge, the lifetime should decrease and the spectral width should increase.

Section 4.2 describes an SPDC source, which was set up during an external project in the *Clarendon Laboratory, department of physics* at the *University of Oxford*.

This describes the process of setting up an SPDC and characterising the source. The characterisation showed unexpected behaviour which is investigated. The focus of this section is on what type of noise sources could have influenced the measurements and how these can be solved. The last part of this chapter (Sec. 4.3) compares quantum dot sources and SPDC sources with each other in terms of operation for applications. Both sources have distinct characteristics which can be beneficial for different applications, which requires the knowledge on how they compare to each other.

4.1 Characterisation of quantum dots

This section describes the characterisation of quantum dots embedded in planar photonic nanostructures. First we study the effect of the width of a nanobeam waveguide (Sec. 2.2.2) on the spectral and electrical properties of a quantum dot. The effect of the width is studied for two type of excitons, the neutral exciton (X_0) and the negatively charged exciton (X^-). The waveguides are fabricated in a sample with a *P-I-N-I-N*-diode that allows electrical control of the resonance frequencies.

After the nanobeam waveguide we discuss the measurements on photonic crystal waveguides fabricated in a sample with a *P-I-N*-diode. We investigate the effect of the coupling of the quantum dot to the photonic crystal waveguide while the quantum dot resonance is tuned into the bandgap. When the resonance shifts into the bandedge the number of decay channels increases, which decreases the lifetime and increases the linewidth of the resonance.

4.1.1 Characterisation of quantum dots in waveguides

The fabrication of nanostructures around quantum dots influence the spectral properties of the excitons as discussed in Sec. 2.2.2. Changing the design parameters of a structure changes the spectral properties since the modes in the waveguide change. There are many design parameters that can be investigated, but we focus on the width of a nanobeam waveguide since this should have a direct link to the coupling between the exciton and the guided modes of the waveguide. The quantum dots are grown via the Stranski-Krastanov method [76] resulting in spatial and spectral randomly distributed quantum dots. The waveguides are fabricated at fixed locations on the sample resulting in a random number of quantum dots per waveguide, at random lateral (perpendicular to waveguide direction) and longitudinal (parallel to waveguide direction) positions.

This random distribution of quantum dots adds extra measurement steps before the spectral properties can be measured, which are to find the longitudinal position and spectral resonances. This is done by using a CW laser at ~ 860 nm that excited quantum dot in the wetting layer, enabling emission from the resonances.

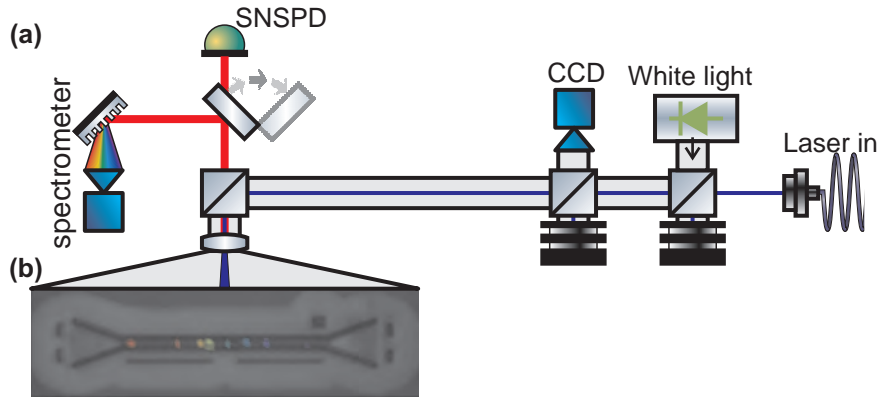


Figure 4.1: **(a)** Schematic of the setup used for the characterisation of the quantum dot emitters. Light is coupled in via a fibre and reflected on a beamsplitter towards the sample. Extracted photons are transmitted through the beamsplitter and measured by either a spectrometer or an SNSPD. The input path contains two extra beamsplitters allowing white-light illumination via an LED and allows us to view the sample with a CCD-camera. **(b)** Grey scale image of a nanobeam waveguide with a designed width of 500 nm while illuminated via white light. The colours are images of the quantum dots via aboveband excitation indicating the spatial position of the quantum dots. The colours differentiate the quantum dots and do not represent the emission wavelength.

The focus of this laser is scanned along the longitudinal direction and the collected emission is sent via the waveguide to a spectrometer and the top emission is collected by a CCD camera. The spectrometer identifies the resonance wavelength and the CCD camera the position in the waveguide.

The setup performing the measurements is schematically shown in Fig. 4.1 (a). The input laser is inserted via a fibre, transmitted through two beamsplitters and then reflected by a beamsplitter towards the sample. The two other beamsplitters are used to insert a white light source onto the sample and to image the sample on a CCD. Light out from the sample is transmitted on the top beamsplitter and is sent to either a spectrometer or an SNSPD (superconducting nanowire single photon detector), depending on the type of measurement. The sample used in the nanobeam measurements is shown in Fig. 4.1 (b) which shows one of the nanobeam waveguides that is measured on, illuminated via white light. The white light image is overlaid with images captured by the CCD of the excitation of different quantum dots, where every colour represents a different quantum dot. The waveguide shown is a waveguide of 500 nm wide and labelled as 2Aw05QD3. The measurement process is described by following a quantum dot numbered as QD3 located in this waveguide.

Voltage tuning

When the spatial location of a quantum dot is found we can measure the coarse spectral properties of the quantum dot. This is measured by exciting the quantum dot with the same CW laser (~ 860 nm, wetting layer) while we measure the emitted light on a spectrometer. This is done at different applied bias potentials from which an emission map is obtained showing the emission depending on the potential and emission wavelength. An example of these maps is shown in Fig. 4.2 which is measured on a QD3 in the 500 nm wide waveguide (2Aw05QD3). Darker areas shows emission from the quantum dot, which is normalised to the maximum measured value. The emission map shows different emission lines which are identified as different charge state of the quantum dot based on [69]. The identified lines are the X^+ (939.7 nm), X_0 (939.9 nm), X^- (943.4 nm) and X^{2-} hybridised with the wetting layer (944.1 nm). There are more emission lines visible which are other states of the exciton, but they have a significant lower probability to be populated. The exact wavelength of all these states do vary from quantum dot to quantum dot [50, 76, 156–158], but the relative distances between the exciton lines are as expected for this type of sample [69]. The effect that different charge states occur at different applied voltages is due to the shift in the bandedge [69, 158–160], allowing the capture of a different number of charges in the quantum dot.

Knowing the coarse spectral properties of the quantum dot, resonance transmis-

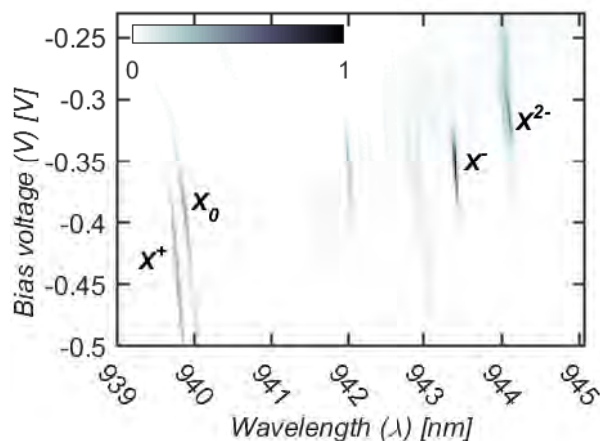


Figure 4.2: Photoluminescence map showing normalised emission intensity depending on the applied voltage and emission wavelength. The quantum dot is excited with a laser emitting at ~ 860 nm and the collected light is measured on a spectrometer. This dot shows typical features for a quantum dot in a P - I - N - I - N structure with an X_0 around 939.9 nm, X^- around 943.4 nm, an expected X^+ at 939.7 nm and an expected X^{2-} hybridising with the wetting layer around 944.1 nm.

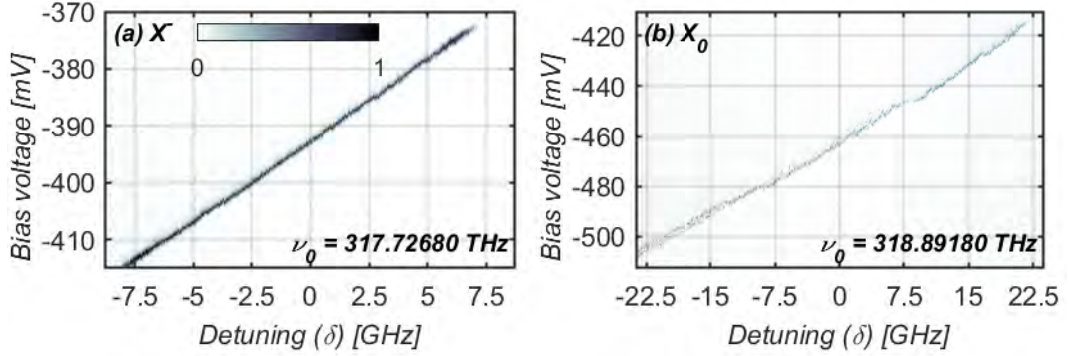


Figure 4.3: Voltage-frequency map of (a) X^- and (b) X_0 showing the normalised transmission reduction depending on the laser frequency detuning from ν_0 and applied bias voltage. Step sizes are 200 μV and 40 MHz.

sion (Sec. 2.2.3) is used to measure the spectral properties with a higher resolution. This finer resolution cannot be measured with the 860 nm laser and spectrometer due to the limited resolution of the spectrometer (~ 25 pm; 8.3 to 9.3 GHz). Another effect is that the 860 nm laser alter the resonance wavelength of the quantum dot due to charges induced in the environment around the quantum dot. The measurement with the 860 nm laser is however an accurate enough indication of the wavelength and voltage of the resonance. The first RT-measurement is to measure the charge plateau of the exciton, which is a trace of the resonance frequency with a varying bias voltage. This plateau is measured with an attenuated tunable CW-laser coupled into the waveguide via one of the grating couplers. The other grating couples the light into a fibre towards a single photon detector. The transmitted photons are counted, and should reduce when the quantum dot and laser are on resonance since it is a RT-measurement. The frequency and voltage are scanned across a region where we expect the resonance to appear based on the measurements with the 860 nm laser. The frequency is stepped in 40 MHz and the voltage with 200 μV . The measured count rate is normalised according to Eq. 2.16 and we plot the depth of the normalised transmission ($1 - T_{norm}$) in Fig. 4.3. We did this for two exciton lines, the X^- (Fig. 4.3 (a)) and the X_0 (Fig. 4.3 (b)). Both excitons show a tuning over tens of millivolt with a range of tens of gigahertz. The transmission dip appears to be less prominent for the X_0 , which will be discussed later on.

Measuring Linewidths

Measuring the charge plateau of the exciton allows us to identify the centre of it. This is where the resonance interaction is the strongest, resulting in the deepest RT-dip. Around this point is a more fine scan performed at the voltage where the

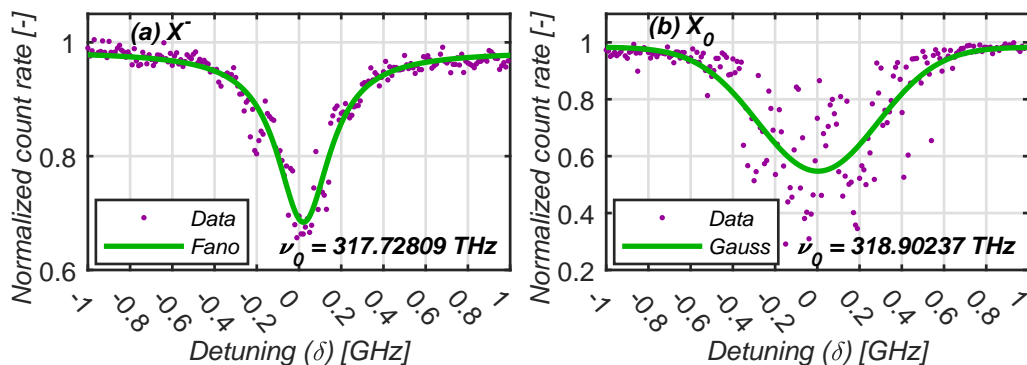


Figure 4.4: Normalised RT data with (a) X^- data and a Fano fit (b) X_0 data and a Gaussian fit. (a) Shows a measurement without telegraph noise, allowing a fit to the Fano-shape function to determine the linewidth and transmission dip visibility. (b) Shows a measurement with telegraph noise fitted by a Gaussian function since we assume random uncorrelated noise. The fit is however an improper estimation of the linewidth and transmission dip visibility.

transmission dip should be the deepest. The laser frequency is then swept in steps of 5 MHz across the resonance to obtain the linewidth and transmission dip of the exciton. The transmission dip normalisation is done by tuning the quantum dot in and out of resonance with the voltage. The results of these scans on the example quantum dot are given in Fig. 4.4 with (a) X^- and (b) X_0 .

The two graphs in Fig. 4.4 shows the cause of the difference in prominence between voltage-frequency-maps of Fig. 4.3. The X^- has a Fano lineshape (Fig 4.4 (a)) while the X_0 is affected by *telegraph noise* [161, 162] (figure 4.4 (b)), which hides the lineshape. This telegraph noise is caused by uncontrolled fluctuation in the resonance frequency of the quantum dot by random uncorrelated noise at a timescale of the integration time. Figure 4.5 shows schematically how the noise influences the measurement. The left panel illustrate the quantum dot resonance profile (dotted line) and the laser linewidth (solid line, not to scale). If there would be no noise, the quantum dot resonance is fixed and the laser frequency is swept over the quantum dot profile. The overlap of the two is an indication of their interaction which means a count rate decrease in RT. The measured profile is the convolution of the laser profile and the quantum dot profile. Since the laser linewidth is a few orders of magnitude smaller than the profile of the quantum dot and smaller than the frequency step made in the measurement, the measured profile will correspond to the quantum dot. When random uncorrelated noise is added to the system (Fig. 4.5 (left panel, dot-dashed lines)), the resonance frequency shifts in the timescale of the noise (right panel, solid curve). The effect of the noise in the measurements depends on the timescale of the noise [49, 163], with three possibilities. The noise is either faster, slower or same order as the integration time. If the noise is a lot slower than the integration time, the resonance

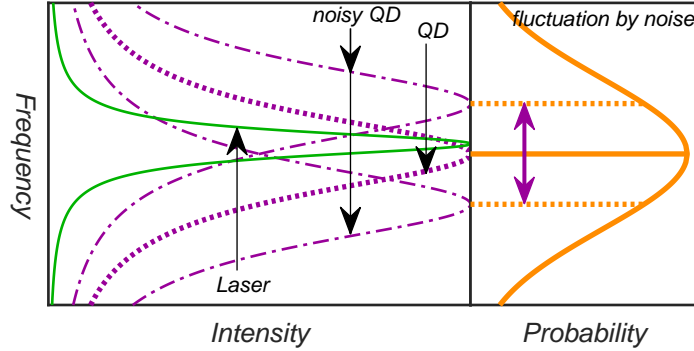


Figure 4.5: Schematic of the influence of random uncorrelated noise on the measured quantum dot profile. The quantum dot (purple dotted line) has a frequency profile which is scanned by a laser with a few order of magnitude narrower linewidth (green solid line). When noise acts on the quantum dot, the resonance changes with the noise in a random uncorrelated pattern.

remains nearly stable over the time of a single measurement and we measure the linewidth of the quantum dot. If we measure the linewidth later on again, the width remains equal but the centre frequency is shifted. When the noise is a lot faster than the integration time, the noise will be averaged out per scanned frequency. The measured profile is therefore a convolution between the quantum dot profile and the noise profile [102, 163]. The last possibility is when the noise has the same timescale. The resonance frequency will be different for every datapoint on the profile measurement, but it remains on that resonance long enough to not be averaged out for a single datapoint. Every datapoint is a measurement with a different resonance frequency randomised by the noise, resulting in telegraph noise. The width of this noise is similar to the linewidth of the convolution of the quantum dot line with the noise.

4.1.2 Effect of WG width variation on QD resonance

The aim is to measure the effect of the width of the nanobeam on the quantum dot resonance frequency and the voltage tuning. We measured on nanobeam waveguides with designed widths ranging from 350 nm to 1000 nm. The actual widths are approximately 10 to 30 nm smaller due to over etching of the sample during fabrication. Different widths of the waveguide are expected to have different coupling between the waveguide and the quantum dot. The stronger the coupling, the lower the lifetimes and therefore larger linewidths. The change in width can also have an influence on the electrical tuning of the resonance, which can play a role on the effect of noise influences. The range of waveguide widths we measured on arises from practical limitations. The 1000 nm wide waveguides were the widest fabricated waveguides, and they are multimode at that width. The min-

imum width of 300 nm arises from the measurements, since we could not find quantum dots at which we could perform RT measurements in waveguides narrower than 300 nm.

The variation of the nanobeam width has an effect on the effective refractive index for different modes [102], and changes the number of allowed guided modes. Nanobeam waveguides with a width below 200 nm are single mode, from 200 to 400 nm the waveguide has 2 modes but the second mode is still weak and can usually be neglected. From 400 nm and wider the waveguides support more than one guided mode and are considered multimode. The change in number of modes has an effect since the quantum dot can couple to different modes, which affect the β -factor [52] for the individual modes. Furthermore is the grating coupler optimised to couple the first order even mode into a single mode fibre. This determines in which waveguide mode the laser is coupled into the waveguide, resulting in the measurement of the coupling between that waveguide mode and the quantum dot.

Since the goal is to measure the effect of the waveguide width on the quantum dot resonance, multiple quantum dots per waveguide have to be measured to obtain statistics. Due to the growth of the quantum dots and the fabrication of the nanostructures, there is no control on how many quantum dots a waveguide contains and where in the waveguide these are located. The longitudinal position has a negligible effect on the coupling between quantum dot and waveguide, but the lateral location has a significant effect on it [152, 164]. Multiple quantum dots were found per waveguide, but not all could be measured due to experimental limitations. A part of the constraints comes from the limited frequency range of the used resonant laser which can scan from 914 nm to 980 nm (327.9 THz to 305.8 THz) and a part because the quantum dot could not be found back in resonance transmission after the measurement with the 860 nm laser. There were a few occasions where the quantum dot resonance could not be found back when switching from the charge plateau map to the frequency scan. The linewidths are therefore determined with the charge plateau scan as a voltage linewidth and then transformed to a frequency linewidth based on the Stark parameters. Another advantage of this process is that a sweep in voltage is faster than a sweep in frequency, reducing the telegraph noise (Fig. 4.5). This process allowed us to measure on 14 quantum dots on which we measured all the X^- excitons and 8 X_0 excitons. We did not measure on X^+ or X^{2-} excitons.

Results of varying waveguide width

The effect of the nanobeam width on the linewidth and the transmission dip visibility is investigated first. The dependencies are shown in Fig. 4.6 with (a) the transmission dip visibility and (b) the linewidth depending on the waveguide width. There are no error bars shown to avoid cluttering, but the transmission dip has a typical error of 5 to 10 percent-points and the linewidth of 60 MHz (X^-) and

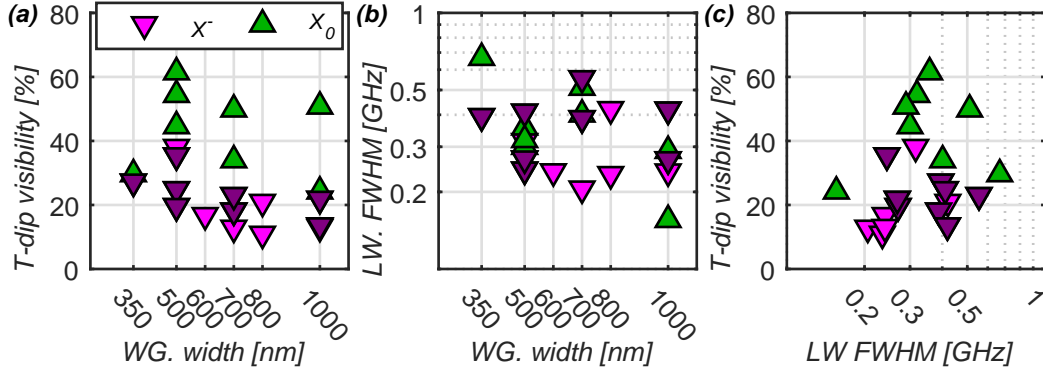


Figure 4.6: (a) Transmission dip visibility depending on nanobeam width, (b) linewidth depending on nanobeam width and (c) transmission dip visibility depending on linewidth for X_0 and X^- . Green upward pointing triangles is measured on the X_0 and the magenta downward pointing triangles on the X^- . The darker magenta downward pointing triangles mark the X^- lines of the same dot as on which the X_0 was measured.

120 MHz (X_0). The green upward pointing triangles are the measured X_0 resonances and the magenta downward pointing triangles the X^- resonances where the dark magenta triangles indicate the X^- excitons on which we also measured the X_0 . None of these two graphs indicate a clear dependency based on the waveguide width, but the X_0 tends to have a larger transmission dip visibility than the X^- while both have a comparable linewidth. From these graphs we can not conclude any dependency between the width of the waveguide and the coupling or the linewidth.

The difference in transmission dip visibility can be explained with the polarisation since the X_0 couples to linear polarised light and the X^- to circular polarised light. We aimed for quantum dots located central in the longitudinal direction, where the waveguide mode is dominantly linear polarised. This allows the X_0 to couple perfectly while the X^- can couple at best only 50% [50, 164]. The transmission dip of the X^- should therefore be at best only 50%.

The dependency between the transmission dip visibility and the resonance linewidth is also investigated. It is expected that the transmission dip visibility decreases if the linewidth is broadened by noise [102]. Figure 4.6 (c) shows the dependency of the transmission dip visibility on the linewidth and shows a faint decrease in transmission dip visibility for larger linewidths on the X_0 . This can be a false trend due to the lack of datapoints in this region, and we can not claim a clear relation from this data. Further investigation on this is required to confirm or decline the relation. This plot does however show that the X_0 has a larger transmission dip visibility than the X^- .

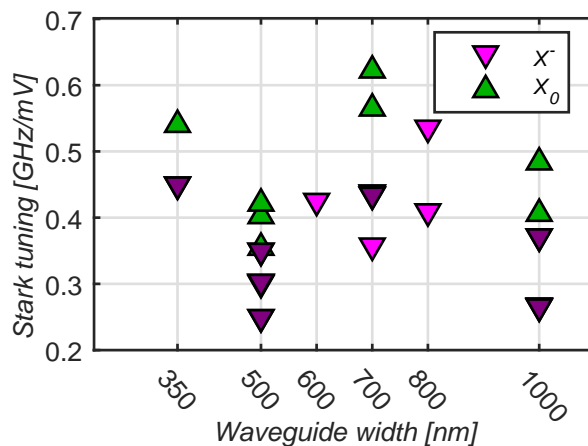


Figure 4.7: Linear stark shift parameter depending on the waveguide width. Green upward pointing triangles is measured on the X_0 and the magenta downward pointing triangles on the X^- . The darker magenta downward pointing triangles mark the X^- lines of the same dot as on which the X_0 was measured.

As last we investigate the Stark parameter depending on the waveguide width which is shown in Fig. 4.7 with the X_0 (green upward pointing triangles) and X^- (magenta downward pointing triangles). All the measured resonances had linear relation and no clear quadratic term was measured. There can however be a small effect from the quadratic Stark parameter which entered in the error margins. From the 500 nm to 800 nm range there appears to be a relation where a wider waveguide has a larger Stark shift parameter. This is however not compatible with the data from the 350 nm and 1000 nm waveguides. This can be explained for the 1000 nm wide nanobeam with the lateral location of the quantum dot which determines the dominant mode that is coupling to, affecting the stark shift parameter. The 350 nm waveguide has only a single datapoint per exciton and might therefore be an outlier. This effect can be investigated further when nanostructures are deterministically fabricated around quantum dots [165, 166].

X_0 versus X^-

Performing the measurements the X_0 appeared to have more often telegraph noise than the X^- , and the X_0 was typically harder to find back in a next measurement than the X^- . This induces the idea that there is some structural difference between the X_0 and the X^- . This difference might come from the extra electron in the quantum dot for a X^- , which would mean that the difference is charge related. We compare the 3 properties we measured for quantum dots on which we could measure both the X_0 and the X^- . This resulted in a total of 8 quantum dots we could use for the comparison. Figure 4.8 compares (a) the transmission dip visibility, (b) the linewidths and (c) the Stark shift parameter of the X^- ver-

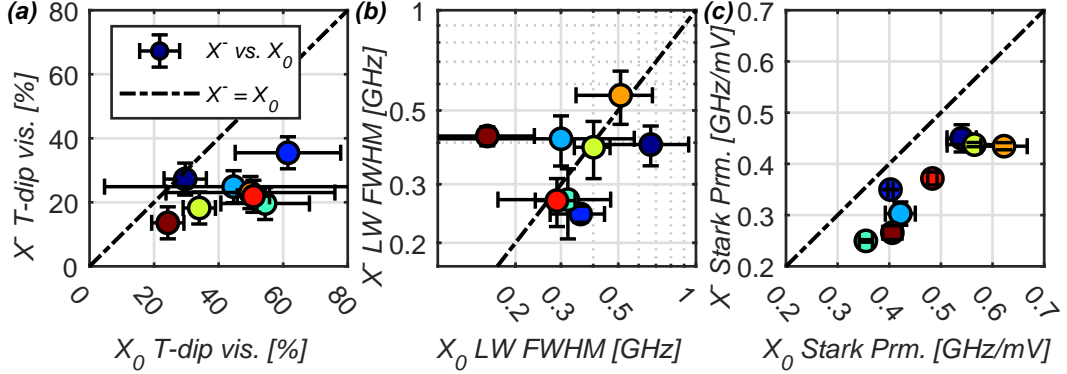


Figure 4.8: Comparison between X_0 and X^- on the eight quantum dots where both excitons could be measured. This graph compares (a) transmission dip visibility, (b) linewidth and (c) stark parameter. The colour of the datapoints indicate the quantum dot on which was measured.

sus the X_0 . The datapoints have unique colours, but the same colour across different graphs indicate that it is measured on the same quantum dot. The dashed lines indicate where the X^- and X_0 would be equal for that property. Figure 4.8 (a) confirms that the X^- has a lower transmission dip visibility than the X_0 , and Fig. 4.8 (b) shows that the linewidths are comparable. The error bars in Fig 4.8 (b) are smaller for the X^- , indicating that there is less noise on the data. This is related to the telegraph noise (Fig. 4.5), which was seen more often on the X_0 . Figure 4.8 (c) shows that the Stark parameter for the X_0 is consistently larger than for the X^- , but they are correlated since the quantum dots with a larger Stark parameter on the X_0 also have a larger Stark parameter on the X^- . This indicate that electrical or charge noise can be the noise source for the linewidths because the X_0 is more sensitive to the electrical environment and has more noise.

All given expectations require further investigation to confirm or deny any hypothesis made in this analysis since the data sets are not big enough to make a deterministic statement. Further work might include deterministic locations of nanostructures around quantum dots to avoid influences from the lateral position of the quantum dot in the waveguide.

4.1.3 Purcell enhancement in photonic crystal waveguides

Quantum dots in a photonic crystal waveguide couple to the waveguide depending on the Local Density of States (LDoS) [97, 167]. The waveguide creates a guided mode in the bandgap to which a quantum dot in the waveguide can couple. The frequency edges of the guided mode have an increased LDoS meaning that the coupling between a quantum dot and the waveguide is enhanced in that regime.

Obtaining electrical control over the resonance frequency of a quantum allows to tune an exciton in and out of this bandedge. This results in a change of coupling depending on the bias voltage, translating into a decay rate into the waveguide that can be electrically tuned. Tuning this decay rate allows for a quantum dot source with a tuneable β -factor, or to tune a quantum dot into a localised mode.

The idea of the measurement is illustrated in Fig. 4.9 which shows the simulation of the Purcell enhancement depending on the resonance frequency scaled to the lattice parameter a . The simulation is performed for $r = a/3$, which is different from our experiment since we have $r \approx a/2$. This results in a rescaling of the frequency axis and Purcell enhancement, but the fundamentals remain equal. The red arrow indicate the direction we tune the quantum dot resonance. The resonance is in a guided mode with low Purcell enhancement and is tuned across the bandedge where the Purcell enhancement increases. The dashed lines are indicators used in the paper for other referencing.

The sample used in this experiment has a $P-I-N$ -diode structure to allow electrical tuning of the quantum dot resonance. The type of diode structure changed compared to the nanobeam waveguides since the $P-I-N$ -diode is found to have a larger tuning range of the resonance frequency. The first step towards a tuneable source is to find a quantum dot that can be electrically tuned into the bandedge and measure the lifetime and spectral linewidth depending on the voltage. The bandedge of the photonic crystal has to be measured to, which is done by performing a transmission measurement on the waveguide with a tuneable CW laser. When the transmission drops below 10% of the maximum transmitted light we obtained the cutoff wavelength of the bandedge. Next is to find a quantum dot that is spatially located in the photonic crystal waveguide and emits photons with a wavelength near the bandedge. This is done with the same procedure as in Sec.

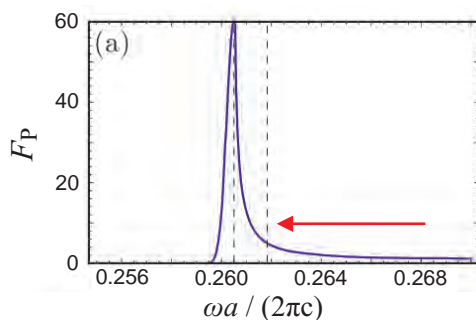


Figure 4.9: Adapted from [50]. Example of the Purcell enhancement depending on emission frequency. The frequency axis is scaled with the lattice parameter a of the photonic crystal lattice. The frequency axis is shifted compared to our structure since this is simulated for $r = 3/a$ while we have $r = a/2$. The red arrow shows the tuning direction of the resonance of our quantum dot.

4.1.1 by scanning the longitudinal location of the laser spot and tune the bias voltage when a quantum dot is found to measure if the quantum dot can be tuned into the bandedge.

The quantum dot used in this measurement is found in a waveguide with a designed hole radius of $r = 72$ nm with a lattice parameter of $a = 248$ nm. Simulations show a cutoff wavelength of $\lambda_c = 1036$ nm, but pre-calibrated fabrication processes results in a cutoff wavelength in the range of $\lambda_c = 910 - 960$ nm. The measured cutoff wavelength is 934.9 ± 0.3 nm and the found quantum dot could be electrically tuned from 934.8 nm to 936.2 nm, which is through the cutoff wavelength. Since this quantum dot fulfils the requirement to be electrically tuneable across the bandedge (through the cutoff wavelength), we measured linewidths and lifetime of this quantum dot.

Purcell enhanced lifetime and linewidth

We measure the lifetime and linewidth of the quantum dot as it is tuned across the photonic crystal bandedge. The lifetimes are measured via pulsed p-shell excitation (Sec. 2.1.4) from the top, with a 3 ps pulse at a 72.6 MHz repetition rate. The emission is collected through the waveguide and spectrally filtered via a grating filter (± 0.3 nm bandwidth) tuned to the desired emission wavelength. The voltage and excitation wavelength are optimised for maximum detection count rate. The detected counts are recorded with a timestamp (4 ps resolution) of arrival relative to the latest excitation pulse. A histogram is made of all these arrival times, from which the lifetime can be calculated by the exponential decay in the histogram. The linewidths are measured via a resonance fluorescence measurement (Sec. 2.2.3) with a CW laser. The laser in the collection path is filtered out by polarisation and the collected photons are sent to the detector from which the count rates are determined.

The first measurements consisted of measuring the lifetime at three different emission wavelengths by tuning the applied voltage, which are 935.0 nm (381 mV), 935.5 nm (100 mV) and 936.0 nm (-60 mV). Increasing the wavelength pushes the excitation into the bandedge which increases the number of decay channels and should result in a decreased lifetime and increased linewidths. Figure 4.10 shows the lifetime and linewidth measurements performed on this quantum dot with (a-c) the lifetime and (d-f) the linewidths. The emission wavelength are (a,d) 935.0 nm, (b,e) 935.5 nm and (c,f) 936.0 nm. The top graphs show the measurement data (green dots) and fit (purple line) where the lifetimes are fitted with an exponential convoluted with the *Instrument Response Function* (IRF), and the linewidths are fitted with a Fano function. The bottom graph shows the residue between the data and the fit, to determine the quality of the fits. The only relation shown in the residue is that the larger the exact number, the larger the residue. A histogram of the residue is made (bottom right) with a Gaussian fit

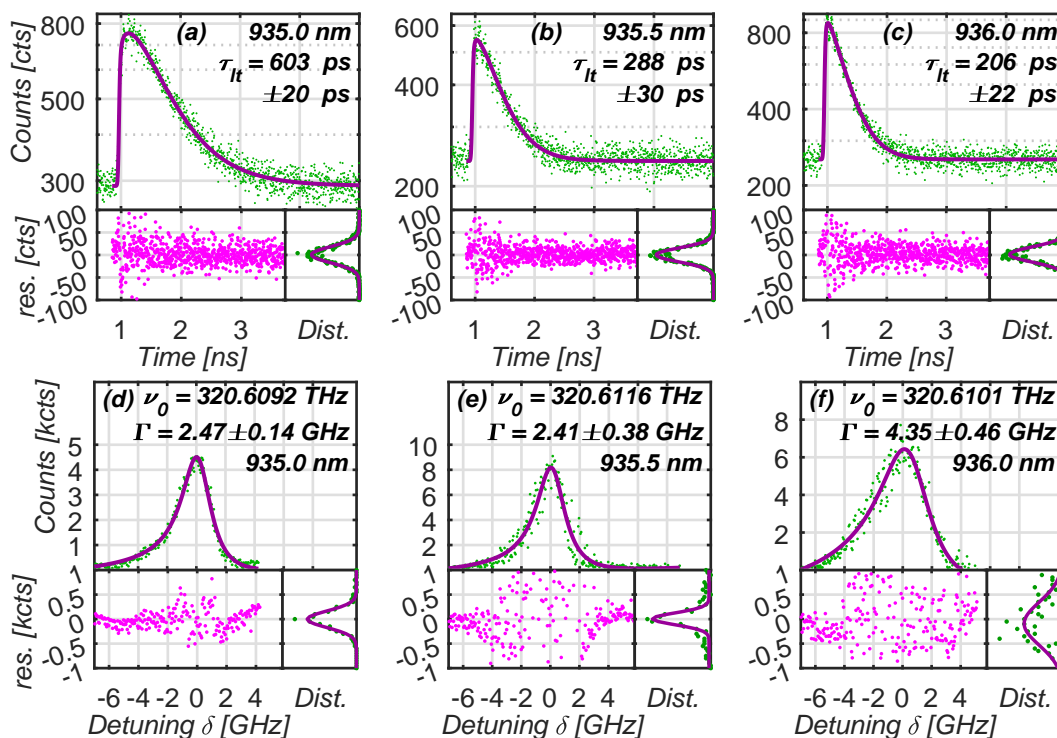


Figure 4.10: **(a-c)** Lifetime and **(d-f)** linewidth measurements for different voltages with resonance wavelengths at **(a,d)** 935.0 nm, **(b,e)** 935.5 nm and **(c,f)** 936.0 nm. Top graphs show the measurement results (green dots) and the fit (solid purple line), where the linewidths are fitted with a Fano-lineshape. The bottom graphs shows an analysis of the residual with left the residue between the fit and data over time ((d-f) frequency), and right a histogram of the residue (green dots) with a Gaussian fit (solid purple line).

fixed around zero showing that the residue follows a Gaussian distribution. From this we conclude that the fits represents the data.

The results from the lifetime and linewidth measurements are shown in Fig. 4.10 and summarised in Tab. 4.1. This shows that the measured lifetime decreases while the resonance is tuned into the bandedge, indicating that we Purcell enhance the coupling. The lifetime limited linewidth can be calculated from this lifetime ($\gamma_{lim} = \frac{1}{2\pi\tau_{lt}}$) and is shown in the third column of Tab. 4.1. The measured linewidths are shown in the last column and are at least a factor 4 larger than the lifetime limited linewidth. The measured linewidths at an emission of 935.0 nm and 935.5 nm are also equal to each other. This indicate that we cannot measure the Purcell enhancement from the measured linewidths. Since the Fano-fits to the linewidths resulted, the broadening can be due to pure-dephasing [50, 168, 169].

λ [nm]	τ_{lt} [ps]	Γ_{lim} [GHz]	Γ [GHz]
935.0	603 ± 20	0.264 ± 0.006	2.47 ± 0.14
935.5	288 ± 30	0.552 ± 0.016	2.41 ± 0.38
936.0	206 ± 22	0.772 ± 0.023	4.35 ± 0.46

Table 4.1: Measured lifetimes and linewidths on varying emission wavelengths. The measured linewidths are at least a factor 4 larger than the lifetime limited linewidths.

In conclusion, we measured a decreased lifetime while the quantum dot resonance is electrically tuned across the bandedge. The expected increase in lifetime limited linewidth could not be measured since all measured linewidths were more than a factor 4 larger than lifetime limited linewidth as can be seen in Tab. 4.1. This experiment requires more study and can greatly benefit from deterministic fabrication of nanostructures around quantum dots.

4.2 Building a SPDC source

Quantum dots embedded in nanostructures are not the only single photon sources. Another common single photon source is the SPDC source (Sec. 2.4). A temporary project was performed at the *Clarendon Laboratory* in the *department of physics* at the *University of Oxford* to allow a study on these type of sources. This allows the understanding of these source and the comparison between SPDC sources and quantum dot single photon sources. The project consisted of setting up and characterise an SPDC source for a quantum walk experiment [170]. This section focus on the experiments perform to set-up the SPDC source and to trace down possible problems.

The source described in this section is a type-II SPDC source made with a *Periodically Poled KTP*-crystal (PPKTP) with a poling period designed to convert into co-linear photons. The goal is to use the source for quantum walks with multiple photons where both signal and idler can be simultaneously used as an input photon. These photons should therefore overlap in spectrum.

The crystal is pumped with a pulsed laser at 80 MHz and a wavelength of 775 nm which bandwidth is tuned with a high-pass and low-pass filter. A fraction of the laser is tapped into a fibre towards a spectrometer to record the spectrum. The non-tapped light is filtered by a spatial filter and focused on the PPKTP. The PPKTP has a poling period of $46.205 \mu\text{m}$ to ensure phase matching of co-linear spectral overlapping photons at 1550 nm. The setup is designed for type-II conversion, resulting in photons with orthogonal polarisation which are split by a PBS. The laser is filtered out with a low pass filter, and the separated photons are individually filtered with bandpass filters. The setup is schematically drawn in Fig. 4.11.

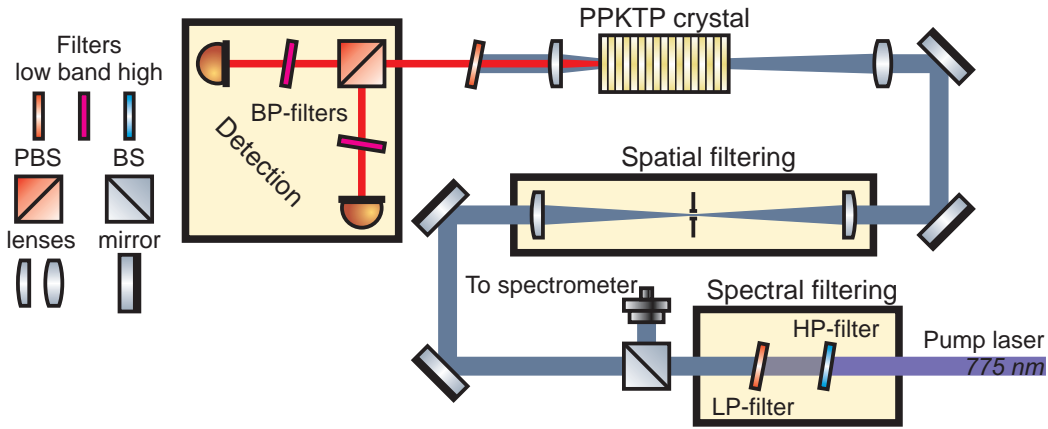


Figure 4.11: Schematic of the SPDC source. The pump beam consists of a 80 MHz pulsed laser with a central wavelength of 775 nm. The bandwidth of the laser can be tuned with a high-pass and low-pass filter followed by a spatial filter for mode matching. The laser is focused on a *Periodically Poled KTP*-crystal (PPKTP) where the poling is phase matched to obtain co-linear photons. The polarisation of the laser is setup for type-II conversion allowing the photons to be split with a PBS. The pump laser is filtered out with a low-pass filter.

The spectral properties are defined by the crystal and pump laser and will be briefly discussed. The focus is on the single photon properties from the source, focused on the unconditioned second order correlation function.

4.2.1 Optimising spectral properties

The spectral properties of the generated photons occur from the pump laser and the poling period of the crystal since these bind the energy conservation and phase matching. Both relations are simulated for the crystal described in Fig. 4.11, with varying linewidth for the pump laser with a centre wavelength at 775 nm. The phase relation is independent of the pump linewidth, but depend on the central wavelength and the non-linear crystal. Figure 4.12 (a) shows this phase relation for a pump laser at 775 nm with on the axis the signal and idler photon wavelength and the plotted map is the generation probability of that specific signal-idler pair. This shows the local maximum as given by Eq. 2.38. The non-zero linewidths of the pump laser results in a non-zero linewidths for the generated photons, as shown in Fig. 4.12 (b,top). This shows the energy conservation for a pump laser at 775 nm with a non-zero FWHM of the linewidth (given above the diagram). The plotted map is the probability distribution of generating a signal-idler pair with a certain wavelength relation.

Combining the two relation result in a *Joint Spectral Intensity* (JSI) giving the intensity relation between the signal and idler photons (Fig. 4.12 (b,bottom)).

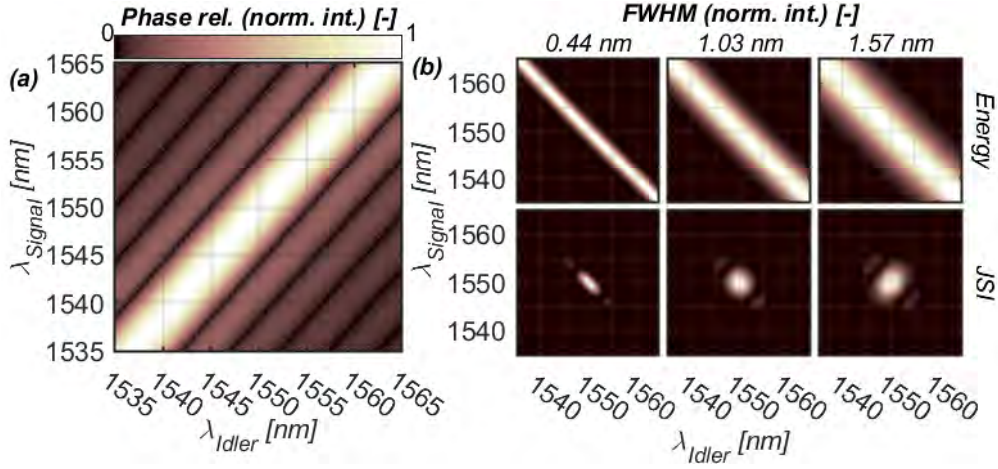


Figure 4.12: **(a)** Phase relation for a PPKTP crystal with a poling period of $46.205 \mu\text{m}$. This shows the local maximum occurring in the phase matching (Eq. 2.38) **(b)** Top: Energy conservation relation a pump laser with three different linewidths of the pump with a central wavelength of 775 nm . Bottom: *Joint Spectral Intensity* (JSI) for the three different FWHM settings.

The JSI indicates that there is a limited wavelength range for the signal and idler photons and it visualises if there is a correlation between the wavelengths of the signal and idler. This correlation is visualised by a non circular distribution. For example, if we look at the case where the pump laser has a FWHM of 0.44 nm , the idler photon decrease in wavelength when the signal photon increases in wavelength. This allows us to obtain information about one of the photons by measuring the other photon. This correlation between the signal and idler can be described via the Schmidt number (K) [137, 171] which indicates an effective number of modes. In an ideal case the Schmidt number $K = 1$, resulting in a single effective mode and would yield no correlation between signal and idler photons. When the Schmidt number increases, the number of effective modes increases and the correlation in the JSI increases as well. This Schmidt number can be directly related to the expected unconditional $g^{(2)}(0)$ as [171]

$$g^{(2)}(0) = 1 + \frac{1}{K}. \quad (4.1)$$

The Schmidt number is calculated from the same simulations as in Fig. 4.12 for a range of linewidths. The resulting $g^{(2)}(0)$ depending on the linewidth is shown in Fig. 4.13 which shows that a maximum in $g^{(2)}(0)$ exist at a finite linewidth. This optimum is reached at a linewidth FWHM of 1.03 nm resulting in a maximum $g^{(2)}(0) = 1.83$. The markers in Fig. 4.13 indicate the linewidths for which the energy conservation and the JSI are shown in Fig. 4.12 (b).

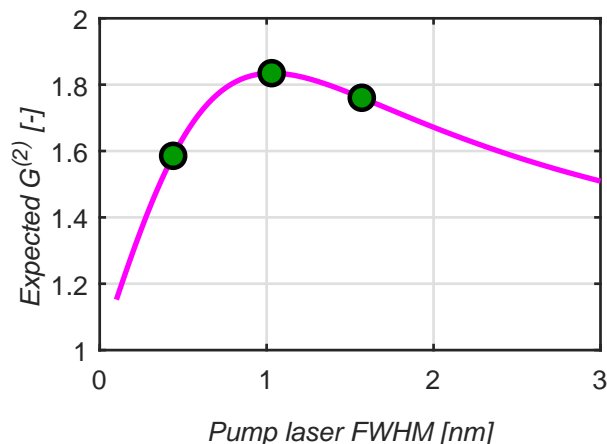


Figure 4.13: Calculated $g^{(2)}(0)$ depending on the pump laser linewidth. This graph indicates a maximum $g^{(2)}(0) = 1.83$ with a FWHM of 1.03 nm. The markers on the graph indicate the three linewidths of which the energy relation and JSI are shown in Fig. 4.12.

4.2.2 Optimising built SPDC source

Knowing what to expect from the source, we can build and optimise the source setup. The first step is to tune the linewidth of the pump laser to optimised unconditional $g^{(2)}(0)$, which is expected to be at a pump linewidth of 1.03 nm with $g^{(2)}(0) \rightarrow 1.83$. The linewidth is manually controlled by angular tuning of the high and low pass filter in the spectral filtering section (Fig. 4.12). We measured at linewidths ranging from ~ 0.7 nm to ~ 1.5 nm which spans over the expected optimum of ≈ 1.03 nm. The coincidence and single rates are measured and used to calculate the unconditional second order correlation function from Sec. 2.4.

The results are shown in Fig. 4.14, indicating a second order correlation $g^{(2)}(0) > 2$. Random noise processes would result in a $g^{(2)}(0) \rightarrow 1$, which is opposite from what is measured. The noise introducing this enhanced $g^{(2)}(0)$ must therefore be a correlated noise. Four different possible noise sources which would increase the $g^{(2)}(0)$ were investigated. These noise sources are: 1. Other order generation processes 2. Mixing of $g^{(2)}(0)$ and $g^{(1,1)}(0)$ 3. Detection crosstalk 4. Time varying power

The first two points are related to each other, but have different origins. Point 2 means that in a single generation event, the signal and idler photons are not fully separated resulting correlation measurements between the signal and idler photons, which is the $g^{(1,1)}(0)$. Point 1 indicate processes such as four wave mixing and Type-I or Type-0 SPDC processes. Both processes could generate photon pairs that are not fully separated by the PBS which would result again in a sampling from the $g^{(1,1)}(0)$. The scenario of four-wave mixing process is simulated by

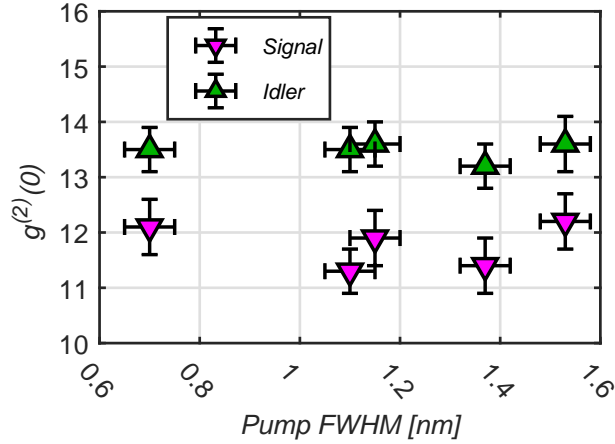


Figure 4.14: The measured $g^{(2)}(0)$ depending on the linewidth of the input laser as measured on the spectrometer. The maximum value that $g^{(2)}(0)$ is able to reach in a noiseless environment is $g^{(2)}(0) = 2$. The measured value is higher, indicating that correlated noise is present in the setup.

a postdoc which showed that this process should not occur. If four wave mixing would occur, the photons would have a significant different wavelength that are blocked by the band-pass filters. Type-I and Type-0 are also simulated for the system and are predict to not occur. If these would still occur, the photons would have the same polarisation meaning. This makes it impossible for them to split on the PBS and result in measuring the $g^{(1,1)}(0)$, but it can only be measured in either the signal or the idler path. The measurement shows that both have a $g^{(2)}(0) > 2$ which means that either both processes occur or the noise has a different source.

Mixing of $g^{(2)}(0)$ and $g^{(1,1)}(0)$

The second point is the mixing of $g^{(2)}(0)$ and $g^{(1,1)}(0)$. When the signal and idler photon are imperfectly split by the PBS, the measurements samples from the $g^{(1,1)}(0)$ which would increase the measured correlation [171, 172]. This increase occurs since $g^{(1,1)}(0) = 3 + 1/\bar{n}$ [172], which goes to infinity for low generation probabilities since $\bar{n} \propto \eta_g$. The mixing can have two origins which are both related to the PBS. The first origin is that the polarisation axis from the crystal and not perfectly projected on the PBS, and the second origin is that the PBS can has imperfect separation of the polarizations. The imperfect projection of the polarisation axes is tested by adding a half wave plate between the crystal and the PBS and rotate this to minimise the coincident counts. This resulted in a wave plate angle of 0° and a $g^{(2)}(0)$ that remained equal to what it was before. The imperfect splitting was tested by adding a polarizer with an extinction of 1 : 100.000 in the signal and idler path to suppress the photons with a wrong polarisation. This ini-

tially reduced the second order correlation by $g^{(2)}(0) = 1.8 \pm 0.1$. These polarizers were removed after the confirmation expecting the $g^{(2)}(0)$ to raise back to a high value [†], but the $g^{(2)}(0)$ remained initially on 1.8 ± 0.1 . This makes the splitting unlikely to be the cause of the increased $g^{(2)}(0)$. This shows that the mixing of $g^{(2)}(0)$ and $g^{(1,1)}(0)$ is unlikely but not fully excluded as the source for the unreasonably high $g^{(2)}(0)$.

Detection crosstalk

Crosstalk in the detection scheme would result in a larger $g^{(2)}(0)$ since it induces correlation that does not exist. This crosstalk can come from either the single photon detectors or from the detection electronics. All cases of crosstalk occur from the induction of an electrical pulse from a different electrical pulse. This extra pulse is then measured by the detection electronics, which results in a correlation event.

Crosstalk induced by the detection electronics is tested by having cable connected to one channel, while the other channel has no connection (no electrical load). The connected channel is detected to the single photon detector, which receives a stream of photons. If the crosstalk is induced by the detection box, this test setup should result in correlation between the two channels. Crosstalk in the single photon detector is tested by connecting both detectors to a channel on the detection electronics and sent a stream of photons to only one detector. If there is crosstalk somewhere on the detection of the photons, a correlation between the two channels should arise. None of these tests showed correlation between the channels, removing crosstalk as a possible source for the increased $g^{(2)}(0)$.

Time varying power

The last noise source we investigated is a time varying pump power. When the crystal is pumped with a time varying power, the generation rate fluctuates along with the pump power. This introduces correlation on the timescale of the fluctuation and therefore increases the non-time resolved $g^{(2)}(0)$. The expected areas where power fluctuations can occur are the laser itself, the spectral filtering setup and the spatial filter setup. Fluctuations in the laser itself can happen due to internal process in the laser itself resulting in an unstable output power. Fluctuations around the spectral filter setup can occur when the pump laser had spectral fluctuations. These fluctuations result in a different power in the spectral region that is transmitted inducing power fluctuations. The spatial filter induces power fluctuations when the output laser beam is not spatially stable or if any optics mount is mechanically unstable.

[†]The notation of high value is used since between every step the measured $g^{(2)}(0)$ varied between 100 and 5.0 in an inexplicable manner.

Power fluctuations induced by the spectral or spatial filter are measured by placing a beamtap before the filter where the tapped signal is measured and correlated to the power measured after the filter. Doing this for the spectral filter also yielded the stability of the power out of the laser with the power meter on the beamtap. Performing this measurement on the spectral filter resulted in no correlation or power fluctuation.

The measurement over the spatial filter is shown in Fig. 4.15 which is a measurement of 108 minutes with a sampling rate of 1 Hz. The measurement results are normalised to the average power to compare the fluctuations between the detectors. Figure 4.15 (a) shows the normalised measured powers where both measurements are smoothed with a nine-point averaging window to reduce fast noise. This shows that the power before the filter has a small fluctuation without a clear trend. The power after the filter shows a larger fluctuation and an indication that there is a fluctuations on the minute timescale, inducing that there is a long time fluctuation in spatial stability. Figure 4.15 (b) shows the measured data where the averaged measurement is divided by the non-averaged data, for both power meters. The amplitude of the ratio is a measure of how strong of an fluctuation there is at a sub-9 seconds time scale. This amplitude is binned in a histogram, which is fitted to a Gaussian distribution since we assume random noise. The standard deviation (σ) of this Gaussian fit is a measure of the amplitude of the fluctuation. The histogram and Gaussian fits are shown in the right panel of Fig. 4.15 (b) and show a $\sigma_b = 0.22\%$ and $\sigma_a = 0.53\%$ where b indicates before the filter and a after the filter.

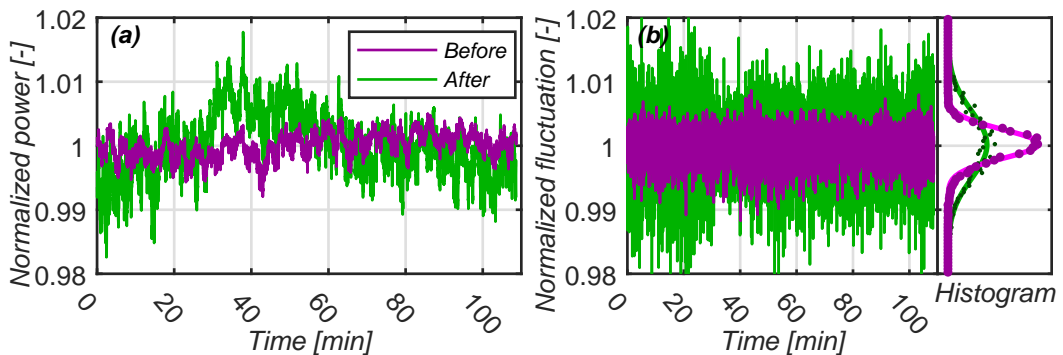


Figure 4.15: Result from measuring the power before and after the spatial filter over a period of 108 minutes with a 1 Hz sampling rate. Measured powers are normalised to the average power to compare the before and after data. (a) Before and after data smoothed with a nine-point averaging window to reduce fast noise. The data after the filter appears to fluctuate more at a certain time interval. (b) Division of the raw data with the nine-point averaged data. The fluctuation is an indication of the amplitude of the fluctuation in a non-resolvable time scale.

Measuring the power before and after the spatial filter indicate that the beam is not spatially stable on sub-Hertz and sup-Hertz timescales. The sub-Hertz fluctuations can come from mechanical oscillations in the optomechanics or from any macroscopic mechanical element connected to the setup. The faster fluctuations are expected to come from the laser itself from the dithering function from the laser. The dithering allows the laser to mode-lock itself in a changing environment, but the output laser beam obtains a small pointing rotation over time. This typically happens at speed ranging from 30 Hz to 60 Hz. Since the laser is coupled free-space to the photon source, this effect is first visible on the spatial filter.

This could unfortunately not be investigated further due to a fixed time limit for the external project. The dithering of the laser could therefore not be confirmed anymore, as well if this could have increased the measured $g^{(2)}(0)$ of the SPDC-source.

This section showed the set-up of an SPDC source during a temporary project. The source was designed for type-II conversion with spectrally overlapping co-linear photons. The $g^{(2)}(0)$ was expected to reach $g^{(2)}(0) = 1.83$ due to the design parameters, but the measured $g^{(2)}(0)$ reached values higher than what should occur ($g^{(2)}(0) \gg 2$). This means that there is more correlation in the an individual path than expected. Different sources of the correlation noise were investigated, from which the laser dithering and the mixing with a $g^{(1,1)}(0)$ are the most likely sources. They could however not be experimentally confirmed.

4.3 Comparison SPDC and Quantum Dots

Two different type of single photon sources are characterised with the intention of using these source for single photon applications. Both sources have intrinsically different characteristics, which will be compared to each other. The three core properties we compare are the single photon purity (second order correlation function), the photon indistinguishability and the single photon generation rate.

Second order correlation

The first property to compare the two sources on is the second order correlation function, measured via an HBT setup (Sec. 2.3.2). The single photon purity determines the operation fidelity of applications. For a quantum dot is the intrinsic $g^{(2)}(0) = 0$, since a single excitation can emit only one photon. This can however not be measured since any uncorrelated noise will bring the $g^{(2)}(0) \rightarrow 1$. How far closer to 1 depends on the prominence of the noise. When the quantum dot is excited with a strong laser pulse, it is also possible to obtain multi-photon states due to coupling between the quantum dot and the strong laser pulse [173]. Different groups researching report values for the second order correlation measurement. Notable values consist of $g^{(2)}(0) < 0.6\%$ [95] and $g^{(2)}(0) = 0.7 \pm 0.1\%$ [60]. In

[95] they measured in a suspended nanobeam waveguide terminated with a taper for high collection efficiency. The quantum dot was cooled down to 4.2 K and excited with a quasi-resonant laser. The collected photons were filtered to remove the phonon sidebands. In [60] they measured on a quantum dot in a micropillar cavity with a 2 μm diameter cooled down to 4.3 K. The interest of this work becomes more clear in the photon indistinguishability.

Since an SPDC has random generation of photon pairs it has to be heralded on one of the two generated photon to perform deterministic operations. The conditioned second order correlation function for a SPDC source is $g^{(2)}(0) = 2\eta_g$ (Eq. 2.43) in the approximation that the generation rate is small. This shows that the SPDC source cannot reach perfect single photons, but it can be tuned to an arbitrary value. An SPDC source is from complexity less sensitive to noise sources than quantum dots, allowing the tuning of the $g^{(2)}(0)$ to a similar value at the cost of generation rate.

Indistinguishability of single photons

The next comparison is the indistinguishability of the photons generated by the two different sources and can be measured with a HOM-setup (Sec. 2.3.3. An ideal two level emitter would have an indistinguishability between consecutive photons of $V_{HOM} = 100\%$. When the quantum dot is cooled down to a finite temperature ($T > 0$ K), the HOM-visibility is reduced depending on the temperature and confinement dimensionality [174]. Noise sources limits the HOM-visibility too since they can fluctuate a property of one of the photons, causing a partial distinguishability on the timescale of the noise.

Current state of the art measurements of single photon indistinguishability for quantum dot sources consist of $V_{HOM} = 94 \pm 1\%$ ($\Delta t \approx 13$ ns) [95] and $V_{HOM} = 94.8\%$ ($\Delta t \approx 289$ ns) $V_{HOM} = 93.2\%$ ($\Delta t \approx 830$ ns) $V_{HOM} = 92.1 \pm 0.5\%$ ($\Delta t \approx 14.7$ μs) [60]. In [60] was the indistinguishability measured over a long time scale to ensure that the photons are still indistinguishable for applications interfering far away photon. The timescale of 830 ns is relevant to the spatial-to-temporal mode converter from Ch. 3, since the longest timescale of photons their is $\Delta t = 60/(76.2 \cdot 10^6) \approx 790$ ns.

SPDC sources have an intrinsic $V_{HOM} = 100\%$ but are also influenced by noise. An SPDC source has however less noise in the photon generation than the quantum dot resulting in a high indistinguishability between photons from the same SPDC source. A more interesting metric is the indistinguishability across different SPDC sources, which arise from the control of fabrication of the crystals. State of the art result on this is $V_{HOM,n-SPDC} = 96.2 \pm 1.1\%$ [175], which is in the range of photons from a single quantum dot source. This results that multiple SPDC sources can be used for single photon applications while the indistinguishability is similar to the quantum dot sources. This strategy allows an increase of the photon

generation rate, which we compromised on for the single photon purity.

Generation rate

The last part to compare the generation rate of single photon of the two sources with each other. The generation rate is an important factor since multi-photon experiments depends on an efficient source of single photons to reduce the required time for a single operation. The generation rate is already hinted at in the other comparison sections. An ideal two level emitter would emit a single photon with every excitation pulse resulting in a generation efficiency of 1. This is not yet measured and state of the art work consist of a generation efficiency of 34%, since they measure a single photon rate of 25.6 MHz while pumping at 76 MHz [54]. The second order correlation function they measured is $g^{(2)}(0) = 2.7\%$. An SPDC that would have the same second order correlation function would have a maximum generation rate of $\eta_g = 1.3\%$, which is almost a factor 30 lower than the generation efficiency of the quantum dot source.

This lack of generation efficiency can be overcome by using multiple SPDC sources since we discussed that the indistinguishability between SPDC source is similar to photons from a quantum dot. Multiplexing of these sources is possible since the herald indicates which SPDC-source generated a photon pair, which allows an optical circuit to route that SPDC source to the output. If this circuit would be perfect, 32 SPDC sources with $\eta_g = 1.3\%$ would be required to obtain an effective $\eta_g = 34\%$. The same multiplexing can be done with a single SPDC-source, but the effective output rate will be reduced depending on the number of temporal modes combined [46, 47]. The herald now notify in which temporal mode the photon pair was generated allowing a circuit to delay the photon into a predefined temporal output mode.

There are applications which require the photons to be in separated spatial modes. This eliminates the requirement of routing all SPDC-sources into a single spatial mode, while a quantum dot source requires a circuit to split the photons into different spatial modes. A much studies application for multiple SPDC sources is scattershot BosonSampling [175–178].

This section gave a brief overview of how the SPDC and quantum dot source compare to each other in terms of single photon purity, indistinguishability and generation rate. It also discusses how the generation rate is affected by the other two and how to utilise the sources to their strength.

4.4 Conclusion

This chapter showed the characterisation of two commonly used single photon sources, a quantum dot embedded in a nanostructure and a Spontaneous Parametric Down Conversion source. On the quantum dot we measured the spectral properties and the Stark-tuning depending on the width of the nanobeam waveguide for the X_0 and X^- excitons. The two different excitons are compared to each other afterwards. We showed that there was no dependency visible on the linewidths or transmission dip for the waveguide widths. However, there appeared to be a dependency on the Stark-parameter which has to be investigated further. Comparing the X_0 to the X^- showed that the X_0 has larger transmission dips while the linewidths remained equal. The X_0 is influenced stronger by noise since this exciton has more frequently linewidths with telegraph noise. This is expected to be related to charge noise since the X_0 has a larger Stark-parameter, which result in a larger sensitivity for charge noise around the quantum dot.

The second characterisation measurement on the quantum dots consisted of tuning a quantum dot resonance into the bandedge of a photonic crystal waveguide. This tuning was done by applying a bias voltage that tunes the quantum dot resonance from 934.8 nm to 936.2 nm while the cutoff wavelength was measured at 934.9 ± 0.3 nm. We measured the lifetimes at emission wavelengths of 935.0 nm, 935.5 nm and 936.0 nm with the measured lifetimes of 603 ± 20 ps, 288 ± 30 ps and 206 ± 22 ps respectively. The reduction in lifetime for the resonance is expected by the Purcell enhancement. The increase in linewidths could unfortunately not be measured due to pure dephasing and we measured linewidths of 2.47 ± 0.14 GHz, 2.41 ± 0.38 GHz and 4.35 ± 0.46 GHz. The linewidths were at least a factor 4 larger than the lifetime limited linewidths (264 ± 6 MHz, 552 ± 16 MHz and 772 ± 23 MHz respectively) and did not consistently widen while being tuned into the bandedge. Both measurements could be investigated further when nanostructure can be fabricated deterministically around the quantum dots.

The SPDC source consisted of measuring the second order correlation function of the signal and idler photons, which yielded an unexpected large $g^{(2)}(0)$. The unconditional second order correlation function for an SPDC source should be $g^{(2)}(0) \leq 2$, meaning we had a noise term inducing correlation. The expected source of the noise is the laser dithering which rotates the pointing of the output laser beam, or mixing of the signal and idler photons ($g^{(1,1)}(0)$). The dithering results in power fluctuation after a spatial filter inducing correlation on a fixed time scale. This could not be confirmed as the noise source due to time constraints. The $g^{(1,1)}(0)$ was tested for, but the results were indecisive.

On the last part we compared a quantum dot source with an SPDC source for multi photon experiments with the focus on the generation rate, single photon purity and photon indistinguishability. The generation rate and single photon purity are tied together for an SPDC source. This source can get an arbitrary small

$g^{(2)}(0)$ at the cost of the photon generation rate. A quantum dot source has these two parameters uncoupled, meaning that it can get a near unity generation rate while photons have a high purity. The efficient generation is not yet measured above 34% [54] due to limited efficiencies. The single photon purity for a quantum dot is still limited since this is strongly influenced by noise. Due to the relation between generation rate and single photon purity, it would require 32 SPDC sources to have a 34% generation probability with the same single photon purity as [54]. This is a possible technique since SPDC sources have high indistinguishability between their photons, even across different sources. The indistinguishability across SPDC sources is similar to the measured indistinguishability between photons from a single quantum dot source allowing stacking of SPDC sources to compensate for the low generation probability.

Heralded Entanglement Generation

Single photons are investigated as a resource for different quantum protocols due to the robustness against environmental influences. This makes photons strong candidates for communication and cryptography, but there are also options for quantum information processing [20, 43, 48, 61, 143, 179, 180]. Different cryptography protocols are investigated such as Quantum Random Number Generators (QRNG) [41, 147, 181–183] and Quantum Key Distribution (QKD)[32–35, 184–188]. Examples for quantum information processing exist of BosonSampling (BS) [26–31, 44, 57, 144, 189, 190] and cluster states [191–193].

The common problem for quantum information processing is the validation of the results. It is assumed that quantum computation has a processing speed advantage over classical computation [194, 195] for specific calculations. Current techniques to validate these quantum processors is via comparisons to statistical test [196, 197] or by using an entangled state [198].

Quantum cryptography focus on the encryption of data to avoid an eavesdropper of listening. The first proposals on QKD and QRNG required the trust that the measurement apparatus worked as promised, making it threat for the data safety. In QKD this can be overcome by implementing Device Independent QKD (DIQKD) [148, 199–205], where the user can test if the apparatus worked accordingly. DIQKD uses entangled photon pairs as a resource where the operation can

be tested via Bells theorem. QRNG requires a method to validate the true randomness of the generated numbers. True randomness does not exist in classical system since all perceived randomness is due to an inability to predict. Quantum systems have a random nature that can help in the generation of true random numbers. Current definitions of randomness compares the generated random numbers via a specific tests. These tests can exclude only certain types of correlation, allowing other types of correlation to exist. Excluding correlations with all statistical test we know does therefore not prove that it is truly random since there might be a correlation in the numbers that is not tested. It is possible to certify a QRNG by showing that the random numbers are generated based on quantum mechanics, which is true random. This can be done via Bells theorem and requires entangled photons as a source for the QRNG [206].

The above examples show that entanglement is a required resource to ensure that quantum protocols perform the desired operation. The generated entanglement has to be deterministic to reduce to possibilities that an eavesdropper gains information, or that the random numbers obtain correlations. This poses a problem since most entanglement generation schemes are probabilistic, resulting in an effective lower efficiency. This problem is overcome by using a scheme that can herald the entanglement so the user knows within a certain efficiency that there is an entangled photon pair. Such a scheme exists in the form of the *Heralded Entanglement Gate* [179, 207] requiring a four photon input state of which two photons are entangled and the other two photons are used as a herald.

Chapter 3 showed a demultiplexed four photon source that can be used as in input to generate entanglement with an entanglement gate. This chapter focuses on the operation of the entanglement gate. First we show how the state evolution of the photons can be calculated. This is followed with the output state and how we can herald the output state. Different types of heralding are shown together with their effect on the output. After the ideal scenario are imperfections added to the calculations, where we focus on either partial distinguishable photons or a limited source and setup efficiency.

5.1 Operation of the heralded entanglement gate

This section introduces the operation of the entanglement gate [207], which is constructed from passive optical components. A schematic view of the gate is given in Fig. 5.1 which has four input photons (port A to D). Each path contains a *Half Wave Plate* (HWP) to orient the photons into a diagonal polarisation. The photons in path A and B are interfered on a PBS, just as the photons in paths C and D . Outputs A' and D' are the paths containing the photons heralded into Bell states. Figure 5.1 shows polarisation analysers in paths A' and D' which are used for Bell-state confirmation, but are removed when the entangled photons are inserted into a following setup. Paths B' and C' are inserted on a *Rotated PBS*

Operation of the heralded entanglement gate

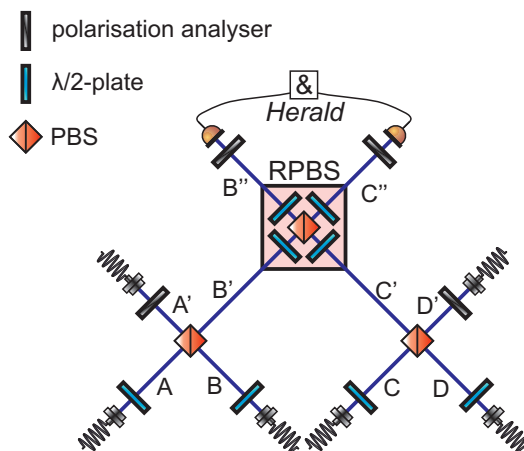


Figure 5.1: Setup of a Heralded Entanglement Gate requiring four indistinguishable photons on the input. Photons are interfered via PBSs after which two photons are used for heralding (B'' and C'') a Bell-state on the outputs (A' and D').

(RPBS) which is constructed of a normal PBS with a HWP at an angle of 22.5° in every path. The outputs B'' and C'' go through polarisation analysers where coincidence counts between different polarisation combinations in B'' and C'' herald different Bell states at ports A' and D' .

The first step in understanding the entanglement gate is to evaluate the operation of the gate assuming perfect input and perfect gate operation. This means that all four inputs contain a diagonal polarisation after the input HWPs, and that all optical components operate on the light in a perfect fashion.

A HWP has a single input path which can contain two polarisation's (horizontal $|H\rangle$ and vertical $|V\rangle$). The operation matrix of the HWP can therefore be written as a 2×2 matrix via

$$\begin{pmatrix} \hat{a}'_H \\ \hat{a}'_V \end{pmatrix} = \frac{1}{\sqrt{2}} \begin{bmatrix} 1 & 1 \\ 1 & -1 \end{bmatrix} \begin{pmatrix} \hat{a}_H \\ \hat{a}_V \end{pmatrix}, \quad (5.1)$$

where a denotes the path the photon is in and the apostrophe denotes the output side of the HWP. Since the diagonal and anti-diagonal states are defined as

$$\begin{aligned} |D\rangle &= \hat{a}'_D |0\rangle = \frac{1}{\sqrt{2}} (\hat{a}'_H + \hat{a}'_V) |0\rangle \\ |A\rangle &= \hat{a}'_A |0\rangle = \frac{1}{\sqrt{2}} (\hat{a}'_H - \hat{a}'_V) |0\rangle, \end{aligned} \quad (5.2)$$

the HWP rotates the horizontal and vertical state into the diagonal and anti-diagonal state.

The transformation from a PBS can be written as

$$\begin{pmatrix} \hat{a}_H^\dagger \\ \hat{a}_V^\dagger \\ \hat{b}_H^\dagger \\ \hat{b}_V^\dagger \end{pmatrix} = \begin{bmatrix} 0 & 0 & 1 & 0 \\ 0 & i & 0 & 0 \\ 1 & 0 & 0 & 0 \\ 0 & 0 & 0 & i \end{bmatrix} \begin{pmatrix} \hat{a}_H^\dagger \\ \hat{a}_V^\dagger \\ \hat{b}_H^\dagger \\ \hat{b}_V^\dagger \end{pmatrix} \quad (5.3)$$

where the horizontal polarisation is transmitted and the vertical polarisation is reflected while it obtains a $\pi/2$ phase shift.

State evolution

The first step in calculating the output of the gate is to calculate the effect of the PBS on an input state of $\psi_{AB} = \hat{a}_D^\dagger \hat{b}_D^\dagger |0\rangle$. This state contains a diagonal photon on both paths A and B and is written out as

$$|\psi_{AB}\rangle = \frac{1}{2} \left(\hat{a}_H^\dagger \hat{b}_H^\dagger + \hat{a}_H^\dagger \hat{b}_V^\dagger + \hat{a}_V^\dagger \hat{b}_H^\dagger + \hat{a}_V^\dagger \hat{b}_V^\dagger \right) |0\rangle \quad (5.4)$$

which is inserted in the PBS from Eq. 5.3. This results in an output of

$$|\psi_{AB'}\rangle = \frac{1}{2} \left(\hat{a}_H^\dagger \hat{b}_H^\dagger - \hat{a}_V^\dagger \hat{b}_V^\dagger + i\hat{a}_{HV}^\dagger \hat{b}_0^\dagger + i\hat{a}_0^\dagger \hat{b}_{HV}^\dagger \right) |0\rangle, \quad (5.5)$$

where the apostrophe denotes the output of the PBS. Path B' contains a HWP due to the RPBS. This HWP can be added in the path resulting in

$$\begin{aligned} |\psi_{AB'}\rangle = & \\ & \frac{\sqrt{2}}{4} \left[\left(\hat{a}_H^{\prime\dagger} \hat{b}_H^{\prime\dagger} + \hat{a}_V^{\prime\dagger} \hat{b}_H^{\prime\dagger} - \hat{a}_H^{\prime\dagger} \hat{b}_V^{\prime\dagger} + \hat{a}_V^{\prime\dagger} \hat{b}_V^{\prime\dagger} \right) \right. \\ & \left. + i\frac{1}{2} \hat{b}_H^{\prime\dagger} \hat{b}_V^{\prime\dagger} + i\frac{1}{4} \left(\hat{a}_H^{\prime\dagger} \hat{a}_H^{\prime\dagger} - \hat{a}_V^{\prime\dagger} \hat{a}_V^{\prime\dagger} \right) \right] |0\rangle. \end{aligned}$$

where the extra dot in the path notation indicates that this is between the first HWP and PBS of the RPBS. The same can be done on path C and D

$$\begin{aligned} |\psi_{CD'}\rangle = & \\ & \frac{\sqrt{2}}{4} \left[\left(\hat{c}_H^{\prime\dagger} \hat{d}_H^{\prime\dagger} + \hat{c}_H^{\prime\dagger} \hat{d}_V^{\prime\dagger} - \hat{c}_V^{\prime\dagger} \hat{d}_H^{\prime\dagger} + \hat{c}_V^{\prime\dagger} \hat{d}_V^{\prime\dagger} \right) \right. \\ & \left. + i\frac{1}{2} \hat{c}_H^{\prime\dagger} \hat{c}_V^{\prime\dagger} + i\frac{1}{4} \left(\hat{d}_H^{\prime\dagger} \hat{d}_H^{\prime\dagger} - \hat{d}_V^{\prime\dagger} \hat{d}_V^{\prime\dagger} \right) \right] |0\rangle. \end{aligned}$$

Both states are now combined to calculate the effect of the PBS in the RPBS. Since the PBS works on paths B' and C' , we write the state in terms of $\hat{b}'^\dagger \hat{c}'^\dagger$ and $\hat{a}'^\dagger \hat{d}'^\dagger$. The states at different points through the rest of the entanglement gate are written out in App. C where the combined state over all four paths is written as $|\psi_{ABCD'}\rangle$. All states that can not result in a coincidence measurement

on $|\rangle_B |\rangle_C$ are removed from the final state (Eq. C.6) to improve visibility on the relevant states.

When a measurement is heralded on a detection event in all four paths, the only part of the state that could have contributed to this coincidence is

$$|\psi_{ABCD}\rangle = \frac{1}{4} \left(\Phi_{A'',D''}^+ \Psi_{B'',C''}^+ - \Psi_{A'',D''}^+ \Phi_{B'',C''}^+ \right) \quad (5.6)$$

with the Bell states [4] (p. 297)

$$\begin{aligned} |\Phi_{A,D}^\pm\rangle &= \frac{1}{\sqrt{2}} (|H\rangle_A |H\rangle_D \pm |V\rangle_A |V\rangle_D) \\ |\Psi_{A,D}^\pm\rangle &= \frac{1}{\sqrt{2}} (|H\rangle_A |V\rangle_D \pm |V\rangle_A |H\rangle_D). \end{aligned} \quad (5.7)$$

This shows that the photons in the output were maximally entangled when a four fold coincidence was measured.

Heralding

We just showed the evolution of the state through the entanglement gate and that a four fold coincidence at the output can only occur when the output photons were entangled. The next step is to use the other two photons as a herald for this entanglement. This allows to connect a different setup after the gate and that we know when an entangled photon pair entered that setup. The detectors in the setup are non-photon number resolving and polarisation sensitive by using an optical element to project on a specific polarisation. The heralding occurs at one of the four detection possibilities of $|H\rangle_B |H\rangle_C$, $|V\rangle_B |H\rangle_C$, $|H\rangle_B |V\rangle_C$, or $|V\rangle_B |V\rangle_C$. There are however more states in path B'' or C'' which can be measured as a herald, e.g. $|H\rangle_B |HH\rangle_C$ or $|H\rangle_B |HV\rangle_C$ also herald for $|H\rangle_B |H\rangle_C$. The heralding is thus a detection on

$$\mu_{\zeta_b, \zeta_c}^{(j)} = \left(\langle 0 | \hat{b}_{\zeta_b} \hat{c}_{\zeta_c} \hat{j}_b \hat{j}_c \right) \quad (5.8)$$

where

$$\begin{aligned} \zeta_\kappa &\in \{H, V\} \\ j_\kappa &\in \{\hat{\kappa}_0, \hat{\kappa}_H, \hat{\kappa}_V\}. \end{aligned}$$

In this projection ζ_b and ζ_c indicate the polarisation states in path B'' or C'' that we herald on. j_κ indicate the polarisation of the extra photons. This can be horizontal (j_H), vertical (j_V) or no extra photon (j_0). Equation C.6 shows that there are 7 possible output states on path A' and D' when heralded on a coincidence in B'' and C'' . The possible states are

$$|\Psi_{A,B}^+\rangle, |\Phi_{A,B}^+\rangle, |H\rangle_A |0\rangle_D', |V\rangle_A |0\rangle_D', |0\rangle_A |H\rangle_D', |0\rangle_A |V\rangle_D', |0\rangle_A |0\rangle_D'.$$

The probability to measure a certain state combined with a herald given by ζ_b and ζ_c is given by

$$\rho_{\Psi_{A,D}^+}^{(\zeta_b, \zeta_c)} = \sum_j \left| \mu_{\zeta_b, \zeta_c}^{(j)} \langle \Psi_{A,D}^+ | \psi_{ABCD} \rangle \right|^2 \quad (5.9)$$

$$\rho_{\Phi_{A,D}^+}^{(\zeta_b, \zeta_c)} = \sum_j \left| \mu_{\zeta_b, \zeta_c}^{(j)} \langle \Phi_{A,D}^+ | \psi_{ABCD} \rangle \right|^2 \quad (5.10)$$

$$\rho_{\epsilon}^{(\zeta_b, \zeta_c)} = \sum_N \sum_j \left| \mu_{\zeta_b, \zeta_c}^{(j)} \langle N | \psi_{ABCD} \rangle \right|^2 \quad (5.11)$$

$$\langle N | \in \{ \langle H |_A \langle 0 |_D, \langle V |_A \langle 0 |_D, \langle 0 |_A \langle H |_D, \langle 0 |_A \langle V |_D, \langle 0 |_A \langle 0 |_D \}$$

where the superscripts of ρ indicate the polarisation combination of heralding and the subscript indicate the measured state on paths A' and D' . The measured state on A' and D' is split in either the $\Psi_{A,D}^+$, $\Phi_{A,D}^+$ or an erroneous state ϵ .

The heralding efficiency can be calculated knowing all the state efficiencies. This is the probability to obtain the entangled state when a herald is measured, which is the ratio between the state efficiency of the herald with the entangled state and the total probability to measure the herald

$$P_s = \frac{\rho_{\Psi_{A,D}^+}^{(b,c)} + \rho_{\Phi_{A,D}^+}^{(b,c)}}{\rho_{\Psi_{A,D}^+}^{(b,c)} + \rho_{\Phi_{A,D}^+}^{(b,c)} + \rho_{\epsilon}^{(b,c)}}. \quad (5.12)$$

The heralding is depending on the operation of the polarisation analyser in Fig. 5.1. The analyser can be set to filter on a polarisation which requires only one detector or it can split the polarizations which requires two detectors (one for each

$(b,c)=$	HH	VV	HV	VH	$HH\&VV$	$HV\&VH$	$HH\&VV\&HV\&VH$
$\rho_{\Psi_{A,D}^+}^{(b,c)}$	$\frac{8}{256}$	$\frac{8}{256}$	0	0	$\frac{8}{128}$	0	$\frac{8}{128}$
$\rho_{\Phi_{A,D}^+}^{(b,c)}$	0	0	$\frac{8}{256}$	$\frac{8}{256}$	0	$\frac{8}{128}$	$\frac{8}{128}$
$\rho_{\epsilon}^{(b,c)}$	$\frac{17}{256}$	$\frac{17}{256}$	$\frac{17}{256}$	$\frac{17}{256}$	$\frac{5}{128}$	$\frac{5}{128}$	$\frac{10}{128}$
P_s	$\frac{8}{25}$	$\frac{8}{25}$	$\frac{8}{25}$	$\frac{8}{25}$	$\frac{8}{13}$	$\frac{8}{13}$	$\frac{8}{13}$

Table 5.1: Probabilities of measuring a $\Phi_{A,D}^+$ or $\Psi_{A,D}^+$ Bell-state or a noise output state heralded on a specific combination with non-photon-number-resolving detectors. This shows that the probability to obtain a heralded Bell-state is at best $\rho = 1/16$ if the type of Bell-state is important and $\rho = 1/8$ if any Bell-state is accepted. The heralding efficiency with non-photon-number resolving detectors is $P_s = 8/13$.

$(b,c)=$	HH	VV	HV	VH	$HH\&VV$	$HV\&VH$	$HH\&VV\&HV\&VH$
$\rho_{\Psi_{A,D}^+}^{(b,c)}$	$\frac{2}{64}$	$\frac{2}{64}$	0	0	$\frac{1}{16}$	0	$\frac{1}{16}$
$\rho_{\Phi_{A,D}^+}^{(b,c)}$	0	0	$\frac{2}{64}$	$\frac{2}{64}$	0	$\frac{1}{16}$	$\frac{1}{16}$
$\rho_{\epsilon}^{(b,c)}$	$\frac{3}{64}$	$\frac{3}{64}$	$\frac{3}{64}$	$\frac{3}{64}$	0	0	0
P_s	$\frac{2}{5}$	$\frac{2}{5}$	$\frac{2}{5}$	$\frac{2}{5}$	1	1	1

Table 5.2: Probabilities of measuring a $\Phi_{A,D}^+$ or $\Psi_{A,D}^+$ Bell-state or a noise output state heralded on a specific combination with photon-number-resolving detectors. This shows an improvement in heralding efficiency up to $P_s = 1$.

polarisation). The advantage of the latter case is that this allows detection when a path contains multiple photons with different polarisation, removing these detection event as a possible herald. This reduces the number of noise herald and improves the heralding efficiency. Another advantage is that this allows the heralding on different polarisation combinations at the same time, which increases the general detection probability. Table 5.1 shows the detection probabilities and heralding efficiency for the case of polarisation filtering and polarisation splitting. When only a single polarisation is mentioned it is assumed to be filtering and when multiple polarisation sets are mentioned as heralds it is polarisation splitting where we identify between the given polarizations. This table assumes non photon-number resolving detectors. In the case of splitting there are two scenarios. We either herald a specific output Bell-state (heralding on $|H\rangle_B |H\rangle_C$ & $|V\rangle_B |V\rangle_C$ or $|H\rangle_B |V\rangle_C$ & $|V\rangle_B |H\rangle_C$), or heralding on having an output Bell-state while knowing which state it is (Heralding on all four possible combinations).

This table shows a heralding efficiency of $P_s = 32\%$ in the case of polarisation filtering and $P_s \approx 62\%$ in the case of polarisation splitting. Replacing the detectors for photon-number resolving detectors improves the heralding efficiency since multiple photons of the same polarisation in a single path can be removed from the heralds. The detection probabilities and heralding efficiencies in this case are shown in Tab. 5.2. Polarisation filtering reaches a heralding efficiency of $P_s = 40\%$ while polarisation splitting reaches a heralding efficiency of $P_s = 100\%$.

5.2 Effects of experimental limitations

The above given calculation assumes a perfect setup, which is unfeasible in an experimental situation. Different effects play a role on how the state evolves. This section introduces the effect from optical components and from an imperfect source. The two used components are a PBS and a HWP, having a transmission efficiency of η_L . The waveplate has a non-perfect retardation of δ_λ and a angle set to α .

The PBS has an imperfection in the splitting of the polarisation, introducing the efficiency of the vertical polarisation being reflected of η_V (where $1 - \eta_V$ is transmitted) and the horizontal polarisation being transmitted of η_H (where $1 - \eta_H$ is reflected). Other limitations occur from the source since there is a limited indistinguishability (Q , section 2.3.3)[†] between the photons with a limited single photon purity. Another imperfection is the generation probability of a photon at every input, which results from the used demultiplexer efficiency (Chap. 3) and source efficiency. These limitations on the generation probability and the single photon purity can be solved by adjusting the input state and do not require a change in the entanglement gate. The indistinguishability is implemented on the beamsplitters, since that is where the different photons interfere with each other. The transfer matrix for the HWP is given in Eq. 5.13, where the loss state is given by \hat{L} and implemented to maintain constant normalisation.

$$\begin{pmatrix} \hat{a}_H^\dagger \\ \hat{a}_V^\dagger \\ \hat{L} \end{pmatrix} = \begin{pmatrix} \sqrt{\eta_L} (\cos^2(\alpha) + \sin^2(\alpha) e^{i\delta_\lambda}) & \sqrt{\eta_L} \sin \alpha \cos \alpha (1 - e^{i\delta_\lambda}) & 0 \\ \sqrt{\eta_L} \sin \alpha \cos \alpha (1 - e^{i\delta_\lambda}) & \sqrt{\eta_L} (\cos^2(\alpha) e^{i\delta_\lambda} + \sin^2(\alpha)) & 0 \\ \sqrt{1 - \eta_L} & \sqrt{1 - \eta_L} & 1 \end{pmatrix} \begin{pmatrix} \hat{a}_H^\dagger \\ \hat{a}_V^\dagger \\ \hat{L} \end{pmatrix} \quad (5.13)$$

The transfer matrix for the PBS in case of partial indistinguishability and losses is given by Eq. D.1 in App. D. The factors in front of the double vertical line denote a general multiplier for that row. The limited indistinguishability is implemented via the Q -parameter (Sec. 2.3.3) and results in an expanding number of modes after a PBS. This modal expansion consist of the indistinguishable modes, and the distinguishable modes with an index to identify from which input the photon is. It is assumed that the already distinguishable modes out of the first PBS set are assumed to be fully distinguishable on the second PBS. The Q -parameter on the second PBS for the already distinguishable modes is $Q_{PBS_2} = 0$, the indistinguishable modes have a $Q_{PBS_2} \neq 0$.

We calculate the effect of indistinguishability and loss on the entanglement gate while assuming pure single photons ($g^2(0) = 0$). First is the effect of only the indistinguishability investigated to which the losses are added later. There are two indistinguishability parameters to investigate since we assume that the indistinguishability between path A and B is equal to the indistinguishability between path C and D . Calculating the output probabilities shows that heralding on $|H\rangle_B |H\rangle_C$ & $|V\rangle_B |V\rangle_C$ has the same probabilities as heralding on $|H\rangle_B |V\rangle_C$ & $|V\rangle_B |H\rangle_C$ with the difference that the output Bell-state is different. The rest of the calculation assumes that the heralding is in the polarisation splitting configuration. The probability to obtain an output Bell-state and a herald is independent of the type of detectors (photon number resolving or not), and is always given by

$$\rho_{\Psi_{A,D}^+}^{(H,H)} + \rho_{\Psi_{A,D}^+}^{(V,V)} = \rho_{\Phi_{A,D}^+}^{(H,V)} + \rho_{\Phi_{A,D}^+}^{(V,H)} = \frac{Q_1^4 Q_2^2}{16} \quad (5.14)$$

[†]Reminder: $Q = \sqrt{V_{HOM}}$.

where Q_1 is the indistinguishability parameter on the first two PBSs and Q_2 on the RPBS. If these Q -parameters are set to 1 (perfect indistinguishable), the calculated probability from Tab. 5.1 and Tab. 5.2 are obtained ($\rho = 1/16$). The heralding efficiencies depends on if the photon number is measured. Measuring with non-photon-number-resolving detectors the heralding efficiency is given by

$$P_s = \frac{64Q_1^4Q_2^2}{4Q_1^4Q_2^4 - 4Q_1^4Q_2^2 - Q_1^4 - 40Q_1^3Q_2^2 + 44Q_1^2Q_2^2 - 50Q_1^2 + 151}, \quad (5.15)$$

while photon number resolving detectors yield a heralding efficiency of

$$P_s = \frac{16Q_1^4Q_2^2}{2Q_1^4Q_2^2 - 3Q_1^4 - 2Q_1^2Q_2^2 - 8Q_1^2 + 27}. \quad (5.16)$$

Inserting perfect indistinguishable photons ($Q_n = 1$) yield again the same results as Tab. 5.1 and Tab. 5.2.

Realistic values for the indistinguishability are obtained from [60], since they measured the indistinguishability at 289 ns and 830 ns. This is roughly the time separation of 20 photons ($\tau_{Q_1} = 20 / (76.2 \cdot 10^6) \approx 262$ ns) and 60 photons ($\tau_{Q_2} = 60 / (76.2 \cdot 10^6) \approx 787$ ns) as obtained from the demultiplexed source from Ch. 3. The measured indistinguishability were $V_{HOM,289} = 94.8\%$ and $HOM_{dip,830} = 93.2\%$, which we insert in our calculation for the entanglement gate. The resulting heralding probability and probability to obtain a Bell-state ($P_{\text{Bell}} = \rho_{\Psi_{A,D}^+} + \rho_{\Phi_{A,D}^+}$) are shown in Tab. 5.3 for the case of photon number resolving detectors and non-photon number resolving detectors. The probability to obtain a Bell-state is independent of the heralding detectors since this is the raw probability of obtaining a Bell-state on paths A' and D' . The heralding efficiency is at best $p_S \approx 81\%$ with photon number resolving detectors with the given indistinguishabilities. A setup with non-photon number resolving detectors has a heralding efficiency of $P_S \approx 50\%$.

The next step to analyse is the effect of the limited efficiency of the demultiplexer and the Entanglement gate. We measured the port-to-port transmission efficiency of the entanglement gate between every port, yielding an averaged efficiency of $\eta_{P-P} = 88\%$. Knowing the efficiency of the demultiplexer, we calculated the rate in which we obtain heralding coincidences (F_H), the rate in which we obtain a Bell-state (F_B) and the heralding efficiency depending on the input count

	P_{Bell}	P_s
Non-number resolving	$\approx 5.2\%$	$\approx 50\%$
Number resolving	$\approx 5.2\%$	$\approx 81\%$

Table 5.3: Detection and heralding efficiencies with realistic indistinguishabilities and perfect efficiencies. Heralding is done on either $|H\rangle_B |H\rangle_C$ & $|V\rangle_B |V\rangle_C$ or $|H\rangle_B |V\rangle_C$ & $|V\rangle_B |H\rangle_C$.

rate in the demultiplexer setup. Assuming perfect indistinguishability between the photon, we obtain the estimation shown in Fig. 5.2. The repetition rate of the laser is taken to be $F_{rep} = 76.152$ MHz, as measured in Ch. 3. The expected herald rate depending on the input photon rate of the demultiplexer setup is given in Fig. 5.2 (a) for photon number resolving detectors (magenta line) and non-number resolving detectors (green line). This is the total rate of obtained heralds, including the noise heralds. The top axis shows the effective photon generation rate, which is the input rate divided by the laser repetition rate. The obtained rate of output Bell-states is given in the inset (in MHz), depending on the effective photon generation rate. The heralding efficiency is given in Fig. 5.2 (b) for both the number resolving and the non-number resolving detectors. These graphs show that the best obtainable Bell-state rate $F_B = 0.38$ MHz. The best obtainable heralding efficiencies are $P_S = 24\%$ (non-number resolving detectors) and $P_S = 31\%$ (number resolving detectors) for the current setup efficiencies. If the input source counts is 25 MHz, the heralding efficiency is limited to 1% for both cases. This shows that improvement of the source count rate and the setup transmission efficiencies are required to obtain reasonable heralding efficiencies.

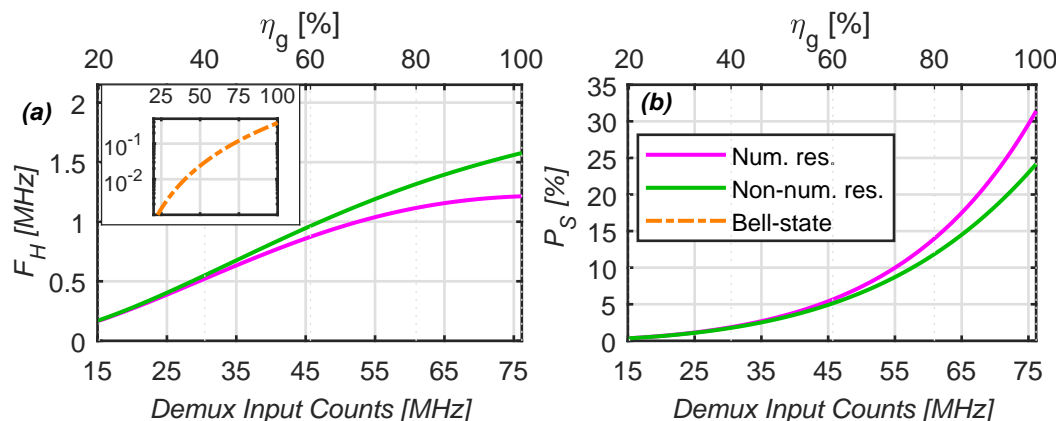


Figure 5.2: Expectation from the heralded entanglement gate assuming pure indistinguishable photons from a source with losses. The source is assumed to be pumped at 76.152 MHz. The demultiplexer efficiencies from Ch. 3 are used together with an effective gate transmission of 88%. (a) Expected herald rate depending on the input count rate of the demultiplexer with number resolving detectors (magenta) and non-number resolving detectors (green). This are all heralds and therefore includes the noise heralds. Top axis shows the effective photon generation probability for the given source rate. Inset shows the rate of Bell-states for the given effective photon generation probability. (b) heralding efficiency depending on the input count rate of the demultiplexer for the same two possible detector configurations.

5.3 Entanglement confirmation

The generated entanglement from the gate has to be confirmed, which can be done via Bell-Measurements and evaluating Bells-inequality [11]. The Bell-inequality was originally proposed to test if an experiment could be described via local hidden variable theory as proposed by Einstein, Podolsky and Rosen (EPR-paradox) [10]. If the Bell-inequality is violated, the outcome cannot be described by local hidden variables and must be quantum. An experimental setup for testing Bell-inequalities is shown in ref [208], where the violation of the *CHSH*-inequality is a measure if the system is quantum. The *CHSH*-inequality is defined with the *S*-parameter. The first experiment to violate the *CHSH*-inequality comes from A. Aspect et al. in the series of papers [12–14]. The *S*-parameter given in [208] can be calculated via [4] (p. 308)

$$S = E(\theta_1, \theta_2) - E(\theta_1, \theta'_2) + E(\theta'_1, \theta_2) + E(\theta'_1, \theta'_2), \quad (5.17)$$

with

$$E(\theta_1, \theta_2) = P_{11}(\theta_1, \theta_2) + P_{00}(\theta_1, \theta_2) - P_{10}(\theta_1, \theta_2) - P_{01}(\theta_1, \theta_2). \quad (5.18)$$

The parameters θ_1 and θ_2 are measurement settings for the two different entangled particles where both side can be in the setting a (θ_1 or θ_2) or setting b (θ'_1 or θ'_2). Since this is a measurement, the parameter P_{ab} is a probability of measuring coincidence ab with the given measurement settings. In case of polarisation entanglement, these parameters are the angle of a waveplate before a PBS with the settings $\theta_1 = 0.0^\circ$ or $\theta'_1 = 45.0^\circ$ $\theta_2 = 22.5^\circ$ or $\theta'_2 = 67.5^\circ$. The detectors 1 and 0 are the detectors in the horizontal and vertical output of the PBS. The Bell-inequality is now written as $-2 \leq S \leq 2$ or $|S| \leq 2$, and the system is quantum if $S > 2$.

5.4 Conclusion

This chapter showed a setup to generate polarisation entangled photons where the problems of probabilistic generation are overcome by heralding. To obtain the highest heralding efficiency, the heralding has to be polarisation and photon-number resolving. This can yield a heralding efficiency of $P_s = 100\%$. If the detectors are not number resolving, the heralding efficiency for a perfect setup is $P_s \approx 62\%$. This chapter also introduced a method to calculate the state evolution for an imperfect setup and imperfect inputs. If the setup is assumed to be perfect but the input photons have a realistic indistinguishability we obtain a heralding efficiency $P_s \approx 81\%$ with number and polarisation resolving detectors. Assuming perfect indistinguishable photons but realistic losses, the heralding efficiency is limited to $P_s \approx 31\%$. The last section introduces a method to analyse if the output state is indeed an entangled state by the methods of the *CHSH*-inequality derived from Bells-inequality.

CH. 6

Time-bin BosonSampler

In quantum information processing, it is assumed that a quantum computer can obtain a calculation speed advantage over classical computers, the so-called quantum advantage. A general design for a quantum computer is the *KLM*-scheme [20] proposed by Knill, Laflamme and Milburn in 2000. This scheme proposes a general quantum computer including overhead for error correction. The resources required for this are however far out of reach with current technologies due to the large number of operations and qubits required to perform single gate operations [21]. The required resources causes this scheme to be unfeasible to prove quantum advantage. An alternative is a specialised quantum computer which is optimised for a single task and can outperform a classical computer for this individual task. This will prove quantum advantage and can be used as a building block for the general quantum computer. A different route to prove quantum advantage is via quantum simulation instead of a quantum computation. Certain Hamiltonians can be simulated by mapping them on the simulator which is faster than simulating or calculating the Hamiltonian on a classical computer. It is shown that a quantum simulator can be made with a passive linear optical network [26, 209–211]. This network consists of a collection of beamsplitters with phase-shifters in between with N number of inputs and outputs. This results in a unitary matrix of N -by- N . When single indistinguishable bosons (e.g. photons) are inserted on the input, the output can be predicted by calculating the permanents of the unitary

matrix. It is shown that calculating permanents is hard for a classical computer [212, 213]. There are however constraints on the unitary matrix before the permanent is classically hard to calculate [214]. This type of quantum simulator is called the BosonSampler.

The first experiments on BosonSampling originate from 2013, which are proof of principle measurements [28–31]. All of these consist of spatial modes interfering through linear optics. The number of elements expands when the number of modes increases. This expansion can be overcome by using time-bin encoding, where the number of interfering elements remains equal [44, 215]. Time-bin BosonSampling requires two nested loops of which one loop (inner loop) interferes consecutive photons by adding a time delay of one time-bin. The second loop is a loop that is larger than the number of time bins, and allows multiple iterations of interference in the inner loop. The switching in and out of the loop can be done via polarisation, where a tunable waveplate before a PBS can select the fraction that will enter the inner loop. The inner loop has two possible configurations, a feedback configuration where a photon can be delayed multiple rounds or a feed forward where a photon can be delayed at maximum one time-bin, as performed in [215]. The feedback loop configuration also has a tunable waveplate before the PBS to determine the fraction that obtains another time-bin of delay.

This chapter introduces a time-bin BosonSampler with an inner loop in the feedback configuration with realistic switching components. The setup will be introduced in Sec. 6.1 followed by the calculation of the unitary matrix in Sec. 6.2.

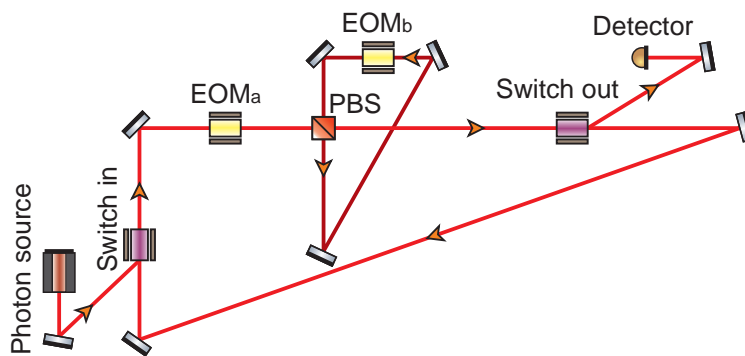


Figure 6.1: BosonSampler setup consisting of two loops with the inner loop in the feedback configuration. Photons are switched into the inner loop via EOM-a and a PBS, and switched out of the inner loop via EOM-b and the same PBS. This configuration allows modes to obtain a delay of more than one time-bin. The photons are switched in and out of the setup via non-polarisation-sensitive switches.

6.1 Time-bin BosonSampling setup

The setup proposed for time-bin BosonSampling is shown in Fig. 6.1 and consists of two loops with EOMs to switch between them. The inner loop has the length necessary to delay a photon by exactly one time-bin, while the outer loop has a length required to delay at least the number of modes while being locked to a desired timing of the EOMs. Single photons generated from a source are switched into the outer loop and make the required circulation in the outer and inner loop to applying the designed unitary evolution. Afterwards they are switched out to a detector with a time tagger to obtain information about the time-bin in which the detection event occurred.

The modes in this setup are not only the time-bins but there is also a polarisation degree of freedom. There exist two orthogonal polarisations per temporal mode, making the total maximum number of modes (M) two times the number of temporal modes (T ; $M = 2T$). Due to these polarisation modes, the switches to

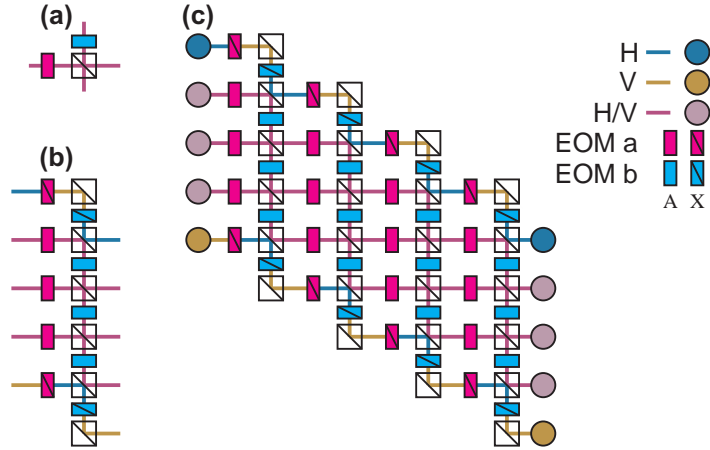


Figure 6.2: Schematic representation of the BosonSampling circuit with five temporal input modes. (a) Single PBS building block, with from the top the input from the inner loop and in blue EOM-b. From the left is the input from the outer loop with EOM-a as the input switch. Concatenating multiple PBS elements yields (b), with five input temporal modes. An EOM with a diagonal line indicates that this EOM is forced to perform an X-operation, which switches horizontal and vertical polarisation. This is required to maintain the number of modes. This block represents one circulation around the outer loop where photons can circulate in the inner loop for multiple rounds. Concatenating multiple circulations around the large loop result in schematic (c) which is a full time-bin BosonSampling run. The colour of the lines represents the allowed polarisation modes for the illustrated temporal mode and the circles represent the input and output modes.

switch photons in and out of the interfering setup have to be polarisation insensitive.

The switching of EOM-a and EOM-b determines how all the modes mix with each other as schematically represented in Fig. 6.2. Part (a) shows the basic building block of the BosonSampler, a single switch. This shows the PBS in the setup with two inputs and outputs. The left input is from the outer loop where the splitting ratio into the delay loop and the polarisation mixing is done with EOM-a. The inner loop enters from the top where EOM-b mixes the two polarisations, determining the splitting ratio of exiting and remaining in the inner loop. A single circulation around the outer loop yields Fig. 6.2 (b), which is a concatenation of multiple inner loop circulations. The colour of the temporal modes represents which polarisation modes are allowed for that temporal mode. A diagonal line through an EOM indicates that the operation is fixed to be crossed (switching horizontal and vertical polarisation). All other EOM settings are allowed to be arbitrary. The first and last temporal mode have a boundary on the allowed polarisation to ensure that the total number of modes remains constant and therefore

$$M = 2(T - 1) \quad (6.1)$$

is the actual number of modes in the system. Concatenating multiple circulations around the outer loop results in a schematic of Fig. 6.2 (c) which is also the total operation of the setup to mix all modes. This shows that for T number of temporal modes, a total of $T - 1$ circulations around the outer loop with T circulations in the inner loop (per outer loop circulation) are required to interfere all modes. A used assumption for the schematic is that the horizontal polarisation is transmitted by a PBS, but this is a matter of convention and does not alter the operation of the time-bin BosonSampler.

6.2 Calculating the unitary operation

The next step is to calculate the unitary evolution of the BosonSampler. This can be done by analysing the unitary matrix for every individual circulation around the outer loop. This matrix can be written as

$$\bar{U}^{(L)} = \begin{bmatrix} U_{p=1,q=1}^{(L)} & \cdots & U_{p=1,q=M}^{(L)} \\ \vdots & \ddots & \vdots \\ U_{p=M,q=1}^{(L)} & \cdots & U_{p=M,q=M}^{(L)} \end{bmatrix} \quad (6.2)$$

where index q denotes the input mode number, index p the output mode number and the superscript (L) is the circulation iteration in the outer loop. The total unitary evolution can then be written as

$$\bar{U} = \prod_{\kappa=1}^{T-1} \bar{U}^{(T-\kappa)}. \quad (6.3)$$

Calculating the unitary operation

time-bin number T	1	2	2	3	3	4	4	5
mode number m	1	2	3	4	5	6	7	8
Mode configuration	$ H_1\rangle$	$ V_2\rangle$	$ H_2\rangle$	$ V_3\rangle$	$ H_3\rangle$	$ V_4\rangle$	$ H_4\rangle$	$ V_5\rangle$

Table 6.1: Assigning mode indices to temporal and polarisation modes. The index in the mode configuration denotes in which time-bin that polarisation mode resides.

This is effectively multiplying all individual matrices via left handed multiplication. The next step is to assign mode indices to the different states, which is done in Tab. 6.1 for $T = 5$. The numbering is done in order of time-bin where every time-bin has two consecutive mode numbers for the two polarisation modes. The polarisation is numbered with first the vertical and than the horizontal polarisation. All the horizontal polarisations are an odd-numbered mode while the vertical polarisations are even-numbered. Using Fig. 6.2 (b) together with the mode assignment of Tab. 6.1 and the physical operation, the unitary evolution of a single outer loop circulation can be written out as

$$\bar{U}^{(L)} = \begin{bmatrix} 0 & U_{1,2}^{(L)} & U_{1,3}^{(L)} & 0 & 0 & 0 & 0 & 0 \\ U_{2,1}^{(L)} & U_{2,2}^{(L)} & U_{2,3}^{(L)} & 0 & 0 & 0 & 0 & 0 \\ 0 & 0 & 0 & U_{3,4}^{(L)} & U_{3,5}^{(L)} & 0 & 0 & 0 \\ U_{4,1}^{(L)} & U_{4,2}^{(L)} & U_{4,3}^{(L)} & U_{4,4}^{(L)} & U_{4,5}^{(L)} & 0 & 0 & 0 \\ 0 & 0 & 0 & 0 & 0 & U_{5,6}^{(L)} & U_{5,7}^{(L)} & 0 \\ U_{6,1}^{(L)} & U_{6,2}^{(L)} & U_{6,3}^{(L)} & U_{6,4}^{(L)} & U_{6,5}^{(L)} & U_{6,6}^{(L)} & U_{6,7}^{(L)} & 0 \\ 0 & 0 & 0 & 0 & 0 & 0 & 0 & U_{7,8}^{(L)} \\ U_{8,1}^{(L)} & U_{8,2}^{(L)} & U_{8,3}^{(L)} & U_{8,4}^{(L)} & U_{8,5}^{(L)} & U_{8,6}^{(L)} & U_{8,7}^{(L)} & U_{8,8}^{(L)} \end{bmatrix}. \quad (6.4)$$

All the zero elements in the matrix occur from physical limitations due to the orientation and transmission and reflection properties of the PBS. This shows that the vertical output modes have more contributing input modes than the horizontal output modes. This can be explained since a vertical output mode comes from circulation through the inner loop while horizontal output modes come from modes not entering the inner loop.

To calculate all the matrix elements, the building block from Fig. 6.2 (a) has to be applied $T + 1$ times. Indication of the time instance can be done with the same indication as the input time-bin from the large loop. From Fig. 6.2 (b) it can then be seen that the index t runs from 1 to $T + 1$. Every building block from Fig. 6.2 (a) consists of a polarisation mixing EOMs inserted in both input arms of the

PBS. The individual EOMs have a transfer function of

$$\bar{\bar{E}}_{a,t}^{(L)} = \begin{bmatrix} E_{a,t}^{vv,(L)} & E_{a,t}^{hv,(L)} \\ E_{a,t}^{vh,(L)} & E_{a,t}^{hh,(L)} \end{bmatrix} \quad (6.5)$$

$$\bar{\bar{E}}_{b,t}^{(L)} = \begin{bmatrix} E_{b,t}^{vv,(L)} & E_{b,t}^{hv,(L)} \\ E_{b,t}^{vh,(L)} & E_{b,t}^{hh,(L)} \end{bmatrix} \quad (6.6)$$

where h and v in the superscripts denote from which to which polarisation the transfer is executed. The PBS is defined to transmit the horizontal polarisation without any phase shift while the vertical polarisation is reflected with a $\pi/2$ phase shift. The constraint to maintain an equal number of modes shows that the elementwise absolute value of

$$\bar{\bar{E}}_{a,1}^{(L)} = \bar{\bar{E}}_{a,T}^{(L)} = \bar{\bar{E}}_{b,2}^{(L)} = \bar{\bar{E}}_{b,T+1}^{(L)} = \begin{bmatrix} 0 & 1 \\ 1 & 0 \end{bmatrix} \quad (6.7)$$

and that $\bar{\bar{E}}_{a,T+1}^{(L)}$ and $\bar{\bar{E}}_{b,1}^{(L)}$ are not used. The matrix elements from Eq. 6.7 can still have a phase shift which is different for every element.

Knowing the building block of the temporal BosonSampler, the unitary matrix can be calculated. The elements which are zeros in $\bar{\bar{U}}^{(L)}$ are already known and only the non-zero elements will be addressed via different equations. The first condition is when p is odd, so the output mode number is odd (horizontal output modes), yielding

$$\begin{aligned} U_{p,q}^{(L)} &= U_{p,p+1}^{(L)} = E_{a, \lfloor \frac{p+3}{2} \rfloor}^{vh,(L)} \\ U_{p,q}^{(L)} &= U_{p,p+2}^{(L)} = E_{a, \lfloor \frac{p+3}{2} \rfloor}^{hh,(L)} \end{aligned} \quad (6.8)$$

The other condition is when p is even which corresponds to the vertical output modes. These have to be separated on going through the inner loop for a single circulation ($q = p$ and $q = p + 1$) or for multiple circulations ($q < p$). For a single circulation in the inner loop, this yields

$$\begin{aligned} U_{p,q}^{(L)} &= U_{p,p}^{(L)} = E_{a, \lfloor \frac{p+2}{2} \rfloor}^{vv,(L)} E_{b, \lfloor \frac{p+4}{2} \rfloor}^{vv,(L)} e^{i\pi} \\ U_{p,q}^{(L)} &= U_{p,p+1}^{(L)} = E_{a, \lfloor \frac{p+2}{2} \rfloor}^{hv,(L)} E_{b, \lfloor \frac{p+4}{2} \rfloor}^{vv,(L)} e^{i\pi} \end{aligned} \quad (6.9)$$

while multiple circulations yield

$$U_{p,q}^{(L)} = E_{a, \lfloor \frac{q+1}{2} \rfloor}^{hv,(L)} E_{b, \lfloor \frac{q+3}{2} \rfloor}^{vh,(L)} E_{b, \lfloor \frac{p+4}{2} \rfloor}^{hv,(L)} e^{i\pi} \prod_{w=\frac{q+5}{2}}^{\frac{p+2}{2}} E_{b, [w]}^{hh,(L)} \quad (6.10)$$

when q is odd and

$$U_{p,q}^{(L)} = E_{a, \lfloor \frac{q+2}{2} \rfloor}^{hv, (L)} E_{b, \lfloor \frac{q+4}{2} \rfloor}^{vh, (L)} E_{b, \lfloor \frac{p+4}{2} \rfloor}^{hv, (L)} e^{i\pi} \prod_{w=\frac{q+6}{2}}^{\frac{p+2}{2}} E_{b, [w]}^{hh, (L)} \quad (6.11)$$

when q is even. [†]

The initial constraint of a non-expanding number of modes resulted in constraints on the EOM operations. If this is used in the above given equations, it results in $U_{M,M}^{(L)} = 0$ and $U_{M-1,M}^{(L)} = 1$. Knowing how to calculate the unitary matrix, the physical devices can be inserted in the calculation. Highly efficient EOMs are currently not yet able to generate completely arbitrary pulses. As discussed in Chap. 3, electrical broadband EOMs are limited at a repetition rate of 1 MHz. Resonant EOMs are capable of faster switching but oscillate at only one electrical frequency. Since the idea is to switch different photons with a different ratio, the resonant EOMs are preferred since the electrical broadband EOM performs the same rotation to multiple consecutive photons.

The designed EOM configuration for the setup in Fig. 6.1 consists of a quarter wave EOM (EOM-1) and a half wave EOM (EOM-2) in the outer loop and having only a half wave EOM (EOM-3) in the inner loop. This design yields $E_a = E_1 E_2$ and $E_b = E_3$ with

$$\begin{aligned} E_1 &= \frac{1}{\sqrt{2}} \begin{bmatrix} 1 - i \cos(2\theta_{1,t}) & i \sin(2\theta_{1,t}) \\ i \sin(2\theta_{1,t}) & 1 + i \cos(2\theta_{1,t}) \end{bmatrix} \\ E_2 &= i \begin{bmatrix} -\cos(2\theta_{2,t}) & \sin(2\theta_{2,t}) \\ \sin(2\theta_{2,t}) & \cos(2\theta_{2,t}) \end{bmatrix} \\ E_3 &= i \begin{bmatrix} -\cos(2\theta_{3,t}) & \sin(2\theta_{3,t}) \\ \sin(2\theta_{3,t}) & \cos(2\theta_{3,t}) \end{bmatrix}, \end{aligned} \quad (6.12)$$

resulting in

$$\begin{aligned} E_a &= \frac{1}{\sqrt{2}} \begin{bmatrix} -i \cos(2\theta_{2,t}) - \cos(2(\theta_{1,t} - \theta_{2,t})) & i \sin(2\theta_{2,t}) + \sin(2(\theta_{1,t} - \theta_{2,t})) \\ i \sin(2\theta_{2,t}) + \sin(2(\theta_{1,t} - \theta_{2,t})) & +i \cos(2\theta_{2,t}) - \cos(2(\theta_{1,t} - \theta_{2,t})) \end{bmatrix} \\ E_b &= i \begin{bmatrix} -\cos(2\theta_{3,t}) & \sin(2\theta_{3,t}) \\ \sin(2\theta_{3,t}) & \cos(2\theta_{3,t}) \end{bmatrix}, \end{aligned} \quad (6.13)$$

where θ is the angle between the waveplate axes and the polarisation axes.

Inserting the constraints of the resonant EOMs to maintain the number of modes is done by setting up the equations for $\theta_{1,t}$, $\theta_{2,t}$ and $\theta_{3,t}$.

[†] $\prod_{\epsilon}^{\leq \epsilon} = 1$

A solution to the constraints comes in the form of

$$\begin{aligned}
 \theta_{1,t} &= \frac{\pi}{4} \frac{A_1}{2} \left[1 - \cos \left(2\pi I_1 \frac{t-1}{T-1} \right) \right] \\
 \theta_{2,t} &= \frac{\pi}{4} \left(1 - \frac{A_2}{2} \left[1 - \cos \left(2\pi I_2 \frac{t-1}{T-1} \right) \right] \right) \\
 \theta_{3,t} &= \frac{\pi}{4} \left(1 - \frac{A_3}{2} \left[1 - \cos \left(2\pi I_3 \frac{t-1}{T-1} \right) \right] \right)
 \end{aligned} \tag{6.14}$$

where A and I are free parameters and A indicates the effective angle range between the waveplate axes and the polarisation axes ($0 \leq A \leq 1$) and I is an integer indicating the number of oscillations within one circulation. This shows that the complete unitary matrix is defined by only 6 free parameters. It is yet unknown if this is sufficient to obtain a hard random matrix or if the structure in the matrix allows classical computer to efficiently calculate the permanents of the matrix.

Knowing the unitary matrix, the total efficiency of the setup should be calculated focusing on the probability to obtain an n -fold coincidence at the detectors when n -number of photons are inserted into the BosonSampler. This calculation uses the assumption that $n \ll M$ so there are no two photons in the same mode at the output. The challenge in this calculation is to calculate the efficiency around the inner loop since the efficiency depends on the number of circulation the photon makes in the inner loop. The other elements are trivial since every photon has an input efficiency (η_{in}), an output efficiency (η_{out}) and $T-2$ occurrences of the outer loop efficiency (η_{LL}^{T-2}).

Estimating the efficiency for all the circulations around the inner loop require some estimations, making the output an approximation. To obtain the exact efficiency, all losses must be taken into account in the unitary matrix which is then extended with loss modes.

The used approximation is that every input photon is equally distributed over the output modes it can reach. This yields an average efficiency per photon for the inner loop circulations of

$$\eta_{\text{ILA}} = \left(\sum_{k=2}^T \frac{\eta_{\text{IL}}^k}{T-1} + 2 \cdot \sum_{t=2}^{T-1} \left(\sum_{k=0}^{T-t+1} \frac{\eta_{\text{IL}}^k}{T-t+2} \right) + 1 \right) \frac{1}{M}, \tag{6.15}$$

Where η_{IL} is the efficiency of the inner loop. The first and last term in the brackets are the summations for the first and last time bin mode, and the central part are for all time-bin modes that contain two polarisations. The factor $1/M$ at the end is the normalisation to the number of modes. We now calculate the average probability to obtain an n -fold coincidence of

$$P_{\text{n-fold}} = \left(\eta_{\text{ILA}}^{T-1} \eta_{\text{LL}}^{T-2} \eta_{\text{out}} \eta_{\text{in}} \right)^n. \tag{6.16}$$

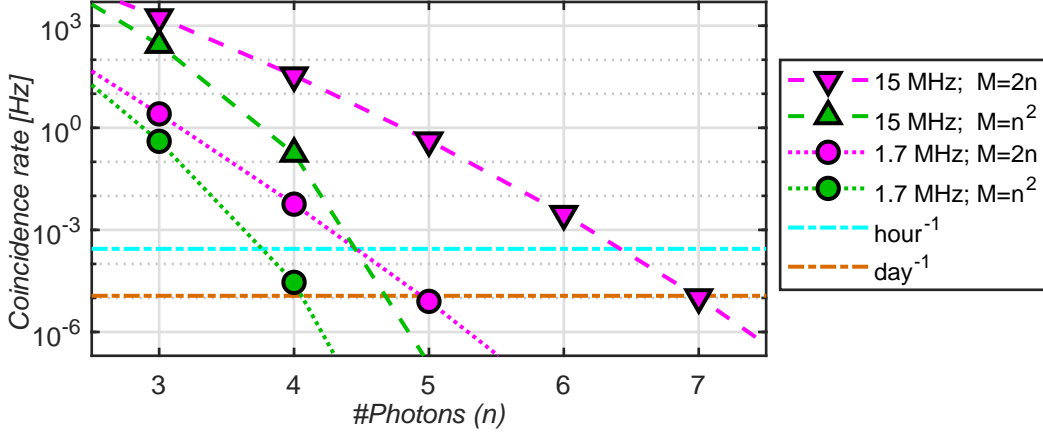


Figure 6.3: Expectations in measured n -fold coincidence rate for the BosonSampler with realistic efficiencies. The magenta points shows the expectation when $M = 2n$ and the green points when $M = n^2$. Both modal expansions are calculated when the input photon rate $F_{in} = 1.7$ MHz and $F_{in} = 15$ MHz. The blue dot-dashed line marks a rate of 1 detected n -fold coincidence per hour and the orange dot-dashed line indicate 1 detected n -fold coincidence per day. The lines connecting the calculated n -fold coincidences are a guide to the eye.

The predictions for n -fold coincidence rates allows us to calculate the expected rates for different number of input photons. First we have to yield realistic values for the variables in Eq. 6.16. The input laser has a repetition rate of 76.152 MHz. The switches to switch in and out are assumed to have an efficiency of 85% when switching and 100% when not switching. These only affect η_{in} and η_{out} for that reason. Other effects on η_{in} and η_{out} are the source efficiency (η_{in}) and the detector efficiency (η_{out}), of which the source efficiency is used as a free variable and the detector efficiency is $\eta_{det} = 88\%$. The inner loop is only influenced by the switch in the inner loop, which we assume $\eta_{sw} = 97\%$ (see Ch. 3). The outer loop has two of these switches, a fibre coupler and a fibre to delay the light. The fibre is assumed to have a loss of $3.5\text{dB}/\text{km}$ (Fibre type: 780HP), and the length is based on the number of modes. When an sampling experiment is ongoing, no new photons can enter the setup for a next sampling experiment. The effective repetition rate is therefore reduced by the number of modes squared [27, 44, 190]. The last variable that has to be set is the number of modes. There are two common conventions for the required number of modes for a BosonSampler, which are $M = 2n$ and $M = n^2$. We calculate the expected coincidence rates depending on the number of photons with both conventions. We do this for two different source efficiencies, with an input photon rate $F_{in} = 1.7$ MHz and $F_{in} = 15$ MHz. The results are plotted in Fig. 6.3 where the magenta points indicate $M = 2n$ and the green points indicate $M = n^2$. The circles indicate $F_{in} = 1.7$ MHz and the triangles indicate $F_{in} = 15$ MHz. The lines are a guide to the eye to trace the different

efficiencies. The dot-dashed lines indicate a sample rate of 1 per hour (blue) and 1 per day (orange). This shows that the source from Ch. 3 ($F_{in} = 1.7 \text{ MHz}$) can perform a BosonSampling experiment with at max 4 photons, independent of the scaling for the number of modes. Increasing the input rate to 15 MHz enables a BosonSampling experiment with a maximum of 7 photon when $M = 2n$.

6.3 Conclusion

This chapter proposed a design for a temporal BosonSampler configured with a feedback delay loop allowing a mode to be delayed by more than one time-bin. An equivalent beamsplitter network is constructed for analogies to the original passive component model. This model was used to formulate constraints on the mixing to ensure a constant number of modes.

The unitary matrix of the system is calculated which can be split in matrices for every individual circulation around the outer delay loop. It is shown that the minimum number of required circulation around the large delay loop is $T - 1$ with T being the number of temporal modes. This architecture allows the temporal modes to contain two polarisation modes, except for the first and last temporal mode. The calculation also shows in which way realistic switching elements can be implemented and gave an example with a total of 6 free parameters to tune the unitary matrix. The next step is to calculate if the possible unitaries are hard random matrices, which are required to show quantum advantage.

The last part consisted of efficiency approximations to estimate how efficient the sampling can be performed. This shows that the total output probability scales exponentially with the number of input photons and exponentially with the number of circulations around the outer loop. Using a source with the same efficiency as in Ch. 3 (1.7 MHz) would result in a maximum BosonSampling experiment with 4 photons to yield a count rate of more than one per day. Increasing the source count rate to 15 MHz would yield a maximum BosonSampling experiment with 7 photons. This assumes we take a number of modes that is twice the number of photons.

This method of BosonSampling is promising due to the limited number of devices, but the delay lines can limit the efficiency for larger number of photons. Free space BosonSampling has traditionally the advantage of higher efficiencies compared to on-chip BosonSampling. This advantage was negated by [57], introducing a structure with the efficiency advantage of free space BosonSampling at the size of an on-chip BosonSampler. This yield a time-bin BosonSampling architecture obsolete due to the larger scale and larger losses.

Conclusion and outlook

In this thesis we presented work towards applications of quantum dot single photon sources. Different properties of the single photons and the single photon sources are discussed and compared to the current state of the art. We studied the single photon purity and photon indistinguishability together with the photon generation rate, and how they affect the operation of different optical circuits.

The main focus of this thesis is on quantum dot single photon sources and their applications. We performed investigations on the effect of the width of a nanobeam waveguide on the embedded quantum dot. The differences and similarities of this effect on the X_0 and X^- excitons were analysed. The measurements indicate that the Stark parameter changes with the waveguide width. Further we observed that the transmission dip visibility reduced when the linewidths increased, indicating that the broadening is due to noise. The measurements also showed that the X_0 is typically more susceptible to noise than the X^- , and that the Stark parameter is larger for the X_0 than for the X^- . This indicates that the noise is induced by charges around the quantum dot. Measurements on the coupling between a quantum dot and a photonic crystal waveguide showed a Purcell enhancement of the radiative decay rate when the exciton resonance is electrically tuned across the bandedge. The measured linewidths were however broadened due to the noise and could not supplement the lifetime measurements.

Photons generated from a quantum dot source were demultiplexed in space with a temporal-to-spatial mode converter. The input source count rate in the demultiplexing setup was 1.7 MHz, resulting in a detected four fold coincidence rate of $F_{4F} = 1.05 \pm 0.05$ Hz. The quantum dot is pumped at a repetition rate of 76.152 MHz, thus a thorough analysis of the source efficiency was carried out. This allowed the identification of the limiting factors in the source efficiency. Increasing the source efficiency to obtain an input count rate to 25.6 MHz would result in a detected four fold coincidence rate of $F_{4F} \approx 38$ kHz. Comparing the demultiplexer to other work via our models shows that our demultiplexer is the most efficient demultiplexer yet.

The generated four photon states by the demultiplexer can be utilised to generate polarisation entangled photon pairs. This can be done with a heralded entanglement gate, where two photons are used as a herald for a polarisation entangled photon pair. We set up a model to analyse the entanglement gate for realistic photon properties. We calculated the heralding efficiency in a case of pure single photons, no losses but with a realistic indistinguishability. This showed that the maximum achievable heralding efficiency with state of the art indistinguishability reaches $P_S \approx 81\%$ with photon-number resolving detectors. A heralding efficiency of $P_S \approx 62\%$ is reached with non photon-number resolving detectors.

In the last chapter we analysed a time-bin BosonSampler with an inner loop in the feed-back configuration. A switching scheme to preserve the number of modes is presented and we analysed the unitary evolution in this configuration. The effect of realistic switches are introduced and we made an estimation of the M-fold coincidence rates after the BosonSampler.

Outlook

The spectral properties of quantum dots embedded in nano-photonic structures benefit from deterministic fabrication of nano-structures around the quantum dot. This allows a better in-depth analysis of the effect of the nanobeam waveguide width. A more in-depth investigation of the noise can clarify if the increased amount of noise measured on the X_0 is due to the larger Stark-parameter. The photonic crystal waveguides benefit from deterministic fabrication since the quantum dot can be located where the β -factor is the largest.

The demultiplexing setup can be upgraded to an 8-mode converter by adding an extra EOM. Using this with a single photon source that can give 17 MHz of photons at the input of the demultiplexer will result in a 1 Hz of 8-fold coincidences. This can be used to operate two entanglements gates, yielding the heralding of two entangled photon pairs. This allows proof of principle measurements for device independent QKD. Utilisation of a single heralded entanglement gate can be done with a quantum random number generator.

Bibliography

- [1] M. Planck, “Ueber das Gesetz der Energieverteilung im Normalspectrum,” *Annalen der Physik*, vol. 309, no. 3, pp. 553–563, 1901.
- [2] A. Einstein, “Über einen die Erzeugung und Verwandlung des Lichtes betreffenden heuristischen Gesichtspunkt,” *Annalen der Physik*, vol. 322, no. 6, pp. 132–148, 1905.
- [3] A. B. Arons and M. B. Peppard, “Einstein’s Proposal of the Photon Concept—a Translation of the Annalen der Physik Paper of 1905,” *American Journal of Physics*, vol. 33, no. 5, pp. 367–374, 1965.
- [4] A. M. Fox, *Quantum Optics*. Oxford: Oxford University Press, 2014.
- [5] N. Bohr, “I. On the constitution of atoms and molecules,” *The London, Edinburgh, and Dublin Philosophical Magazine and Journal of Science*, vol. 26, no. 151, pp. 1–25, 1913.
- [6] W. Heisenberg, “Über quantentheoretische Umdeutung kinematischer und mechanischer Beziehungen.,” *Zeitschrift für Physik*, vol. 33, no. 1, pp. 879–893, 1925.
- [7] E. Schrödinger, “Quantisierung als Eigenwertproblem,” *Annalen der Physik*, vol. 385, no. 13, pp. 437–490, 1926.
- [8] D. J. Griffiths, *Introduction to Quantum Mechanics*. Reed: Pearson Prentice Hall, 2 ed., 2005.
- [9] M. Born, “Zur Quantenmechanik der Stoßvorgänge,” *Zeitschrift für Physik*, vol. 37, no. 12, pp. 863–867, 1926.
- [10] A. Einstein, B. Podolsky, and N. Rosen, “Can Quantum-Mechanical Description of Physical Reality Be Considered Complete?,” *Physical Review*, vol. 47, no. 10, pp. 777–780, 1935.
- [11] J. S. Bell, “On the Einstein Podolsky Rosen paradox,” *Physics Physique Fizika*, vol. 1, no. 3, pp. 195–200, 1964.
- [12] A. Aspect, P. Grangier, and G. Roger, “Experimental Tests of Realistic Local Theories via Bell’s Theorem,” *Physical Review Letters*, vol. 47, no. 7, pp. 460–463, 1981.
- [13] A. Aspect, J. Dalibard, and G. Roger, “Experimental Test of Bell’s Inequalities Using Time-Varying Analyzers,” *Phys. Rev. Lett.*, vol. 49, no. 25,

BIBLIOGRAPHY

- pp. 1804—1807, 1982.
- [14] A. Aspect, P. Grangier, and G. Roger, “Experimental Realization of Einstein-Podolsky-Rosen-Bohm Gedankenexperiment : A New Violation of Bell’s Inequalities,” *Physical Review Letters*, vol. 49, no. 2, pp. 91–94, 1982.
 - [15] D. Deutsch and R. Jozsa, “Rapid Solution of Problems by Quantum Computation,” *Proceedings of the Royal Society A: Mathematical, Physical and Engineering Sciences*, vol. 439, no. 1907, pp. 553–558, 1992.
 - [16] P. Shor, “Algorithms for quantum computation: discrete logarithms and factoring,” in *Proceedings 35th Annual Symposium on Foundations of Computer Science*, pp. 124–134, IEEE Comput. Soc. Press, 2002.
 - [17] L. K. Grover, “A fast quantum mechanical algorithm for database search,” in *Proceedings of the twenty-eighth annual ACM symposium on Theory of computing - STOC '96*, (New York, USA), pp. 212–219, ACM Press, 1996.
 - [18] L. K. Grover, “From Schrödinger’s equation to the quantum search algorithm,” *American Journal of Physics*, vol. 69, no. 7, pp. 769–777, 2001.
 - [19] A. W. Harrow, A. Hassidim, and S. Lloyd, “Quantum Algorithm for Linear Systems of Equations,” *Physical Review Letters*, vol. 103, no. 15, p. 150502, 2009.
 - [20] E. Knill, R. Laflamme, and G. J. Milburn, “A scheme for efficient quantum computation with linear optics,” *Nature*, vol. 409, no. 6816, pp. 46–52, 2001.
 - [21] T. C. Ralph, A. J. F. Hayes, and A. Gilchrist, “Loss-Tolerant Optical Qubits,” *Physical Review Letters*, vol. 95, no. 10, p. 100501, 2005.
 - [22] U. C. Singh and P. A. Kollman, “A combined ab initio quantum mechanical and molecular mechanical method for carrying out simulations on complex molecular systems: Applications to the CH₃Cl + Cl[?] exchange reaction and gas phase protonation of polyethers,” *Journal of Computational Chemistry*, vol. 7, no. 6, pp. 718–730, 1986.
 - [23] R. Kosloff, “Time-dependent quantum-mechanical methods for molecular dynamics,” *The Journal of Physical Chemistry*, vol. 92, no. 8, pp. 2087–2100, 1988.
 - [24] M. J. Field, P. A. Bash, and M. Karplus, “A combined quantum mechanical and molecular mechanical potential for molecular dynamics simulations,” *Journal of Computational Chemistry*, vol. 11, no. 6, pp. 700–733, 1990.
 - [25] A. Aspuru-Guzik, “Simulated Quantum Computation of Molecular Energies,” *Science*, vol. 309, no. 5741, pp. 1704–1707, 2005.
 - [26] M. Reck, A. Zeilinger, H. J. Bernstein, and P. Bertani, “Experimental realization of any discrete unitary operator,” *Physical Review Letters*, vol. 73, no. 1, pp. 58–61, 1994.
 - [27] B. T. Gard, K. R. Motes, J. P. Olson, P. P. Rohde, and J. P. Dowling, “An Introduction to Boson-Sampling,” in *From Atomic to Mesoscale*, pp. 167–192, WORLD SCIENTIFIC, 2015.
 - [28] M. A. Broome, A. Fedrizzi, S. Rahimi-Keshari, J. Dove, S. Aaronson, T. C. Ralph, and A. G. White, “Photonic Boson Sampling in a Tunable Circuit,” *Science*, vol. 339, no. 6121, pp. 794–798, 2013.

BIBLIOGRAPHY

- [29] A. Crespi, R. Osellame, R. Ramponi, D. J. Brod, E. F. Galvão, N. Spagnolo, C. Vitelli, E. Maiorino, P. Mataloni, and F. Sciarrino, “Integrated multi-mode interferometers with arbitrary designs for photonic boson sampling,” *Nature Photonics*, vol. 7, no. 7, pp. 545–549, 2013.
- [30] M. Tillmann, B. Dakić, R. Heilmann, S. Nolte, A. Szameit, and P. Walther, “Experimental boson sampling,” *Nature Photonics*, vol. 7, no. 7, pp. 540–544, 2013.
- [31] J. B. Spring, B. J. Metcalf, P. C. Humphreys, W. S. Kolthammer, X.-M. Jin, M. Barbieri, A. Datta, N. Thomas-Peter, N. K. Langford, D. Kundys, J. C. Gates, B. J. Smith, P. G. R. Smith, and I. A. Walmsley, “Boson Sampling on a Photonic Chip,” *Science*, vol. 339, no. 6121, pp. 798–801, 2013.
- [32] C. H. Bennet and G. Brassard, “Quantum cryptography: Public key distribution and coin tossing,” in *Proceedings of IEEE International Conference on Computers, Systems and Signal Processing*, p. 8, 1984.
- [33] A. K. Ekert, “Quantum cryptography based on Bell’s theorem,” *Physical Review Letters*, vol. 67, no. 6, pp. 661–663, 1991.
- [34] V. Scarani, H. Bechmann-Pasquinucci, N. J. Cerf, M. Dušek, N. Lütkenhaus, and M. Peev, “The security of practical quantum key distribution,” *Reviews of Modern Physics*, vol. 81, no. 3, pp. 1301–1350, 2009.
- [35] E. Diamanti, H.-K. Lo, B. Qi, and Z. Yuan, “Practical challenges in quantum key distribution,” *npj Quantum Information*, vol. 2, no. 1, p. 16025, 2016.
- [36] N. T. Islam, C. C. W. Lim, C. Cahall, J. Kim, and D. J. Gauthier, “Provably secure and high-rate quantum key distribution with time-bin qudits,” *Science Advances*, vol. 3, no. 11, p. e1701491, 2017.
- [37] F.-G. Deng, G. L. Long, and X.-S. Liu, “Two-step quantum direct communication protocol using the Einstein-Podolsky-Rosen pair block,” *Physical Review A*, vol. 68, no. 4, p. 042317, 2003.
- [38] G. L. Long and X. S. Liu, “Theoretically efficient high-capacity quantum-key-distribution scheme,” *Physical Review A*, vol. 65, no. 3, p. 032302, 2002.
- [39] C. H. Bennett, G. Brassard, and S. Breidbart, “Quantum Cryptography II: How to re-use a one-time pad safely even if $P=NP$,” *Natural Computing*, vol. 13, no. 4, pp. 453–458, 2014.
- [40] M. Hillery, V. Bužek, and A. Berthiaume, “Quantum secret sharing,” *Physical Review A*, vol. 59, no. 3, pp. 1829–1834, 1999.
- [41] A. Aspuru-Guzik and P. Walther, “Photonic quantum simulators,” *Nature Physics*, vol. 8, no. 4, pp. 285–291, 2012.
- [42] C. Sparrow, E. Martín-López, N. Maraviglia, A. Neville, C. Harrold, J. Carolan, Y. N. Joglekar, T. Hashimoto, N. Matsuda, J. L. O’Brien, D. P. Tew, and A. Laing, “Simulating the vibrational quantum dynamics of molecules using photonics,” *Nature*, vol. 557, no. 7707, pp. 660–667, 2018.
- [43] N. Sangouard and H. Zbinden, “What are single photons good for?,” *Journal of Modern Optics*, vol. 59, no. 17, pp. 1458–1464, 2012.
- [44] K. R. Motes, A. Gilchrist, J. P. Dowling, and P. P. Rohde, “Scalable Boson

BIBLIOGRAPHY

- Sampling with Time-Bin Encoding Using a Loop-Based Architecture,” *Physical Review Letters*, vol. 113, no. 12, p. 120501, 2014.
- [45] P. Lodahl, “Quantum-dot based photonic quantum networks,” *Quantum Science and Technology*, vol. 3, no. 1, 2018.
- [46] F. Kaneda and P. G. Kwiat, “High-efficiency single-photon generation via large-scale active time multiplexing.”, *arXiv:1803.04803v1* (2018).
- [47] C. Xiong, X. Zhang, Z. Liu, M. J. Collins, A. Mahendra, L. G. Helt, M. J. Steel, D. Y. Choi, C. J. Chae, P. H. W. Leong, and B. J. Eggleton, “Active temporal multiplexing of indistinguishable heralded single photons,” *Nature Communications*, vol. 7, no. 1, p. 10853, 2016.
- [48] T. Rudolph, “Why I am optimistic about the silicon-photonics route to quantum computing,” *APL Photonics*, vol. 2, no. 3, p. 030901, 2017.
- [49] A. V. Kuhlmann, J. H. Prechtel, J. Houel, A. Ludwig, D. Reuter, A. D. Wieck, and R. J. Warburton, “Transform-limited single photons from a single quantum dot,” *Nature Communications*, vol. 6, no. 1, p. 8204, 2015.
- [50] P. Lodahl, S. Mahmoodian, and S. Stobbe, “Interfacing single photons and single quantum dots with photonic nanostructures,” *Reviews of Modern Physics*, vol. 87, no. 2, pp. 347–400, 2015.
- [51] I. Aharonovich, D. Englund, and M. Toth, “Solid-state single-photon emitters,” *Nature Photonics*, vol. 10, no. 10, pp. 631–641, 2016.
- [52] M. Arcari, I. Söllner, A. Javadi, S. Lindskov Hansen, S. Mahmoodian, J. Liu, H. Thyrrstrup, E. H. Lee, J. D. Song, S. Stobbe, and P. Lodahl, “Near-Unity Coupling Efficiency of a Quantum Emitter to a Photonic Crystal Waveguide,” *Physical Review Letters*, vol. 113, no. 9, p. 093603, 2014.
- [53] T. Huber, A. Predojević, D. Föger, G. Solomon, and G. Weihs, “Optimal excitation conditions for indistinguishable photons from quantum dots,” *New Journal of Physics*, vol. 17, no. 12, p. 123025, 2015.
- [54] X. Ding, Y. He, Z.-C. Duan, N. Gregersen, M.-C. Chen, S. Unsleber, S. Maier, C. Schneider, M. Kamp, S. Höfling, C.-Y. Lu, and J.-W. Pan, “On-Demand Single Photons with High Extraction Efficiency and Near-Unity Indistinguishability from a Resonantly Driven Quantum Dot in a Micropillar,” *Physical Review Letters*, vol. 116, no. 2, p. 020401, 2016.
- [55] P. Senellart, G. Solomon, and A. White, “High-performance semiconductor quantum-dot single-photon sources,” *Nature Nanotechnology*, vol. 12, no. 11, pp. 1026–1039, 2017.
- [56] J. P. Lee, A. J. Bennett, R. M. Stevenson, D. J. P. Ellis, I. Farrer, D. A. Ritchie, and A. J. Shields, “Multi-dimensional photonic states from a quantum dot,” *Quantum Science and Technology*, vol. 3, no. 2, p. 024008, 2018.
- [57] H. Wang, Y. He, Y. H. Li, Z. E. Su, B. Li, H. L. Huang, X. Ding, M. C. Chen, C. Liu, J. Qin, J. P. Li, Y. M. He, C. Schneider, M. Kamp, C. Z. Peng, S. Höfling, C. Y. Lu, and J. W. Pan, “High-efficiency multiphoton boson sampling,” *Nature Photonics*, vol. 11, no. 6, pp. 361–365, 2017.
- [58] F. Lenzini, B. Haylock, J. C. Loredó, R. A. Abrahão, N. A. Zakaria, S. Kature, I. Sagnes, A. Lemaitre, H. P. Phan, D. V. Dao, P. Senellart, M. P.

BIBLIOGRAPHY

- Almeida, A. G. White, and M. Lobino, “Active demultiplexing of single photons from a solid-state source,” *Laser and Photonics Reviews*, vol. 11, no. 3, p. 1600297, 2017.
- [59] T. Hummel, C. Ouellet-Plamondon, E. Ugur, I. Kulkova, T. Lund-Hansen, M. A. Broome, R. Uppu, and P. Lodahl, “Efficient demultiplexed single-photon source with a quantum dot coupled to a nanophotonic waveguide,” *arXiv:1903.08785* (2019), 2019.
- [60] H. Wang, Z.-C. Duan, Y.-H. Li, S. Chen, J.-P. Li, Y.-M. He, M.-C. Chen, Y. He, X. Ding, C.-Z. Peng, C. Schneider, M. Kamp, S. Höfling, C.-Y. Lu, and J.-W. Pan, “Near-Transform-Limited Single Photons from an Efficient Solid-State Quantum Emitter,” *Physical Review Letters*, vol. 116, no. 21, p. 213601, 2016.
- [61] I. A. Walmsley, “Quantum optics: Science and technology in a new light,” *Science*, vol. 348, no. 6234, pp. 525–530, 2015.
- [62] J. Borregaard, A. S. Sørensen, and P. Lodahl, “Quantum Networks with Deterministic Spin–Photon Interfaces,” *Advanced Quantum Technologies*, vol. 1800091, p. 1800091, 2019.
- [63] NobelPrize.org, “The Nobel Prize in Physics 2000.” , <https://www.nobelprize.org/prizes/physics/2000/summary/>, accessed 2019-03-28.
- [64] P. Y. Yu and M. Cardona, *Fundamentals of Semiconductors*. Graduate Texts in Physics, Berlin, Heidelberg: Springer Berlin Heidelberg, 4th ed., 2010.
- [65] C. K. Chiang, C. R. Fincher, Y. W. Park, A. J. Heeger, H. Shirakawa, E. J. Louis, S. C. Gau, and A. G. MacDiarmid, “Electrical Conductivity in Doped Polyacetylene,” *Physical Review Letters*, vol. 39, no. 17, pp. 1098–1101, 1977.
- [66] S. M. Sze, *Semiconductor Devices: Physics and Technology*. Wiley, 2 ed., 2002.
- [67] B. H. Bransden and C. Joachain, *Quantum Mechanics*. Prentice Hall, 2nd ed., 2000.
- [68] P. Kuiper, “File:Isolator-metal.svg [Online].” , <https://commons.wikimedia.org/wiki/File:Isolator-metal.svg>, accessed 2019-03-05, 2007.
- [69] M. C. Löbl, I. Söllner, A. Javadi, T. Pregolato, R. Schott, L. Midolo, A. V. Kuhlmann, S. Stobbe, A. D. Wieck, P. Lodahl, A. Ludwig, and R. J. Warburton, “Narrow optical linewidths and spin pumping on charge-tunable close-to-surface self-assembled quantum dots in an ultrathin diode,” *Physical Review B*, vol. 96, no. 16, p. 165440, 2017.
- [70] A. M. Fox, *Optical properties of solids*. Oxford: Oxford University Press, second ed., 2010.
- [71] C. Kittel, *Introduction to solid state physics Charles Kittel*. New York: Wiley, seventh ed., 1996.
- [72] R. S. Daveau, *Efficient fiber-coupled single-photon sources based on quantum dots*. Ph.D thesis, University of Copenhagen, 2016.
- [73] S. L. Hansen, *Single-Photon Manipulation in Nanophotonic Circuits*. Ph.D

BIBLIOGRAPHY

- thesis, University of Copenhagen, 2017.
- [74] G. Kiršanské, *Electrical control of excitons in semiconductor nanostructures*. Ph.D thesis, University of Copenhagen, 2016.
 - [75] J. A. Venables, *Introduction to Surface and Thin Film Processes*. Cambridge: Cambridge University Press, 2000.
 - [76] D. Leonard, K. Pond, and P. M. Petroff, “Critical layer thickness for self-assembled InAs islands on GaAs,” *Physical Review B*, vol. 50, no. 16, pp. 11687–11692, 1994.
 - [77] R. J. Warburton, C. Schulhauser, D. Haft, C. Schäfflein, K. Karrai, J. M. Garcia, W. Schoenfeld, and P. M. Petroff, “Giant permanent dipole moments of excitons in semiconductor nanostructures,” *Physical Review B*, vol. 65, no. 11, p. 113303, 2002.
 - [78] B. Alén, F. Bickel, K. Karrai, R. J. Warburton, and P. M. Petroff, “Stark-shift modulation absorption spectroscopy of single quantum dots,” *Applied Physics Letters*, vol. 83, no. 11, pp. 2235–2237, 2003.
 - [79] M. Hauck, F. Seilmeier, S. E. Beavan, A. Badolato, P. M. Petroff, and A. Högele, “Locating environmental charge impurities with confluent laser spectroscopy of multiple quantum dots,” *Physical Review B*, vol. 90, no. 23, p. 235306, 2014.
 - [80] L. F. Zagonel, S. Mazzucco, M. Tencé, K. March, R. Bernard, B. Laslier, G. Jacopin, M. Tchernycheva, L. Rigutti, F. H. Julien, R. Songmuang, and M. Kociak, “Nanometer Scale Spectral Imaging of Quantum Emitters in Nanowires and Its Correlation to Their Atomically Resolved Structure,” *Nano Letters*, vol. 11, no. 2, pp. 568–573, 2011.
 - [81] J. Y. Duboz, E. Costard, E. Rosencher, P. Bois, J. Nagle, J. M. Berset, D. Jaroszynski, and J. M. Ortega, “Electron relaxation time measurements in GaAs/AlGaAs quantum wells: Intersubband absorption saturation by a free-electron laser,” *Journal of Applied Physics*, vol. 77, no. 12, pp. 6492–6495, 1995.
 - [82] S. Sauvage, P. Boucaud, F. Glotin, R. Prazeres, J.-M. Ortega, A. Lemaître, J.-M. Gérard, and V. Thierry-Flieg, “Saturation of intraband absorption and electron relaxation time in n -doped InAs/GaAs self-assembled quantum dots,” *Applied Physics Letters*, vol. 73, no. 26, pp. 3818–3821, 1998.
 - [83] T. Müller, F. F. Schrey, G. Strasser, and K. Unterrainer, “Ultrafast intraband spectroscopy of electron capture and relaxation in InAs/GaAs quantum dots,” *Applied Physics Letters*, vol. 83, no. 17, pp. 3572–3574, 2003.
 - [84] S. Tomić, “Intermediate-band solar cells: Influence of band formation on dynamical processes in InAs/GaAs quantum dot arrays,” *Physical Review B*, vol. 82, no. 19, p. 195321, 2010.
 - [85] D. Mogilevtsev, A. P. Nisovtsev, S. Kilin, S. B. Cavalcanti, H. S. Brandi, and L. E. Oliveira, “Driving-Dependent Damping of Rabi Oscillations in Two-Level Semiconductor Systems,” *Physical Review Letters*, vol. 100, no. 1, p. 017401, 2008.
 - [86] Y.-M. He, Y. He, Y.-J. Wei, D. Wu, M. Atatüre, C. Schneider, S. Höfling,

BIBLIOGRAPHY

- M. Kamp, C.-Y. Lu, and J.-W. Pan, “On-demand semiconductor single-photon source with near-unity indistinguishability,” *Nature Nanotechnology*, vol. 8, no. 3, pp. 213–217, 2013.
- [87] J. M. Gérard and B. Gayral, “Strong Purcell effect for InAs quantum boxes in three-dimensional solid-state microcavities,” *Journal of Lightwave Technology*, vol. 17, no. 11, pp. 2089–2095, 1999.
- [88] A. B. Young, A. C. Thijssen, D. M. Beggs, P. Androvitsaneas, L. Kuipers, J. G. Rarity, S. Hughes, and R. Oulton, “Polarization Engineering in Photonic Crystal Waveguides for Spin-Photon Entanglers,” *Physical Review Letters*, vol. 115, no. 15, p. 153901, 2015.
- [89] L. Novotny and B. Hecht, *Principles of Nano-Optics*. Cambridge: Cambridge University Press, 2006.
- [90] J. Vučković, D. Fattal, C. Santori, G. S. Solomon, and Y. Yamamoto, “Enhanced single-photon emission from a quantum dot in a micropost microcavity,” *Applied Physics Letters*, vol. 82, no. 21, pp. 3596–3598, 2003.
- [91] J. N. Farahani, D. W. Pohl, H. J. Eisler, and B. Hecht, “Single quantum dot coupled to a scanning optical antenna: A tunable superemitter,” *Physical Review Letters*, vol. 95, no. 1, p. 017402, 2005.
- [92] M. Gschrey, F. Gericke, A. Schüßler, R. Schmidt, J. H. Schulze, T. Heindel, S. Rodt, A. Strittmatter, and S. Reitzenstein, “In situ electron-beam lithography of deterministic single-quantum-dot mesa-structures using low-temperature cathodoluminescence spectroscopy,” *Applied Physics Letters*, vol. 102, no. 25, 2013.
- [93] M. Gschrey, A. Thoma, P. Schnauber, M. Seifried, R. Schmidt, B. Wohlfeil, L. Krüger, J. H. Schulze, T. Heindel, S. Burger, F. Schmidt, A. Strittmatter, S. Rodt, and S. Reitzenstein, “Highly indistinguishable photons from deterministic quantum-dot microlenses utilizing three-dimensional in situ electron-beam lithography,” *Nature Communications*, vol. 6, no. 1, p. 7662, 2015.
- [94] A. Thoma, P. Schnauber, M. Gschrey, M. Seifried, J. Wolters, J. H. Schulze, A. Strittmatter, S. Rodt, A. Carmele, A. Knorr, T. Heindel, and S. Reitzenstein, “Exploring Dephasing of a Solid-State Quantum Emitter via Time- and Temperature-Dependent Hong-Ou-Mandel Experiments,” *Physical Review Letters*, vol. 116, no. 3, p. 033601, 2016.
- [95] G. Kiršanskė, H. Thyrrerstrup, R. S. Daveau, C. L. Dreeßen, T. Pregnolato, L. Midolo, P. Tighineanu, A. Javadi, S. Stobbe, R. Schott, A. Ludwig, A. D. Wieck, S. I. Park, J. D. Song, A. V. Kuhlmann, I. Söllner, M. C. Löbl, R. J. Warburton, and P. Lodahl, “Indistinguishable and efficient single photons from a quantum dot in a planar nanobeam waveguide,” *Physical Review B*, vol. 96, no. 16, p. 165306, 2017.
- [96] P. Lodahl, A. F. Van Driel, I. S. Nikolaev, A. Irman, K. Overgaag, D. Vanmaekelbergh, and W. L. Vos, “Controlling the dynamics of spontaneous emission from quantum dots by photonic crystals,” *Nature*, vol. 430, no. 7000, pp. 654–657, 2004.

BIBLIOGRAPHY

- [97] V. S. C. M. Rao and S. Hughes, “Single Quantum Dot Spontaneous Emission in a Finite-Size Photonic Crystal Waveguide: Proposal for an Efficient “On Chip” Single Photon Gun,” *Physical Review Letters*, vol. 99, no. 19, p. 193901, 2007.
- [98] I. Farrer, G. A. C. Jones, S. Kalliakos, D. A. Ritchie, A. J. Shields, A. Schwagmann, and J. P. Griffiths, “On-chip single photon emission from an integrated semiconductor quantum dot into a photonic crystal waveguide,” *Applied Physics Letters*, vol. 99, no. 26, p. 261108, 2011.
- [99] S. L. Hansen, L. Midolo, P. Lodahl, H. El-Ella, I. Söllner, T. Pregolato, A. Javadi, E. H. Lee, S. Mahmoodian, G. Kiršanskė, S. Stobbe, and J. D. Song, “Deterministic photon–emitter coupling in chiral photonic circuits,” *Nature Nanotechnology*, vol. 10, no. 9, pp. 775–778, 2015.
- [100] S. Kalliakos, Y. Brody, A. J. Bennett, D. J. Ellis, J. Skiba-Szymanska, I. Farrer, J. P. Griffiths, D. A. Ritchie, and A. J. Shields, “Enhanced indistinguishability of in-plane single photons by resonance fluorescence on an integrated quantum dot,” *Applied Physics Letters*, vol. 109, no. 15, 2016.
- [101] P. Lodahl, S. Mahmoodian, S. Stobbe, A. Rauschenbeutel, P. Schneeweiss, J. Volz, H. Pichler, and P. Zoller, “Chiral quantum optics,” *Nature*, vol. 541, no. 7638, pp. 473–480, 2017.
- [102] H. Thyrestrup, G. Kiršanskė, H. Le Jeannic, T. Pregolato, L. Zhai, L. Raahauge, L. Midolo, N. Rotenberg, A. Javadi, R. Schott, A. D. Wieck, A. Ludwig, M. C. Löbl, I. Söllner, R. J. Warburton, and P. Lodahl, “Quantum Optics with Near-Lifetime-Limited Quantum-Dot Transitions in a Nanophotonic Waveguide,” *Nano Letters*, vol. 18, no. 3, pp. 1801–1806, 2018.
- [103] M. Boroditsky, R. Vrijen, T. Krauss, R. Coccioli, R. Bhat, and E. Yablonovitch, “Spontaneous emission extraction and Purcell enhancement from thin-film 2-D photonic crystals,” *Journal of Lightwave Technology*, vol. 17, no. 11, pp. 2096–2112, 1999.
- [104] Phezack, “File:Optical Microresonator.png.” , https://commons.wikimedia.org/wiki/File:Optical_Microresonator.png, accessed 2019-04-05, 2017.
- [105] T. Müller, S. Fölling, A. Widera, and I. Bloch, “State Preparation and Dynamics of Ultracold Atoms in Higher Lattice Orbitals,” *Physical Review Letters*, vol. 99, no. 20, p. 200405, 2007.
- [106] S. Ates, S. M. Ulrich, S. Reitzenstein, A. Löffler, A. Forchel, and P. Michler, “Post-Selected Indistinguishable Photons from the Resonance Fluorescence of a Single Quantum Dot in a Microcavity,” *Physical Review Letters*, vol. 103, no. 16, p. 167402, 2009.
- [107] H. S. Nguyen, G. Sallen, C. Voisin, P. Roussignol, C. Diederichs, and G. Cassabois, “Ultra-coherent single photon source,” *Applied Physics Letters*, vol. 99, no. 26, p. 261904, 2011.
- [108] T. Jakubczyk, W. Pacuski, T. Smoleński, A. Golnik, M. Florian, F. Jahnke, C. Kruse, D. Hommel, and P. Kossacki, “Pronounced Purcell enhancement

BIBLIOGRAPHY

- of spontaneous emission in CdTe/ZnTe quantum dots embedded in micropillar cavities,” *Applied Physics Letters*, vol. 101, no. 13, p. 132105, 2012.
- [109] N. Somaschi, V. Giesz, L. De Santis, J. C. Loredó, M. P. Almeida, G. Hornecker, S. L. Portalupi, T. Grange, C. Antón, J. Demory, C. Gómez, I. Sagnes, N. D. Lanzillotti-Kimura, A. Lemaître, A. Auffèves, A. G. White, L. Lanco, and P. Senellart, “Near-optimal single-photon sources in the solid state,” *Nature Photonics*, vol. 10, no. 5, pp. 340–345, 2016.
- [110] D. Gammon, E. S. Snow, B. V. Shanabrook, D. S. Katzer, and D. Park, “Fine Structure Splitting in the Optical Spectra of Single GaAs Quantum Dots,” *Physical Review Letters*, vol. 76, no. 16, pp. 3005–3008, 1996.
- [111] M. Ghali, Y. Ohno, and H. Ohno, “Vertical electric field induced suppression of fine structure splitting of excited state excitons in a single GaAs/AlGaAs island quantum dots,” *Applied Physics Letters*, vol. 107, no. 12, p. 123102, 2015.
- [112] C. Robert, T. Amand, F. Cadiz, D. Lagarde, E. Courtade, M. Manca, T. Taniguchi, K. Watanabe, B. Urbaszek, and X. Marie, “Fine structure and lifetime of dark excitons in transition metal dichalcogenide monolayers,” *Physical Review B*, vol. 96, no. 15, p. 155423, 2017.
- [113] P. Klenovský, P. Steindl, J. Aberl, E. Zallo, R. Trotta, A. Rastelli, and T. Fromherz, “Effect of second-order piezoelectricity on the excitonic structure of stress-tuned In(Ga)As/GaAs quantum dots,” *Physical Review B*, vol. 97, no. 24, p. 245314, 2018.
- [114] A. Müller, E. B. Flagg, P. Bianucci, X. Y. Wang, D. G. Deppe, W. Ma, J. Zhang, G. J. Salamo, M. Xiao, and C. K. Shih, “Resonance Fluorescence from a Coherently Driven Semiconductor Quantum Dot in a Cavity,” *Physical Review Letters*, vol. 99, no. 18, p. 187402, 2007.
- [115] E. B. Flagg, A. Müller, J. W. Robertson, S. Founta, D. G. Deppe, M. Xiao, W. Ma, G. J. Salamo, and C. K. Shih, “Resonantly driven coherent oscillations in a solid-state quantum emitter,” *Nature Physics*, vol. 5, no. 3, pp. 203–207, 2009.
- [116] A. Auffèves-Garnier, C. Simon, J.-M. Gérard, and J.-P. Poizat, “Giant optical nonlinearity induced by a single two-level system interacting with a cavity in the Purcell regime,” *Physical Review A*, vol. 75, no. 5, p. 053823, 2007.
- [117] I.-C. Hoi, T. Palomaki, J. Lindkvist, G. Johansson, P. Delsing, and C. M. Wilson, “Generation of Nonclassical Microwave States Using an Artificial Atom in 1D Open Space,” *Physical Review Letters*, vol. 108, no. 26, p. 263601, 2012.
- [118] T. G. Tiecke, J. D. Thompson, N. P. de Leon, L. R. Liu, V. Vuletić, and M. D. Lukin, “Nanophotonic quantum phase switch with a single atom,” *Nature*, vol. 508, no. 7495, pp. 241–244, 2014.
- [119] A. Javadi, I. Söllner, M. Arcari, S. L. Hansen, L. Midolo, S. Mahmoodian, G. Kiršanskė, T. Pregnolato, E. H. Lee, J. D. Song, S. Stobbe, and P. Lodahl, “Single-photon non-linear optics with a quantum dot in a waveguide,”

BIBLIOGRAPHY

- Nature Communications*, vol. 6, no. 1, p. 8655, 2015.
- [120] G. Reithmaier, M. Kaniber, F. Flassig, S. Lichtmannecker, K. Müller, A. Andrejew, J. Vučković, R. Gross, and J. J. Finley, “On-Chip Generation, Routing, and Detection of Resonance Fluorescence,” *Nano Letters*, vol. 15, no. 8, pp. 5208–5213, 2015.
- [121] J. Wang, A. Santamato, P. Jiang, D. Bonneau, E. Engin, J. W. Silverstone, M. Lermer, J. Beetz, M. Kamp, S. Höfling, M. G. Tanner, C. M. Natarajan, R. H. Hadfield, S. N. Dorenbos, V. Zwiller, J. L. O’Brien, and M. G. Thompson, “Gallium arsenide (GaAs) quantum photonic waveguide circuits,” *Optics Communications*, vol. 327, pp. 49–55, 2014.
- [122] P. E. Barclay, K. Srinivasan, M. Borselli, and O. Painter, “Efficient input and output fiber coupling to a photonic crystal waveguide,” *Optics Letters*, vol. 29, no. 7, pp. 697–699, 2004.
- [123] S. Gröblacher, J. T. Hill, A. H. Safavi-Naeini, J. Chan, and O. Painter, “Highly efficient coupling from an optical fiber to a nanoscale silicon optomechanical cavity,” *Applied Physics Letters*, vol. 103, no. 18, p. 181104, 2013.
- [124] B. D. Hauer, P. H. Kim, C. Doolin, A. J. MacDonald, H. Ramp, and J. P. Davis, “On-chip cavity optomechanical coupling,” *EPJ Techniques and Instrumentation*, vol. 1, no. 1, p. 4, 2014.
- [125] J. E. Hoffman, S. Ravets, J. A. Grover, P. Solano, P. R. Kordell, J. D. Wong-Campos, L. A. Orozco, and S. L. Rolston, “Ultrahigh transmission optical nanofibers,” *AIP Advances*, vol. 4, no. 6, p. 067124, 2014.
- [126] T. G. Tiecke, K. P. Nayak, J. D. Thompson, T. Peyronel, N. P. de Leon, V. Vuletić, and M. D. Lukin, “Efficient fiber-optical interface for nanophotonic devices,” *Optica*, vol. 2, no. 2, p. 70, 2015.
- [127] R. S. Daveau, K. C. Balram, T. Pregnolato, J. Liu, E. H. Lee, J. D. Song, V. Verma, R. Mirin, S. W. Nam, L. Midolo, S. Stobbe, K. Srinivasan, and P. Lodahl, “Efficient fiber-coupled single-photon source based on quantum dots in a photonic-crystal waveguide,” *Optica*, vol. 4, no. 2, p. 178, 2017.
- [128] Q. V. Tran, S. Combríe, P. Colman, and A. De Rossi, “Photonic crystal membrane waveguides with low insertion losses,” *Applied Physics Letters*, vol. 95, no. 6, p. 061105, 2009.
- [129] A. Faraon, I. Fushman, D. Englund, N. Stoltz, P. Petroff, and J. Vučković, “Coherent generation of non-classical light on a chip via photon-induced tunnelling and blockade,” *Nature Physics*, vol. 4, no. 11, pp. 859–863, 2008.
- [130] N. A. Wasley, A. M. Fox, A. C. T. Thijssen, M. Hugues, I. J. Luxmoore, R. Oulton, M. S. Skolnick, and A. J. Ramsay, “Optical control of the emission direction of a quantum dot,” *Applied Physics Letters*, vol. 103, no. 24, p. 241102, 2013.
- [131] R. J. Coles, D. M. Price, J. E. Dixon, B. Royall, E. Clarke, P. Kok, M. S. Skolnick, A. M. Fox, and M. N. Makhonin, “Chirality of nanophotonic waveguide with embedded quantum emitter for unidirectional spin transfer,” *Nature Communications*, vol. 7, no. 1, p. 11183, 2016.

BIBLIOGRAPHY

- [132] X. Zhou, I. Kulkova, T. Lund-Hansen, S. L. Hansen, P. Lodahl, and L. Midolo, “High-efficiency shallow-etched grating on GaAs membranes for quantum photonic applications,” *Applied Physics Letters*, vol. 113, no. 25, p. 251103, 2018.
- [133] B. Lounis and M. Orrit, “Single-photon sources,” *Reports on Progress in Physics*, vol. 68, no. 5, pp. 1129–1179, 2005.
- [134] J. Řeháček, Z. Hradil, O. Haderka, J. Peřina, and M. Hamar, “Multiple-photon resolving fiber-loop detector,” *Physical Review A*, vol. 67, no. 6, p. 061801, 2003.
- [135] D. Rosenberg, A. Lita, A. Miller, and S. Nam, “Noise-free high-efficiency photon-number-resolving detectors,” *Physical Review A*, vol. 71, no. 6, p. 061803, 2005.
- [136] B. Calkins, P. L. Mennea, A. E. Lita, B. J. Metcalf, W. S. Kolthammer, A. Lamas-Linares, J. B. Spring, P. C. Humphreys, R. P. Mirin, J. C. Gates, P. G. R. Smith, I. A. Walmsley, T. Gerrits, and S. W. Nam, “High quantum-efficiency photon-number-resolving detector for photonic on-chip information processing,” *Optics Express*, vol. 21, no. 19, p. 22657, 2013.
- [137] A. Eckstein, *Mastering quantum light pulses with nonlinear waveguide interactions*. Ph.D thesis, Universität Erlangen-Nürnberg, 2012.
- [138] S. Rand, *Lectures on Light*. Oxford University Press, first ed., 2010.
- [139] R. Loudon, *The Quantum Theory of Light*. Oxford: Oxford University Press, third ed., 2000.
- [140] D. A. Steck, “Quantum and Atom Optics.”, available online at <http://steck.us/teaching> (revision 0.12.6,23 April 2019).
- [141] R. W. Boyd, *Nonlinear Optics*. Elsevier Science & Technology, 3 ed., 2008.
- [142] B. E. A. Saleh and M. C. Teich, *Fundamentals of Photonics*. Wiley Series in Pure and Applied Optics, New York, USA: John Wiley & Sons, Inc., second ed., 2007.
- [143] P. Kok, W. J. Munro, K. Nemoto, T. C. Ralph, J. P. Dowling, and G. J. Milburn, “Linear optical quantum computing with photonic qubits,” *Reviews of Modern Physics*, vol. 79, no. 1, pp. 135–174, 2007.
- [144] J. Carolan, J. D. Meinecke, P. J. Shadbolt, N. J. Russell, N. Ismail, K. Wörhoff, T. Rudolph, M. G. Thompson, J. L. O’Brien, J. C. Matthews, and A. Laing, “On the experimental verification of quantum complexity in linear optics,” *Nature Photonics*, vol. 8, no. 8, pp. 621–626, 2014.
- [145] H. Dale, D. Jennings, and T. Rudolph, “Provable quantum advantage in randomness processing,” *Nature Communications*, vol. 6, no. 1, p. 8203, 2015.
- [146] F. Flamini, N. Spagnolo, and F. Sciarrino, “Photonic quantum information processing: a review,” *Reports on Progress in Physics*, vol. 82, no. 1, p. 016001, 2019.
- [147] M. Herrero-Collantes and J. C. Garcia-Escartin, “Quantum random number generators,” *Reviews of Modern Physics*, vol. 89, no. 1, p. 015004, 2017.
- [148] R. Arnon-Friedman, F. Dupuis, O. Fawzi, R. Renner, and T. Vidick, “Prac-

BIBLIOGRAPHY

- tical device-independent quantum cryptography via entropy accumulation,” *Nature Communications*, vol. 9, no. 1, p. 459, 2018.
- [149] Y. Liu, X. Yuan, M.-H. Li, W. Zhang, Q. Zhao, J. Zhong, Y. Cao, Y.-H. Li, L.-K. Chen, H. Li, T. Peng, Y.-A. Chen, C.-Z. Peng, S.-C. Shi, Z. Wang, L. You, X. Ma, J. Fan, Q. Zhang, and J.-W. Pan, “High-Speed Device-Independent Quantum Random Number Generation without a Detection Loophole,” *Physical Review Letters*, vol. 120, no. 1, p. 010503, 2018.
- [150] M. Davanço, C. S. Hellberg, S. Ates, A. Badolato, and K. Srinivasan, “Multiple time scale blinking in InAs quantum dot single-photon sources,” *Physical Review B*, vol. 89, no. 16, p. 161303, 2014.
- [151] J. Johansen, B. Julsgaard, S. Stobbe, J. M. Hvam, and P. Lodahl, “Probing long-lived dark excitons in self-assembled quantum dots,” *Physical Review B - Condensed Matter and Materials Physics*, vol. 81, no. 8, p. 081304, 2010.
- [152] A. Javadi, S. Mahmoodian, I. Söllner, and P. Lodahl, “Numerical modeling of the coupling efficiency of single quantum emitters in photonic-crystal waveguides,” *Journal of the Optical Society of America B*, vol. 35, no. 3, p. 514, 2018.
- [153] S. Boixo, S. V. Isakov, V. N. Smelyanskiy, R. Babbush, N. Ding, Z. Jiang, M. J. Bremner, J. M. Martinis, and H. Neven, “Characterizing quantum supremacy in near-term devices,” *Nature Physics*, vol. 14, no. 6, pp. 595–600, 2018.
- [154] A. M. Dalzell, A. W. Harrow, D. E. Koh, and R. L. La Placa, “How many qubits are needed for quantum computational supremacy?,” *arXiv:1805.05224v2* (2018).
- [155] C. Papon, X. Zhou, H. Thyrestrup, Z. Liu, S. Stobbe, R. Schott, A. D. Wieck, A. Ludwig, P. Lodahl, and L. Midolo, “Nanomechanical single-photon routing,” *Optica*, vol. 6, no. 4, p. 524, 2019.
- [156] J. Marquez, L. Geelhaar, and K. Jacobi, “Atomically resolved structure of InAs quantum dots,” *Applied Physics Letters*, vol. 78, no. 16, pp. 2309–2311, 2001.
- [157] M. T. Todaro, M. Catalano, J. X. Chen, R. Cingolani, J. F. Carlin, J. Katcki, M. Ilegems, A. Fiore, R. P. Stanley, J. Ratajczak, E. Piscopiello, L. Nasi, A. Markus, U. Oesterle, L. Lazzarini, and R. Houdré, “Tuning InAs/GaAs quantum dot properties under Stranski-Krastanov growth mode for 1.3 μm applications,” *Journal of Applied Physics*, vol. 91, no. 10, p. 6710, 2002.
- [158] R. J. Warburton, “Single spins in self-assembled quantum dots,” *Nature Materials*, vol. 12, no. 6, pp. 483–493, 2013.
- [159] D. Pinotsi, P. Fallahi, J. Miguel-Sanchez, and A. Imamoglu, “Resonant spectroscopy on charge tunable quantum dots in photonic crystal structures,” *IEEE Journal of Quantum Electronics*, vol. 47, no. 11, pp. 1371–1374, 2011.
- [160] K. G. Lagoudakis, K. Fischer, T. Sarmiento, A. Majumdar, A. Rundquist, J. Lu, M. Bajcsy, and J. Vučković, “Deterministically charged quantum dots in photonic crystal nanoresonators for efficient spin-photon interfaces,” *New*

BIBLIOGRAPHY

- Journal of Physics*, vol. 15, p. 113056, 2013.
- [161] A. L. Efros and M. Rosen, “Random Telegraph Signal in the Photoluminescence Intensity of a Single Quantum Dot,” *Physical Review Letters*, vol. 78, no. 6, pp. 1110–1113, 1997.
 - [162] M. Lippitz, F. Kulzer, and M. Orrit, “Statistical Evaluation of Single Nano-Object Fluorescence,” *ChemPhysChem*, vol. 6, no. 5, pp. 770–789, 2005.
 - [163] A. V. Kuhlmann, J. Houel, A. Ludwig, L. Greuter, D. Reuter, A. D. Wieck, M. Poggio, and R. J. Warburton, “Charge noise and spin noise in a semiconductor quantum device,” *Nature Physics*, vol. 9, no. 9, pp. 570–575, 2013.
 - [164] S. Mahmoodian, K. Prindal-Nielsen, I. Söllner, S. Stobbe, and P. Lodahl, “Engineering chiral light–matter interaction in photonic crystal waveguides with slow light,” *Optical Materials Express*, vol. 7, no. 1, p. 43, 2017.
 - [165] J. Liu, M. I. Davanço, L. Sapienza, K. Konthasinghe, J. V. De Miranda Cardoso, J. D. Song, A. Badolato, and K. Srinivasan, “Cryogenic photoluminescence imaging system for nanoscale positioning of single quantum emitters,” *Review of Scientific Instruments*, vol. 88, no. 2, p. 023116, 2017.
 - [166] T. Pregolato, *In preperation*. Ph.D thesis, University of Copenhagen, 2019.
 - [167] A. A. Asatryan, K. Busch, R. C. McPhedran, L. C. Botten, C. M. de Sterke, and N. A. Nicorovici, “Two-dimensional Green tensor and local density of states in finite-sized two-dimensional photonic crystals,” *Waves in Random Media*, vol. 13, no. 1, pp. 9–25, 2003.
 - [168] B. Krummheuer, V. M. Axt, and T. Kuhn, “Theory of pure dephasing and the resulting absorption line shape in semiconductor quantum dots,” *Physical Review B*, vol. 65, no. 19, p. 195313, 2002.
 - [169] T. Suzuki, R. Singh, G. Moody, M. Aßmann, M. Bayer, A. Ludwig, A. D. Wieck, and S. T. Cundiff, “Dephasing of InAs quantum dot p-shell excitons studied using two-dimensional coherent spectroscopy,” *Physical Review B*, vol. 98, no. 19, p. 195304, 2018.
 - [170] J. Boutari, A. Feizpour, S. Barz, C. D. Franco, M. S. Kim, W. S. Kolthammer, and I. A. Walmsley, “Large scale quantum walks by means of optical fiber cavities,” *Journal of Optics*, vol. 18, no. 9, p. 094007, 2016.
 - [171] A. Christ, K. Laiho, A. Eckstein, K. N. Cassemiro, and C. Silberhorn, “Probing multimode squeezing with correlation functions,” *New Journal of Physics*, vol. 13, p. 033027, 2011.
 - [172] H. Le Jeannic, *Optical Hybrid Quantum Information Processing*. Ph.D thesis, Université pierre et marie curie, 2016.
 - [173] K. A. Fischer, L. Hanschke, J. Wierzbowski, T. Simmet, C. Dory, J. J. Finley, J. Vučković, and K. Müller, “Signatures of two-photon pulses from a quantum two-level system,” *Nature Physics*, vol. 13, no. 7, pp. 649–654, 2017.
 - [174] P. Tighineanu, C. L. Dreeßen, C. Flindt, P. Lodahl, and A. S. Sørensen, “Phonon Decoherence of Quantum Dots in Photonic Structures: Broadening of the Zero-Phonon Line and the Role of Dimensionality,” *Physical Review Letters*, vol. 120, no. 25, p. 257401, 2018.

BIBLIOGRAPHY

- [175] H.-S. Zhong, Y. Li, W. Li, L.-C. Peng, Z.-E. Su, Y. Hu, Y.-M. He, X. Ding, W. Zhang, H. Li, L. Zhang, Z. Wang, L. You, X.-L. Wang, X. Jiang, L. Li, Y.-A. Chen, N.-L. Liu, C.-Y. Lu, and J.-W. Pan, “12-Photon Entanglement and Scalable Scattershot Boson Sampling with Optimal Entangled-Photon Pairs from Parametric Down-Conversion,” *Physical Review Letters*, vol. 121, no. 25, p. 250505, 2018.
- [176] F. Sciarrino, R. Osellame, A. Crespi, E. F. Galvão, F. Flamini, M. Bentivegna, R. Ramponi, L. Latmiral, C. Vitelli, N. Spagnolo, P. Mataloni, N. Viggianiello, and D. J. Brod, “Experimental scattershot boson sampling,” *Science Advances*, vol. 1, no. 3, p. e1400255, 2015.
- [177] L. Latmiral, N. Spagnolo, and F. Sciarrino, “Towards quantum supremacy with lossy scattershot boson sampling,” *New Journal of Physics*, vol. 18, no. 11, p. 113008, 2016.
- [178] J. J. Renema, A. Menssen, W. R. Clements, G. Triginer, W. S. Kolthammer, and I. A. Walmsley, “Efficient Classical Algorithm for Boson Sampling with Partially Distinguishable Photons,” *Physical Review Letters*, vol. 120, no. 22, p. 220502, 2018.
- [179] J. Joo, P. L. Knight, J. L. O’Brien, and T. Rudolph, “One-way quantum computation with four-dimensional photonic qudits,” *Physical Review A - Atomic, Molecular, and Optical Physics*, vol. 76, no. 5, p. 052326, 2007.
- [180] T. Jennewein, M. Barbieri, and A. G. White, “Single-photon device requirements for operating linear optics quantum computing outside the post-selection basis,” *Journal of Modern Optics*, vol. 58, no. 3-4, pp. 276–287, 2011.
- [181] T. Jennewein, U. Achleitner, G. Weihs, H. Weinfurter, and A. Zeilinger, “A fast and compact quantum random number generator,” *Review of Scientific Instruments*, vol. 71, no. 4, pp. 1675–1680, 2000.
- [182] A. Stefanov, N. Gisin, O. Guinnard, L. Guinnard, and H. Zbinden, “Optical quantum random number generator,” *Journal of Modern Optics*, vol. 47, no. 4, pp. 595–598, 2000.
- [183] J. F. Dynes, Z. L. Yuan, A. W. Sharpe, and A. J. Shields, “A high speed, postprocessing free, quantum random number generator,” *Applied Physics Letters*, vol. 93, no. 3, p. 031109, 2008.
- [184] H. Lo, “Unconditional Security of Quantum Key Distribution over Arbitrarily Long Distances,” *Science*, vol. 283, no. 5410, pp. 2050–2056, 1999.
- [185] P. W. Shor and J. Preskill, “Simple Proof of Security of the BB84 Quantum Key Distribution Protocol,” *Physical Review Letters*, vol. 85, no. 2, pp. 441–444, 2000.
- [186] H.-K. Lo, X. Ma, and K. Chen, “Decoy State Quantum Key Distribution,” *Physical Review Letters*, vol. 94, no. 23, p. 230504, 2005.
- [187] N. Gisin, S. Fasel, B. Kraus, H. Zbinden, and G. Ribordy, “Trojan-horse attacks on quantum-key-distribution systems,” *Physical Review A*, vol. 73, no. 2, p. 022320, 2006.
- [188] Y. Zhao, C.-H. F. Fung, B. Qi, C. Chen, and H.-K. Lo, “Quantum hacking:

BIBLIOGRAPHY

- Experimental demonstration of time-shift attack against practical quantum-key-distribution systems,” *Physical Review A*, vol. 78, no. 4, p. 042333, 2008.
- [189] J. C. Loredo, M. A. Broome, P. Hilaire, O. Gazzano, I. Sagnes, A. Lemaitre, M. P. Almeida, P. Senellart, and A. G. White, “Boson Sampling with Single-Photon Fock States from a Bright Solid-State Source,” *Physical Review Letters*, vol. 118, no. 13, p. 130503, 2017.
- [190] D. J. Brod, E. F. Galvão, A. Crespi, R. Osellame, and N. Spagnolo, “Photonic implementation of boson sampling: a review,” *Advanced Photonics*, vol. 1, no. 03, p. 034001, 2019.
- [191] N. H. Lindner and T. Rudolph, “Proposal for pulsed On-demand sources of photonic cluster state strings,” *Physical Review Letters*, vol. 103, no. 11, p. 113602, 2009.
- [192] S. E. Economou, N. Lindner, and T. Rudolph, “Optically generated 2-dimensional photonic cluster state from coupled quantum dots,” *Physical Review Letters*, vol. 105, no. 9, p. 093601, 2010.
- [193] H. Pichler, S. Choi, P. Zoller, and M. D. Lukin, “Universal photonic quantum computation via time-delayed feedback,” *Proceedings of the National Academy of Sciences*, vol. 114, no. 43, pp. 11362–11367, 2017.
- [194] D. R. Simon, “On the Power of Quantum Computation,” *SIAM Journal on Computing*, vol. 26, no. 5, pp. 1474–1483, 1997.
- [195] P. W. Shor, “Polynomial-Time Algorithms for Prime Factorization and Discrete Logarithms on a Quantum Computer,” *SIAM Journal on Computing*, vol. 26, no. 5, pp. 1484–1509, 1997.
- [196] S. Aaronson and A. Arkhipov, “BosonSampling Is Far From Uniform.” , *arXiv:1309.7460v2* (2013).
- [197] N. Spagnolo, C. Vitelli, M. Bentivegna, D. J. Brod, A. Crespi, F. Flamini, S. Giacomini, G. Milani, R. Ramponi, P. Mataloni, R. Osellame, E. F. Galvão, and F. Sciarrino, “Experimental validation of photonic boson sampling,” *Nature Photonics*, vol. 8, no. 8, pp. 615–620, 2014.
- [198] S. Barz, J. F. Fitzsimons, E. Kashefi, and P. Walther, “Experimental verification of quantum computation,” *Nature Physics*, vol. 9, no. 11, pp. 727–731, 2013.
- [199] J. Barrett, L. Hardy, and A. Kent, “No Signaling and Quantum Key Distribution,” *Physical Review Letters*, vol. 95, no. 1, p. 010503, 2005.
- [200] A. Acín, N. Brunner, N. Gisin, S. Massar, S. Pironio, and V. Scarani, “Device-Independent Security of Quantum Cryptography against Collective Attacks,” *Physical Review Letters*, vol. 98, no. 23, p. 230501, 2007.
- [201] S. Pironio, A. Acín, N. Brunner, N. Gisin, S. Massar, and V. Scarani, “Device-independent quantum key distribution secure against collective attacks,” *New Journal of Physics*, vol. 11, no. 4, p. 045021, 2009.
- [202] H.-k. Lo, M. Curty, and B. Qi, “Measurement-Device-Independent Quantum Key Distribution,” *Physical Review Letters*, vol. 108, no. 13, p. 130503, 2012.
- [203] C. Branciard, E. G. Cavalcanti, S. P. Walborn, V. Scarani, and H. M. Wiseman, “One-sided device-independent quantum key distribution: Security,

BIBLIOGRAPHY

- feasibility, and the connection with steering,” *Physical Review A*, vol. 85, no. 1, p. 010301, 2012.
- [204] U. Vazirani and T. Vidick, “Fully Device-Independent Quantum Key Distribution,” *Physical Review Letters*, vol. 113, no. 14, p. 140501, 2014.
- [205] H.-k. Lo, M. Curty, and K. Tamaki, “Secure quantum key distribution,” *Nature Photonics*, vol. 8, no. 8, pp. 595–604, 2014.
- [206] S. Pironio, A. Acín, S. Massar, A. B. de la Giroday, D. N. Matsukevich, P. Maunz, S. Olmschenk, D. Hayes, L. Luo, T. A. Manning, and C. Monroe, “Random numbers certified by Bell’s theorem,” *Nature*, vol. 464, no. 7291, pp. 1021–1024, 2010.
- [207] Q. Zhang, X. H. Bao, C. Y. Lu, X. Q. Zhou, T. Yang, T. Rudolph, and J. W. Pan, “Demonstration of a scheme for the generation of ”event-ready” entangled photon pairs from a single-photon source,” *Physical Review A - Atomic, Molecular, and Optical Physics*, vol. 77, no. 6, p. 062316, 2008.
- [208] J. F. Clauser, M. A. Horne, A. Shimony, and R. A. Holt, “Proposed Experiment to Test Local Hidden-Variable Theories,” *Phys. Rev. Lett.*, vol. 23, no. 15, pp. 880–884, 1969.
- [209] S. Scheel, “Permanents in linear optical networks.” , *arXiv:quant-ph/0406127v1*, jun 2004.
- [210] S. Aaronson, “A linear-optical proof that the permanent is #P-hard,” *Proceedings of the Royal Society A: Mathematical, Physical and Engineering Sciences*, vol. 467, no. 2136, pp. 3393–3405, 2011.
- [211] S. Aaronson and A. Arkhipov, “The Computational Complexity of Linear Optics,” in *Research in Optical Sciences*, (Washington, D.C.), p. QTh1A.2, OSA, 2014.
- [212] L. G. Valiant, “The complexity of computing,” *Theoretical Computer Science*, vol. 8, no. 2, pp. 189–201, 1979.
- [213] U. Feige and C. Lund, “On the hardness of computing the permanent of random matrices,” *Computational Complexity*, vol. 6, no. 101, pp. 101–132, 1996.
- [214] D. Grier and L. Schaeffer, “New Hardness Results for the Permanent Using Linear Optics,” in *Proceedings of the 33rd Computational Complexity Conference*, no. 1122374 in CCC ’18, (Germany), pp. 19:1—19:29, Schloss Dagstuhl–Leibniz-Zentrum fuer Informatik, 2018.
- [215] Y. He, X. Ding, Z.-E. Su, H.-L. Huang, J. Qin, C. Wang, S. Unsleber, C. Chen, H. Wang, Y.-M. He, X.-L. Wang, W.-J. Zhang, S.-J. Chen, C. Schneider, M. Kamp, L.-X. You, Z. Wang, S. Höfling, C.-Y. Lu, and J.-W. Pan, “Time-Bin-Encoded Boson Sampling with a Single-Photon Device,” *Physical Review Letters*, vol. 118, no. 19, p. 190501, 2017.

Rate equation modelling for demultiplexed source

This appendix describes the rate equation modelling used to calculate the the bright state efficiency of the source in chapter 3. The model used is given in Fig. A.1 where we use the excitation to some higher state (A) which can relax into either the bright state (B) or the dark state (D). The pumping rate γ_{ga} excites the ground state (G) to state (A) which decays with γ_{ab} and γ_{ad} into the bright and dark states respectively. The bright and dark states decay back into the ground state via γ_{bg} and γ_{dg} . The rate equation model can be set up as described in Sec. 2.3.4 but now with four states. The matrix representation of this model is

$$\begin{pmatrix} \dot{n}_G \\ \dot{n}_A \\ \dot{n}_B \\ \dot{n}_D \end{pmatrix} = \begin{bmatrix} -\gamma_{ga} & 0 & \gamma_{bg} & \gamma_{dg} \\ \gamma_{ga} & -(\gamma_{ab} + \gamma_{ad}) & 0 & 0 \\ 0 & \gamma_{ab} & -\gamma_{bg} & 0 \\ 0 & \gamma_{ad} & 0 & -\gamma_{dg} \end{bmatrix} \begin{pmatrix} n_G \\ n_A \\ n_B \\ n_D \end{pmatrix}. \quad (\text{A.1})$$

The matrix has four eigenvalues and four eigenvectors from which the complete time evolution for every state can be defined as

$$n(t) = \sum_{k=1}^{\#\lambda} c_k \bar{v}_k e^{\lambda_k t}, \quad (\text{A.2})$$

where c_k indicate constants determined by the boundary condition. If we set the boundary condition on $t = 0$ to a state we know we obtain the equality

$$\bar{v} \bar{c} = \bar{n}(0) \rightarrow \bar{c} = \bar{v}^{-1} \bar{n}(0). \quad (\text{A.3})$$

The most common initial condition is

$$\bar{n}(0) = \begin{pmatrix} 1 \\ 0 \\ 0 \\ 0 \end{pmatrix} \quad (\text{A.4})$$

which means that all the population starts in the ground state. Knowing the eigenvectors, eigenvalues and differential constants, we can calculate the efficiency of the source.

Appendix A. Rate equation modelling for demultiplexed source

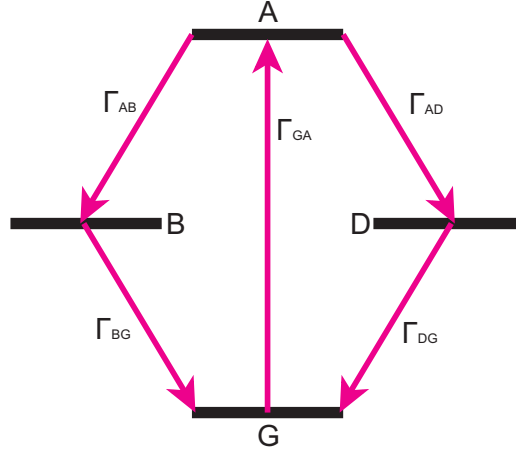


Figure A.1: Model used to set up the rate equations. The photon is excited from the ground state (G) to a higher state (A) with a pumping rate of γ_{ga} . From the higher order state it relaxes into the bright exciton state (B) and dark exciton state (D) with relaxation rates γ_{ab} and γ_{ad} . The bright and dark states decay back to the ground state with γ_{bg} and γ_{dg} . The decay from the bright state yields a photon and the source efficiency at time t is therefore the normalised population in the bright state $n_b(t)$.

We know that one of the eigenvalues will be zero, which we assume to be $\lambda_1 = 0$. When the time goes to infinity $t \rightarrow \infty$, only the exponential term with λ_1 remains. Therefore we only consider the eigenvector and differential constant belonging to λ_1 , which are \bar{v}_1 and c_1 . These values are calculated to be

$$\bar{v}_1 = \begin{pmatrix} \frac{\gamma_{dg}(\gamma_{ab} + \gamma_{ad})}{\gamma_{ad}\gamma_{ga}} \\ \frac{\gamma_{dg}}{\gamma_{ad}} \\ \frac{\gamma_{ab}\gamma_{dg}}{\gamma_{ad}\gamma_{bg}} \\ 1 \end{pmatrix} \quad (\text{A.5})$$

and

$$c_1 = \frac{\gamma_{ad}\gamma_{bg}\gamma_{ga}}{\gamma_{ab}\gamma_{bg}\gamma_{dg} + \gamma_{ad}\gamma_{bg}\gamma_{dg} + \gamma_{ad}\gamma_{bg}\gamma_{ga} + \gamma_{ab}\gamma_{dg}\gamma_{ga} + \gamma_{bg}\gamma_{dg}\gamma_{ga}}. \quad (\text{A.6})$$

The saturation behaviour is now given by the element from the eigenvector describing the bright state multiplied with the differential constant

$$\eta_s(\gamma_{ga}) = \frac{\gamma_{ab}\gamma_{dg}\gamma_{ga}}{\gamma_{ab}\gamma_{bg}\gamma_{dg} + \gamma_{ad}\gamma_{bg}\gamma_{dg} + \gamma_{ad}\gamma_{bg}\gamma_{ga} + \gamma_{ab}\gamma_{dg}\gamma_{ga} + \gamma_{bg}\gamma_{dg}\gamma_{ga}}. \quad (\text{A.7})$$

Where the maximum efficiency is reach when γ_{ga} is large compared to the rest, resulting in

$$\eta_s(\gamma_{ga} \rightarrow \infty) = \frac{\gamma_{ab}\gamma_{dg}}{\gamma_{ad}\gamma_{bg} + \gamma_{ab}\gamma_{dg} + \gamma_{bg}\gamma_{dg}}. \quad (\text{A.8})$$

We assume that $\gamma_{ab} = 2\gamma_{bg}$ and $\gamma_{ad} = 2\gamma_{dg}$ due to a cascade through the bi-exciton, which simplifies the source efficiency to

$$\eta_s(\gamma_{ga} \rightarrow \infty) = \frac{2\gamma_{bg}\gamma_{dg}}{2\gamma_{dg}\gamma_{bg} + 2\gamma_{bg}\gamma_{dg} + \gamma_{bg}\gamma_{dg}} = \frac{4}{10}. \quad (\text{A.9})$$

The source efficiency is independent on the rates in the assumption we made.

To find the time evolution of the system we insert the measured decay rates of the bright and dark state of $\gamma_{bg} = 0.95 \text{ ns}^{-1}$ and $\gamma_{dg} = 0.05 \text{ ns}^{-1}$. This result in eigenvalues with unit ns^{-1} of

$$\lambda_1 = 0, \lambda_2 = -0.081, \lambda_3 = -2.92, \lambda_4 \propto -\gamma_{ga}, \quad (\text{A.10})$$

And eigenvectors multiplied with differential constants of

$$c_1\bar{v}_1 = \begin{pmatrix} 0 \\ 0.2 \\ 0.4 \\ 0.4 \end{pmatrix}, c_2\bar{v}_2 = \begin{pmatrix} 0 \\ 0.118 \\ 0.258 \\ -0.376 \end{pmatrix}, c_3\bar{v}_3 = \begin{pmatrix} 0 \\ 0.682 \\ -0.658 \\ -0.024 \end{pmatrix}, c_4\bar{v}_4 = \begin{pmatrix} 1 \\ -1 \\ 0 \\ 0 \end{pmatrix}. \quad (\text{A.11})$$

Setup design of the demultiplexer

The design of the demultiplexer setup from Ch. 3 is shown in this appendix. Figure B.1 shows the 4-fold demultiplexer setup together with the legend of the optomechanical components. The size of the components in the drawing corresponds to the physical size used on the optical table. The grid indicate the screw holes of the optical table, where every cross-point of grid-lines is the location of the screw hole. The real distance between the grid lines is 2.5 cm. This setup is derived from the original design of a 8-fold demultiplexing setup which is

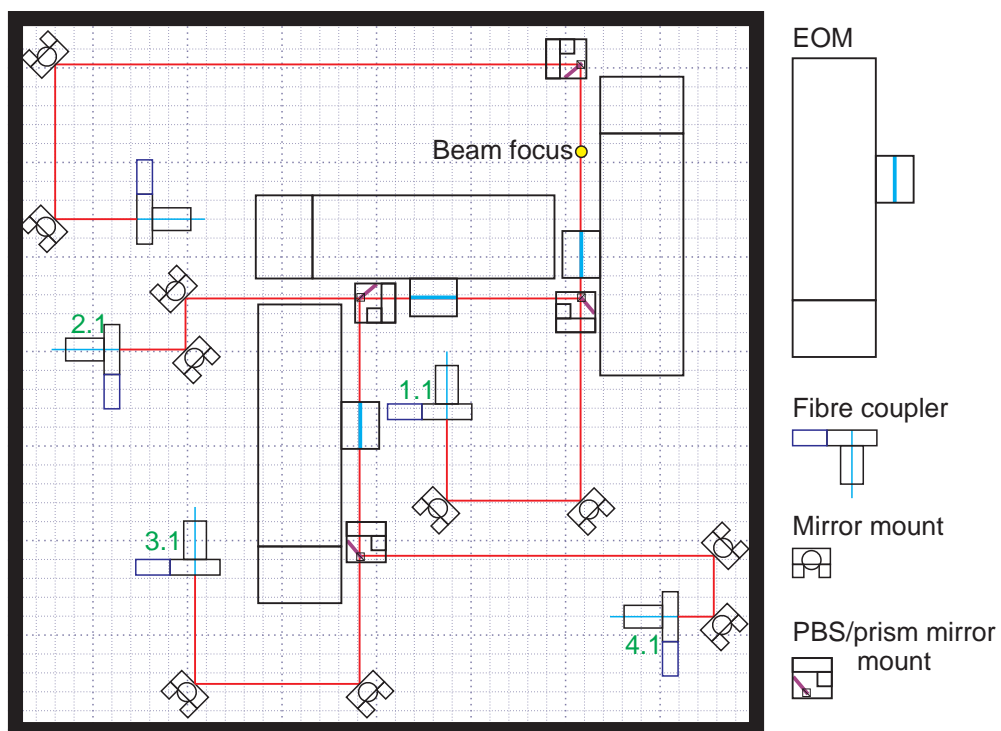


Figure B.1: Design for a 4-fold demultiplexer setup. On the bottom is the legend of the optomechanical mounts.

Appendix B. Setup design of the demultiplexer

shown in Fig. B.2. This 8-fold demultiplexer has a resonant EOM inserted in the input with a delay line to double the number of spatial modes. The current 4-fold demultiplexer is exactly setup from the 8-fold demultiplexer, but without the resonant EOM, delay loop and extra optical components. Due to this designing, the current 4-fold setup can be directly expanded to an 8-fold setup by adding the extra components while nothing has to change to the parts of the 4-fold setup.

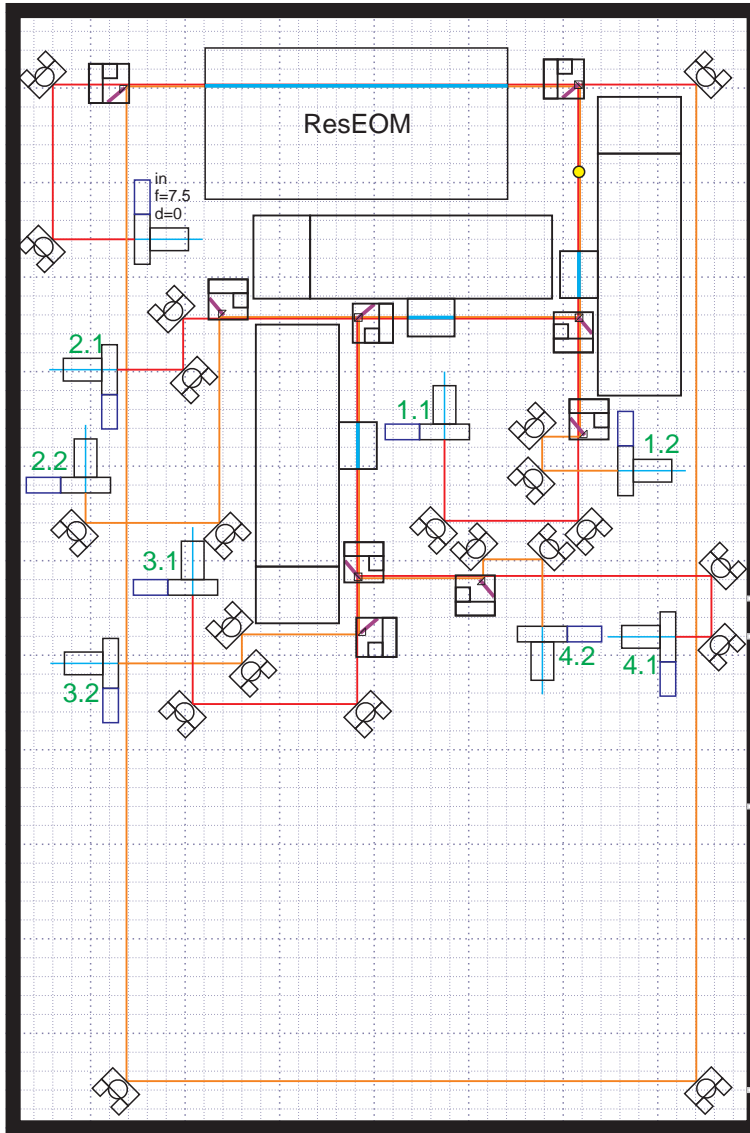


Figure B.2: Original design of the demultiplexer setup, designed for 8-fold demultiplexing. The 4-fold demultiplexer design is directly taken from this design by removing all paths induced by the large delay loop. Current 4-fold demultiplexer can be directly expanded to this.

States in entanglement gate

This appendix shows the evolution of the state through the *Heralded Entanglement Gate* from chapter 5. A schematic of the gate can be seen in Fig. 5.1. This appendix starts at where paths B' and C' combine, which is just before the PBS in the RPBS. Paths A' D' already had all their operations. The full state directly before the PBS in the RPBS is:

$$\begin{aligned}
 |\psi_{ABCD'}\rangle = & \tag{C.1} \\
 & \left[\frac{1}{8} \hat{a}'_{H\dagger} \hat{d}'_{H\dagger} \left(\hat{b}'_{H\dagger} \hat{c}'_{H\dagger} + \hat{b}'_{H\dagger} \hat{c}'_{V\dagger} + \hat{b}'_{V\dagger} \hat{c}'_{H\dagger} + \hat{b}'_{V\dagger} \hat{c}'_{V\dagger} \right) \right. \\
 & + \frac{1}{8} \hat{a}'_{H\dagger} \hat{d}'_{V\dagger} \left(-\hat{b}'_{H\dagger} \hat{c}'_{H\dagger} + \hat{b}'_{H\dagger} \hat{c}'_{V\dagger} - \hat{b}'_{V\dagger} \hat{c}'_{H\dagger} + \hat{b}'_{V\dagger} \hat{c}'_{V\dagger} \right) \\
 & + \frac{1}{8} \hat{a}'_{V\dagger} \hat{d}'_{H\dagger} \left(-\hat{b}'_{H\dagger} \hat{c}'_{H\dagger} - \hat{b}'_{H\dagger} \hat{c}'_{V\dagger} + \hat{b}'_{V\dagger} \hat{c}'_{H\dagger} + \hat{b}'_{V\dagger} \hat{c}'_{V\dagger} \right) \\
 & + \frac{1}{8} \hat{a}'_{V\dagger} \hat{d}'_{V\dagger} \left(\hat{b}'_{H\dagger} \hat{c}'_{H\dagger} - \hat{b}'_{H\dagger} \hat{c}'_{V\dagger} - \hat{b}'_{V\dagger} \hat{c}'_{H\dagger} + \hat{b}'_{V\dagger} \hat{c}'_{V\dagger} \right) \\
 & + \frac{i\sqrt{2}}{8} \hat{a}'_{H\dagger} \hat{d}'_{H\dagger} \hat{d}'_{V\dagger} \left(\hat{b}'_{H\dagger} + \hat{b}'_{V\dagger} \right) + \frac{i\sqrt{2}}{8} \hat{a}'_{V\dagger} \hat{d}'_{H\dagger} \hat{d}'_{V\dagger} \left(-\hat{b}'_{H\dagger} + \hat{b}'_{V\dagger} \right) \\
 & + \frac{i\sqrt{2}}{16} \hat{a}'_{H\dagger} \left(\hat{b}'_{H\dagger} \hat{c}'_{H\dagger} \hat{c}'_{H\dagger} + \hat{b}'_{V\dagger} \hat{c}'_{H\dagger} \hat{c}'_{H\dagger} - \hat{b}'_{H\dagger} \hat{c}'_{V\dagger} \hat{c}'_{V\dagger} - \hat{b}'_{V\dagger} \hat{c}'_{V\dagger} \hat{c}'_{V\dagger} \right) \\
 & + \frac{i\sqrt{2}}{16} \hat{a}'_{V\dagger} \left(-\hat{b}'_{H\dagger} \hat{c}'_{H\dagger} \hat{c}'_{H\dagger} + \hat{b}'_{V\dagger} \hat{c}'_{H\dagger} \hat{c}'_{H\dagger} + \hat{b}'_{H\dagger} \hat{c}'_{V\dagger} \hat{c}'_{V\dagger} - \hat{b}'_{V\dagger} \hat{c}'_{V\dagger} \hat{c}'_{V\dagger} \right) \\
 & + \frac{i\sqrt{2}}{8} \hat{a}'_{H\dagger} \hat{a}'_{V\dagger} \hat{d}'_{H\dagger} \left(\hat{c}'_{H\dagger} + \hat{c}'_{V\dagger} \right) + \frac{i\sqrt{2}}{8} \hat{a}'_{H\dagger} \hat{a}'_{V\dagger} \hat{d}'_{V\dagger} \left(-\hat{c}'_{H\dagger} + \hat{c}'_{V\dagger} \right) \\
 & + \frac{i\sqrt{2}}{16} \hat{d}'_{H\dagger} \left(+\hat{b}'_{H\dagger} \hat{b}'_{H\dagger} \hat{c}'_{H\dagger} + \hat{b}'_{H\dagger} \hat{b}'_{H\dagger} \hat{c}'_{V\dagger} - \hat{b}'_{V\dagger} \hat{b}'_{V\dagger} \hat{c}'_{H\dagger} - \hat{b}'_{V\dagger} \hat{b}'_{V\dagger} \hat{c}'_{V\dagger} \right) \\
 & + \frac{i\sqrt{2}}{16} \hat{d}'_{V\dagger} \left(-\hat{b}'_{H\dagger} \hat{b}'_{H\dagger} \hat{c}'_{H\dagger} + \hat{b}'_{H\dagger} \hat{b}'_{H\dagger} \hat{c}'_{V\dagger} + \hat{b}'_{V\dagger} \hat{b}'_{V\dagger} \hat{c}'_{H\dagger} - \hat{b}'_{V\dagger} \hat{b}'_{V\dagger} \hat{c}'_{V\dagger} \right) \\
 & + \frac{i^2}{4} \hat{a}'_{H\dagger} \hat{a}'_{V\dagger} \hat{d}'_{H\dagger} \hat{d}'_{V\dagger} + \frac{i^2}{8} \hat{a}'_{H\dagger} \hat{a}'_{V\dagger} \left(\hat{c}'_{H\dagger} \hat{c}'_{H\dagger} - \hat{c}'_{V\dagger} \hat{c}'_{V\dagger} \right) + \frac{i^2}{8} \hat{d}'_{H\dagger} \hat{d}'_{V\dagger} \left(\hat{b}'_{H\dagger} \hat{b}'_{H\dagger} - \hat{b}'_{V\dagger} \hat{b}'_{V\dagger} \right) \\
 & \left. + \frac{i^2}{16} \left(\hat{b}'_{H\dagger} \hat{b}'_{H\dagger} \hat{c}'_{H\dagger} \hat{c}'_{H\dagger} + \hat{b}'_{V\dagger} \hat{b}'_{V\dagger} \hat{c}'_{V\dagger} \hat{c}'_{V\dagger} - \hat{b}'_{H\dagger} \hat{b}'_{H\dagger} \hat{c}'_{V\dagger} \hat{c}'_{V\dagger} - \hat{b}'_{V\dagger} \hat{b}'_{V\dagger} \hat{c}'_{H\dagger} \hat{c}'_{H\dagger} \right) \right] |0\rangle
 \end{aligned}$$

Appendix C. States in entanglement gate

The PBS than acts on paths B' and C' resulting in state:

$$\begin{aligned}
 & |\psi_{ABCD'..}\rangle = \tag{C.2} \\
 & \left[\frac{1}{8} \hat{a}'_{H\dagger} \hat{d}'_{H\dagger} \left(\hat{b}'_{H\dagger} \hat{c}'_{H\dagger} + i \hat{c}'_{H\dagger} \hat{c}'_{V\dagger} + i \hat{b}'_{H\dagger} \hat{b}'_{V\dagger} - \hat{b}'_{V\dagger} \hat{c}'_{V\dagger} \right) \right. \\
 & + \frac{1}{8} \hat{a}'_{H\dagger} \hat{d}'_{V\dagger} \left(-\hat{b}'_{H\dagger} \hat{c}'_{H\dagger} + i \hat{c}'_{H\dagger} \hat{c}'_{V\dagger} - i \hat{b}'_{H\dagger} \hat{b}'_{V\dagger} - \hat{b}'_{V\dagger} \hat{c}'_{V\dagger} \right) \\
 & + \frac{1}{8} \hat{a}'_{V\dagger} \hat{d}'_{H\dagger} \left(-\hat{b}'_{H\dagger} \hat{c}'_{H\dagger} - i \hat{c}'_{H\dagger} \hat{c}'_{V\dagger} + i \hat{b}'_{H\dagger} \hat{b}'_{V\dagger} - \hat{b}'_{V\dagger} \hat{c}'_{V\dagger} \right) \\
 & + \frac{1}{8} \hat{a}'_{V\dagger} \hat{d}'_{V\dagger} \left(\hat{b}'_{H\dagger} \hat{c}'_{H\dagger} - i \hat{c}'_{H\dagger} \hat{c}'_{V\dagger} - i \hat{b}'_{H\dagger} \hat{b}'_{V\dagger} - \hat{b}'_{V\dagger} \hat{c}'_{V\dagger} \right) \\
 & + \frac{i\sqrt{2}}{8} \hat{a}'_{H\dagger} \hat{d}'_{H\dagger} \hat{d}'_{V\dagger} \left(\hat{c}'_{H\dagger} + i \hat{b}'_{V\dagger} \right) + \frac{i\sqrt{2}}{8} \hat{a}'_{V\dagger} \hat{d}'_{H\dagger} \hat{d}'_{V\dagger} \left(-\hat{c}'_{H\dagger} + i \hat{b}'_{V\dagger} \right) \\
 & + \frac{i\sqrt{2}}{16} \hat{a}'_{H\dagger} \left(+\hat{c}'_{H\dagger} \hat{c}'_{V\dagger} \hat{c}'_{V\dagger} + i \hat{b}'_{V\dagger} \hat{c}'_{V\dagger} \hat{c}'_{V\dagger} + \hat{b}'_{H\dagger} \hat{b}'_{H\dagger} \hat{c}'_{H\dagger} + i \hat{b}'_{H\dagger} \hat{b}'_{H\dagger} \hat{b}'_{V\dagger} \right) \\
 & + \frac{i\sqrt{2}}{16} \hat{a}'_{V\dagger} \left(-\hat{c}'_{H\dagger} \hat{c}'_{V\dagger} \hat{c}'_{V\dagger} + i \hat{b}'_{V\dagger} \hat{c}'_{V\dagger} \hat{c}'_{V\dagger} - \hat{b}'_{H\dagger} \hat{b}'_{H\dagger} \hat{c}'_{H\dagger} + i \hat{b}'_{H\dagger} \hat{b}'_{H\dagger} \hat{b}'_{V\dagger} \right) \\
 & + \frac{i\sqrt{2}}{8} \hat{a}'_{H\dagger} \hat{a}'_{V\dagger} \hat{d}'_{H\dagger} \left(\hat{b}'_{H\dagger} + i \hat{c}'_{V\dagger} \right) + \frac{i\sqrt{2}}{8} \hat{a}'_{H\dagger} \hat{a}'_{V\dagger} \hat{d}'_{V\dagger} \left(-\hat{b}'_{H\dagger} + i \hat{c}'_{V\dagger} \right) \\
 & + \frac{i\sqrt{2}}{16} \hat{d}'_{H\dagger} \left(i \hat{c}'_{H\dagger} \hat{c}'_{H\dagger} \hat{c}'_{V\dagger} + \hat{b}'_{H\dagger} \hat{c}'_{H\dagger} \hat{c}'_{H\dagger} + i \hat{b}'_{V\dagger} \hat{b}'_{V\dagger} \hat{c}'_{V\dagger} + \hat{b}'_{H\dagger} \hat{b}'_{V\dagger} \hat{b}'_{V\dagger} \right) \\
 & + \frac{i\sqrt{2}}{16} \hat{d}'_{V\dagger} \left(i \hat{c}'_{H\dagger} \hat{c}'_{H\dagger} \hat{c}'_{V\dagger} - \hat{b}'_{H\dagger} \hat{c}'_{H\dagger} \hat{c}'_{H\dagger} + i \hat{b}'_{V\dagger} \hat{b}'_{V\dagger} \hat{c}'_{V\dagger} - \hat{b}'_{H\dagger} \hat{b}'_{V\dagger} \hat{b}'_{V\dagger} \right) \\
 & + \frac{i^2}{4} \hat{a}'_{H\dagger} \hat{a}'_{V\dagger} \hat{d}'_{H\dagger} \hat{d}'_{V\dagger} + \frac{i^2}{8} \hat{a}'_{H\dagger} \hat{a}'_{V\dagger} \left(\hat{b}'_{H\dagger} \hat{b}'_{H\dagger} + \hat{c}'_{V\dagger} \hat{c}'_{V\dagger} \right) + \frac{i^2}{8} \hat{d}'_{H\dagger} \hat{d}'_{V\dagger} \left(\hat{c}'_{H\dagger} \hat{c}'_{H\dagger} + \hat{b}'_{V\dagger} \hat{b}'_{V\dagger} \right) \\
 & \left. + \frac{i^2}{16} \left(\hat{b}'_{H\dagger} \hat{b}'_{H\dagger} \hat{c}'_{H\dagger} \hat{c}'_{H\dagger} + \hat{b}'_{V\dagger} \hat{b}'_{V\dagger} \hat{c}'_{V\dagger} \hat{c}'_{V\dagger} + \hat{c}'_{H\dagger} \hat{c}'_{H\dagger} \hat{c}'_{V\dagger} \hat{c}'_{V\dagger} + \hat{b}'_{H\dagger} \hat{b}'_{H\dagger} \hat{b}'_{V\dagger} \hat{b}'_{V\dagger} \right) \right] |0\rangle
 \end{aligned}$$

The heralding is done on a coincidence detection between paths B'' and C'' thus we ignore all states that cannot contribute to such a coincidence. The resulting state of this reduction is not normalised to 1 anymore since we maintain the normalisation to the full state. The outcome of this reduction is:

$$\begin{aligned}
 |\psi_{ABCD''}\rangle = & \frac{\sqrt{2}}{8} \Phi_{A,D}^{\dagger} (\hat{b}_H'' \hat{c}_V'' + \hat{b}_V'' \hat{c}_H'') - \frac{\sqrt{2}}{8} \Psi_{A,D}^{\dagger} (\hat{b}_H'' \hat{c}_H'' + \hat{b}_V'' \hat{c}_V'') \\
 & + \left[\frac{i}{32} \hat{a}_H'' \left(+i\hat{b}_H'' \hat{c}_H'' \hat{c}_H'' + i\hat{b}_H'' \hat{c}_V'' \hat{c}_V'' - 2i\hat{b}_H'' \hat{c}_H'' \hat{c}_V'' - i\hat{b}_V'' \hat{c}_H'' \hat{c}_H'' - i\hat{b}_V'' \hat{c}_V'' \hat{c}_V'' + 2i\hat{b}_V'' \hat{c}_H'' \hat{c}_V'' \right. \right. \\
 & \quad \left. \left. + \hat{b}_H'' \hat{b}_H'' \hat{c}_H'' + \hat{b}_V'' \hat{b}_V'' \hat{c}_H'' + 2\hat{b}_H'' \hat{b}_V'' \hat{c}_H'' + \hat{b}_H'' \hat{b}_H'' \hat{c}_V'' + \hat{b}_V'' \hat{b}_V'' \hat{c}_V'' + 2\hat{b}_H'' \hat{b}_V'' \hat{c}_V'' \right) \right. \\
 & + \frac{i}{32} \hat{a}_V'' \left(+i\hat{b}_H'' \hat{c}_H'' \hat{c}_H'' + i\hat{b}_H'' \hat{c}_V'' \hat{c}_V'' - 2i\hat{b}_H'' \hat{c}_H'' \hat{c}_V'' - i\hat{b}_V'' \hat{c}_H'' \hat{c}_H'' - i\hat{b}_V'' \hat{c}_V'' \hat{c}_V'' + 2i\hat{b}_V'' \hat{c}_H'' \hat{c}_V'' \right. \\
 & \quad \left. - \hat{b}_H'' \hat{b}_H'' \hat{c}_H'' - \hat{b}_V'' \hat{b}_V'' \hat{c}_H'' - 2\hat{b}_H'' \hat{b}_V'' \hat{c}_H'' - \hat{b}_H'' \hat{b}_H'' \hat{c}_V'' - \hat{b}_V'' \hat{b}_V'' \hat{c}_V'' - 2\hat{b}_H'' \hat{b}_V'' \hat{c}_V'' \right) \\
 & + \frac{i}{32} \hat{d}_H'' \left(+\hat{b}_H'' \hat{c}_H'' \hat{c}_H'' + \hat{b}_H'' \hat{c}_V'' \hat{c}_V'' + 2\hat{b}_H'' \hat{c}_H'' \hat{c}_V'' + \hat{b}_V'' \hat{c}_H'' \hat{c}_H'' + \hat{b}_V'' \hat{c}_V'' \hat{c}_V'' + 2\hat{b}_V'' \hat{c}_H'' \hat{c}_V'' \right. \\
 & \quad \left. + i\hat{b}_H'' \hat{b}_H'' \hat{c}_H'' + i\hat{b}_V'' \hat{b}_V'' \hat{c}_H'' - 2i\hat{b}_H'' \hat{b}_V'' \hat{c}_H'' - i\hat{b}_H'' \hat{b}_H'' \hat{c}_V'' - i\hat{b}_V'' \hat{b}_V'' \hat{c}_V'' + 2i\hat{b}_H'' \hat{b}_V'' \hat{c}_V'' \right) \\
 & + \frac{i}{32} \hat{d}_V'' \left(-\hat{b}_H'' \hat{c}_H'' \hat{c}_H'' - \hat{b}_H'' \hat{c}_V'' \hat{c}_V'' - 2\hat{b}_H'' \hat{c}_H'' \hat{c}_V'' - \hat{b}_V'' \hat{c}_H'' \hat{c}_H'' - \hat{b}_V'' \hat{c}_V'' \hat{c}_V'' - 2\hat{b}_V'' \hat{c}_H'' \hat{c}_V'' \right. \\
 & \quad \left. + i\hat{b}_H'' \hat{b}_H'' \hat{c}_H'' + i\hat{b}_V'' \hat{b}_V'' \hat{c}_H'' - 2i\hat{b}_H'' \hat{b}_V'' \hat{c}_H'' - i\hat{b}_H'' \hat{b}_H'' \hat{c}_V'' - i\hat{b}_V'' \hat{b}_V'' \hat{c}_V'' + 2i\hat{b}_H'' \hat{b}_V'' \hat{c}_V'' \right) \\
 & \left. + \frac{i^2}{64} \left(2\hat{b}_H'' \hat{b}_H'' \hat{c}_H'' \hat{c}_H'' + 2\hat{b}_V'' \hat{b}_V'' \hat{c}_V'' \hat{c}_V'' + 2\hat{b}_H'' \hat{b}_H'' \hat{c}_V'' \hat{c}_V'' + 2\hat{b}_V'' \hat{b}_V'' \hat{c}_H'' \hat{c}_H'' + 8\hat{b}_H'' \hat{b}_V'' \hat{c}_H'' \hat{c}_V'' \right) \right] |0\rangle
 \end{aligned} \tag{C.5}$$

Applying the creation operators on the vacuum state result in a final state before detection of:

$$\begin{aligned}
 |\psi_{ABCD''}\rangle = & \frac{\sqrt{2}}{8} \Phi_{A,D}^{\dagger} (|H\rangle_B'' |V\rangle_C'' + |V\rangle_B'' |H\rangle_C'') - \frac{\sqrt{2}}{8} \Psi_{A,D}^{\dagger} (|H\rangle_B'' |H\rangle_C'' + |V\rangle_B'' |V\rangle_C'') \\
 & + \frac{i\sqrt{2}}{32} |H\rangle_A'' |0\rangle_D'' \left(+i|H\rangle_B'' |H, H\rangle_C'' + i|H\rangle_B'' |V, V\rangle_C'' - \sqrt{2}i|H\rangle_B'' |H, V\rangle_C'' - i|V\rangle_B'' |H, H\rangle_C'' \right. \\
 & \quad \left. - i|V\rangle_B'' |V, V\rangle_C'' + \sqrt{2}i|V\rangle_B'' |H, V\rangle_C'' + |H, H\rangle_B'' |H\rangle_C'' + |V, V\rangle_B'' |H\rangle_C'' \right. \\
 & \quad \left. + \sqrt{2}|H, V\rangle_B'' |H\rangle_C'' + |H, H\rangle_B'' |V\rangle_C'' + |V, V\rangle_B'' |V\rangle_C'' + \sqrt{2}|H, V\rangle_B'' |V\rangle_C'' \right) \\
 & + \frac{i\sqrt{2}}{32} |V\rangle_A'' |0\rangle_D'' \left(+i|H\rangle_B'' |H, H\rangle_C'' + i|H\rangle_B'' |V, V\rangle_C'' - \sqrt{2}i|H\rangle_B'' |H, V\rangle_C'' - i|V\rangle_B'' |H, H\rangle_C'' \right. \\
 & \quad \left. - i|V\rangle_B'' |V, V\rangle_C'' + \sqrt{2}i|V\rangle_B'' |H, V\rangle_C'' - |H, H\rangle_B'' |H\rangle_C'' - |V, V\rangle_B'' |H\rangle_C'' \right. \\
 & \quad \left. - \sqrt{2}|H, V\rangle_B'' |H\rangle_C'' - |H, H\rangle_B'' |V\rangle_C'' - |V, V\rangle_B'' |V\rangle_C'' - \sqrt{2}|H, V\rangle_B'' |V\rangle_C'' \right) \\
 & + \frac{\sqrt{2}}{32} |0\rangle_A'' |H\rangle_D'' \left(+|H\rangle_B'' |H, H\rangle_C'' + |H\rangle_B'' |V, V\rangle_C'' + \sqrt{2}|H\rangle_B'' |H, V\rangle_C'' + |V\rangle_B'' |H, H\rangle_C'' \right. \\
 & \quad \left. + |V\rangle_B'' |V, V\rangle_C'' + \sqrt{2}|V\rangle_B'' |H, V\rangle_C'' + i|H, H\rangle_B'' |H\rangle_C'' + i|V, V\rangle_B'' |H\rangle_C'' \right. \\
 & \quad \left. - \sqrt{2}i|H, V\rangle_B'' |H\rangle_C'' - i|H, H\rangle_B'' |V\rangle_C'' - i|V, V\rangle_B'' |V\rangle_C'' + \sqrt{2}i|H, V\rangle_B'' |V\rangle_C'' \right) \\
 & + \frac{i\sqrt{2}}{32} |0\rangle_A'' |V\rangle_D'' \left(-|H\rangle_B'' |H, H\rangle_C'' - |H\rangle_B'' |V, V\rangle_C'' - \sqrt{2}|H\rangle_B'' |H, V\rangle_C'' - |V\rangle_B'' |H, H\rangle_C'' \right. \\
 & \quad \left. - |V\rangle_B'' |V, V\rangle_C'' - \sqrt{2}|V\rangle_B'' |H, V\rangle_C'' + i|H, H\rangle_B'' |H\rangle_C'' + i|V, V\rangle_B'' |H\rangle_C'' \right. \\
 & \quad \left. - \sqrt{2}i|H, V\rangle_B'' |H\rangle_C'' - i|H, H\rangle_B'' |V\rangle_C'' - i|V, V\rangle_B'' |V\rangle_C'' + \sqrt{2}i|H, V\rangle_B'' |V\rangle_C'' \right) \\
 & + \frac{i^2}{16} |0\rangle_A'' |0\rangle_D'' \left(|H, H\rangle_B'' |H, H\rangle_C'' + |V, V\rangle_B'' |V, V\rangle_C'' + |H, H\rangle_B'' |V, V\rangle_C'' + |V, V\rangle_B'' |H, H\rangle_C'' + 2|H, V\rangle_B'' |H, V\rangle_C'' \right)
 \end{aligned} \tag{C.6}$$

Polarising beamsplitter with limited indistinguishability

Transformation of a polarising beamsplitter with limited efficiency, limited transmission and reflection extinction and limited indistinguishability of the input photons. This transfer is used in Ch. 5 to calculate the heralding efficiencies and state probabilities in case of an imperfect setup. The variables before the double vertical line are multipliers for that row.

$$\begin{pmatrix} \hat{a}'_{HI} \\ \hat{a}'_{VI} \\ \hat{b}'_{HI} \\ \hat{b}'_{VI} \\ \hline \hat{a}'_{Ha} \\ \hat{a}'_{Va} \\ \hat{b}'_{Ha} \\ \hat{b}'_{Va} \\ \hline \hat{a}'_{Hb} \\ \hat{a}'_{Vb} \\ \hat{b}'_{Hb} \\ \hat{b}'_{Vb} \\ \hline \hat{L} \end{pmatrix} = \left(\begin{array}{c|cccccc} \sqrt{Q}\eta_L & i\sqrt{1-\eta_H} & 0 & \sqrt{\eta_H} & 0 & 0 \\ \sqrt{Q}\eta_L & 0 & i\sqrt{\eta_V} & 0 & \sqrt{1-\eta_V} & 0 \\ \sqrt{Q}\eta_L & \sqrt{\eta_H} & 0 & i\sqrt{1-\eta_H} & 0 & 0 \\ \sqrt{Q}\eta_L & 0 & \sqrt{1-\eta_V} & 0 & 0 & i\sqrt{\eta_V} \\ \hline \sqrt{(1-Q)\eta_L} & i\sqrt{1-\eta_H} & 0 & 0 & 0 & 0 \\ \sqrt{(1-Q)\eta_L} & 0 & i\sqrt{\eta_V} & 0 & 0 & 0 \\ \sqrt{(1-Q)\eta_L} & \sqrt{\eta_H} & 0 & 0 & 0 & 0 \\ \sqrt{(1-Q)\eta_L} & 0 & \sqrt{1-\eta_V} & 0 & 0 & 0 \\ \hline \sqrt{(1-Q)\eta_L} & 0 & 0 & \sqrt{\eta_H} & 0 & 0 \\ \sqrt{(1-Q)\eta_L} & 0 & 0 & 0 & \sqrt{1-\eta_V} & 0 \\ \sqrt{(1-Q)\eta_L} & 0 & 0 & i\sqrt{1-\eta_H} & 0 & 0 \\ \sqrt{(1-Q)\eta_L} & 0 & 0 & 0 & 0 & i\sqrt{\eta_V} \\ \hline \sqrt{1-\eta_L} & \sqrt{1-\eta_L} & \sqrt{1-\eta_L} & \sqrt{1-\eta_L} & \sqrt{1-\eta_L} & 1 \end{array} \right) \begin{pmatrix} \hat{a}'_H \\ \hat{a}'_V \\ \hat{b}'_H \\ \hat{b}'_V \\ \hat{L} \end{pmatrix} \quad (\text{D.1})$$